WAVE BREAKING INDUCED DRIFT

An experimental and theoretical prediction in deep-water waves

Master thesis
J.E. Swagemakers

TU Delft

WAVE BREAKING INDUCED DRIFT

An experimental and theoretical prediction in deep-water waves

by:

J.E. Swagemakers

To obtain the degree of
Master of Science
In Hydraulic Engineering
At the Delft University of Technology
To be defended publicly on Thursday October 20th, 2022 at 12:00

Student number: 4442105

Date: 12-10-2022
Thesis committee:

Dr. Ir. T.S. van den Bremer	TU Delft, Chair
Dr. Ir. M.A. de Schipper	TU Delft
Dr. Ir. R. Calvert	TU Delft/University of Edinburgh

TU Delft

Preface

Growing up in a less fortunate neighbourhood in the city of Rotterdam I became aware of the large amount of pollution on the streets. When I grew older I realised this was not only a local problem but a global catastrophe happening around us. I always had this ambition to use my technical knowledge to contribute to a solution. When looking for a master's thesis topic, the opportunity arose to be part of a large-scale experimental campaign from the European Space Agency at Deltares to work with experts in the field and contribute to research into plastic pollution in the ocean. The decision was not difficult; In my thesis, I focus on the transport of breaking waves in the ocean. This thesis is part of my Master's program in Hydraulic Engineering at the Delft University of Technology.

First of all, I would like to thank my daily supervisor Ton van den Bremer, for his challenging questions and feedback to make me look more critically of my work. I also want to thank Ross Calvert, who was always available to discuss any challenges and gave me the right nudge toward solutions. Your input during the meetings kept me on track and I appreciate the time and effort you put into reviewing my work. Our meetings were incredibly educational for me. Also, I want to thank Matthieu de Schipper for his critical questions during the committee meetings. Many thanks also to Kübra, Jitske, and my parents for their unconditional support and for motivating me during some of the long days. I want to thank my friends for getting my mind off the thesis and a special thanks to Will and Furkan for improving my writing.

Dear reader, please be aware that the ultimate solution to this crisis is not to just clean all the plastics out of the environment, but to prevent making it end up there in the first place. Mismanagement of plastics starts with the individual. Thus, taking a moment to consider how you dispose it can make a huge difference. Lastly, I want to thank you for taking the time to read this thesis. I hope you find as much insight while reading this as I had preparing and writing it in the last couple of months.

J. E. Swagemakers
Rotterdam, October 2022

Summary

Accurately predicting surface transport in the ocean is crucial for estimating the course of marine pollution, which is considered one of the most pressing environmental issues of the 21st century. In the ocean, floating marine pollution is transported by several mechanisms, including waves. Companies specialised in removing plastic use numerical models to predict the course of marine pollution. The wave component included in these numerical models is limited to the transport of non-breaking waves. However, Deike et al. (2017) and Pizzo et al. (2019) indicated that the transport induced by non-breaking waves is enhanced by breaking waves. Thus, in this thesis, the contribution of the transport from breaking waves to the total wave-induced transport at the surface of a deep-water unidirectional irregular sea is estimated. To do this, first, experiments are conducted to study the contribution of the wave-breaking-induced drift to the total wave-induced drift. Secondly, a theoretical model is developed. The model computes the transport of individual breaking wave groups from surface elevation measurements of a deep-water unidirectional irregular sea. The contribution of the wave-induced transport from breaking waves to the total wave-induced transport is defined by an enhancement factor. This enhancement factor shows how much the wave-induced surface transport without breaking waves is enhanced by the transport of breaking wave groups.

The contribution of breaking waves to the total wave-induce transport is first determined from experimental results. Experiments were performed in the Atlantic Basin of Deltares. In this facility, unidirectional irregular waves were generated in deep water. An overhead camera filmed the behaviour of quasi-Lagrangian particles floating on top of the waves. The particles were tracked using OpenCV and their trajectories were obtained. The trajectories were undistorted using the camera's intrinsic parameters and calibrated into the physical plane of the Atlantic Basin by inverting the transformation matrix. The camera intrinsic parameters and transformation matrix were calculated using a series of images of a 75 mm square calibration grid floating on the still-water surface of the Atlantic Basin. The trajectories were low-pass filtered and a velocity threshold was imposed to extract the breaking waves. The transport from the extracted breaking waves was defined.

Secondly, to complement to the experimental results, a theoretical model is developed. The theoretical model is an extension of the relationship from research by Sinnis et al. (2021), who defined a transport relationship for isolated breaking wave groups based on the spectral bandwidth and the linear slope of the wave groups. The developed theoretical model applies the transport relation from Sinnis et al. to breaking wave groups from surface elevation measurements of deep water irregular seas. To do this, an approximation was made of the surface elevation spectrum by multiple Gaussian wave groups. From the Gaussian wave groups, the spectral bandwidth and the linear slope could be determined. Breaking waves were identified based on a steepness threshold for wave groups. The transport was calculated for all individual breaking wave groups.

Furthermore, the theoretical model was validated by comparing the number of breaking waves, the strength of the breaking events, and the enhancement factor with the experimental results. The results showed that all values were in the same order of magnitude and that the transport induced by breaking enhanced the surface transport for non-breaking waves by a factor up to 1.5. Besides, a sensitivity analysis of the relevant parameters showed that the error margin remains within 10% of the mean. In conclusion, the theoretical model gave reasonable predictions of the contribution of the wave-breaking-induced transport in a unidirectional irregular sea. Hence, this framework can be fruitful grounds for further extension of the breaking-induced drift in the ocean.

Table of contents

List of symbols

Parameter	Unit	Description
a	m	Amplitude
c_g	m/s	Group velocity
d	m	Water depth
$E(f)$	m^2/Hz	Spectral density
f	Hz	Frequency
f_c	Hz	Central frequency
f_0	Hz	Peak frequency
g	m/s^2	Gravitational acceleration
H	m	Wave height
H_s	m	Significant wave height
H_{m_0}	m	Spectral significant wave height
k	m^{-1}	Wave number
k_c	m^{-1}	Central wave number
k_0	m^{-1}	Wave number carrier wave
L	m	Wave length
m_0	m^2	First order spectral moment
S	-	Linear slope of the wave group
S_{tr}	-	Threshold linear slope of the wave group
T	s	Wave period
T_p	s	Peak wave period
$\bar{u}_{st}$	m/s	Stokes drift monochromatic wave
$\bar{u}_{st,ch}$	m/s	Characteristic Stokes drift
$\bar{u}_{st,\eta,tr}$	m/s	Stokes drift imposed threshold
$\bar{u}_{st,\eta}$	m/s	Stokes drift derived from surface elevation
$\bar{u}_{st,\eta,f<3.5f_0}$	m/s	Truncated Stokes drift derived from surface elevation
$\bar{u}_{0.2\ EMS}$	m/s	Average current 0.2 m below the mean water level
$\langle\bar{u}_{ob}\rangle$	m/s	Average object drift from the trajectories of the particles
$\langle\bar{u}_{br,ob}\rangle$	m/s	Average breaking induced drift from the trajectories of the particles
$\bar{u}_{ob,w}$	m/s	Average object drift of a particle during 1 wave oscillation
$\delta x_{od,w}$	m	Total travelled distance of a particle during 1 wave oscillation
$\delta x_{st,ob}$	m	Stokes transport of a particle in a nonbreaking wave
$\delta x_{br,ob}$	m	Transport of a particle in a breaking wave
$\delta x_{st,\eta,g}$	m	Stokes transport for a nonbreaking wave group
$\delta x_{\eta,br,g}$	m	Transport for a breaking wave group
Δ	-	Spectral bandwidth
ϵ	-	Wave steepness
ϵ_{ch}	-	Characteristic wave steepness
ϵ_{tr}	-	Threshold wave steepness
η	m	Surface elevation
ω	rad/s	Angular frequency
χ_{ob}	-	Drift enhancement factor from particle trajectories
χ_η	-	Drift enhancement factor the wave groups

1

Introduction

Marine pollution has become one of the most pressing environmental issues of the 21st century. The largest and most widespread source of marine pollution is plastics accounting for 60-95% of the global marine litter (Schnurr, et al., 2018). Millions of tonnes of plastics are thrown (intentionally or unintentionally) into the oceans each year (Andrady, 2011). This number is expected to increase as the production of disposable plastics overwhelms the world's ability to deal with them. Plastic is highly durable and takes centuries to degrade (Oliveira, et al., 2020). Upon entering the water, plastic both releases and absorbs pollutants, making it extremely dangerous for the marine environment. Through the food chain, these pollutants and chemicals contaminate human consumption causing health problems (Wang, et al., 2016). The international community has acknowledged the urgency of the issue. In 2017, all UN-countries agreed to intensify their efforts in reducing plastic pollution in the ocean and this was incorporated into multiple sustainable development goals. Consequently, more funding became available for companies specialized in removing plastics from the ocean. These companies predict where the floating plastics accumulate. They do this by measuring wind, waves, and currents, which are responsible for the distribution of marine pollution across the oceans; therefore, to remove plastics from the marine environment, an accurate prediction of the surface transport in the ocean is required (Sherman & van Sebille, 2016; Welden & Lusher, 2017; Lermusiaux, et al., 2019).

The physical mechanism contributing to the surface transport at the centre of this research is waves: particularly breaking waves. The surface wave-induced Lagrangian drift plays a fundamental role in the dynamics of the surface layer of the ocean (Pizzo & Melville, 2019) and has a significant practical application in predicting the transport of flotsam, jetsam, and pollution (van den Bremer & Breivik, 2017). For non-breaking waves, drift is induced by the orbital motion of water particles beneath the surface of the waves. The trajectories of the water particles do not fully close as they spend more time in the forward-moving region under the crest where the velocity is higher than in the backward-moving region under the trough, resulting in a Lagrangian-mean velocity in the direction of the waves known as the Stokes drift (left in Figure 1.1). For each wave at the surface of the ocean, the Stokes drift and its direction can be determined. This knowledge is used to improve the prediction of plastic movement in the ocean.

For breaking waves, the theoretical concept is rather poorly understood. The reason for this is that it involves highly non-linear hydrodynamics. Additionally, acquiring quantitative observations for research purposes is difficult to carry out (Holthuijsen, 2007). During breaking events, Lagrangian particles at the surface travel much farther in space as can be seen on the right in Figure 1.1. This distance is almost an order of magnitude larger than for non-breaking waves since fluid particles in the breaking front travel approximately with the phase speed of the wave (Stansell & MacFarlane, 2002). Thus, predicting the surface transport solely based on non-breaking waves in wave fields where breaking waves occur gives less accurate results of the wave-induced surface transport. However,

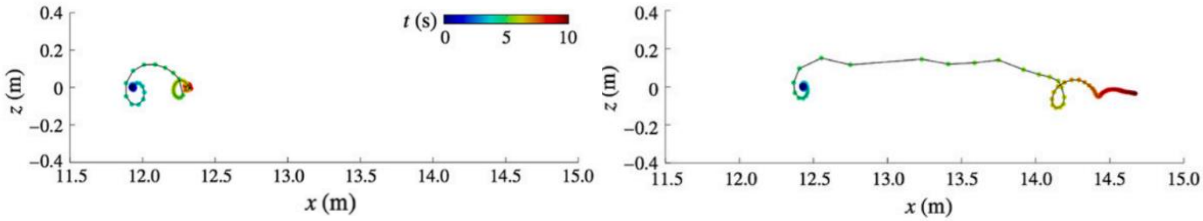

Figure 1.1 On the left a side view of a particle experiencing the Stokes drift and on the right a particle experiencing a breaking wave (Pizzo, Melville, & Deike, 2019)

accurately capturing the influence of small-scale features like breaking waves requires large computational capabilities, which most modern computers do not have. Consequently, breaking waves are not taken into account in most models predicting the surface transport.

Summarizing, predicting the course of floating marine debris is of critical importance to preserve marine environments. The contribution of the wave-breaking-induced Lagrangian drift is of significant importance for more accurate predictions of wave-induced surface transport. However, due to the complex hydrodynamics of breaking waves, they are not incorporated in models predicting the wave-induced transport. This research aims to characterize the Lagrangian drift induced by breaking surface waves for a deep-water random sea state, in which deep-water implies that the surface waves are unaffected by the bottom.

1.1 Background information on breaking waves in the ocean

To get a better understanding of the wave-breaking-induced transport in the ocean a literature study is performed. The literature study starts by giving the basic principles in the description of ocean waves and discusses the tendency of ocean waves to form wave groups. Thereafter, different types of deep-water breaking waves and their characteristics are discussed. Lastly, existing research and relationships into the transport of deep-water breaking waves are summarised. From this study, the knowledge gap is determined and a problem description is formulated. This section aims to give essential background information on breaking and non-breaking waves in the ocean, more in-depth literature is present in the individual chapters.

1.1.1 Description of ocean waves

Waves in the ocean are predominantly generated by the wind blowing over the surface. The wind creates friction between the air and the water resulting in a rise and fall of the surface elevation. The waves can be described in two ways: the Eulerian and Lagrangian approaches. The Eulerian approach concerns the waves at a fixed location over time. Measurements from a wave gauge are for example used for the Eulerian approach. The wave gauge measurements give a one-dimensional surface elevation time series at a fixed location. An indication of a wave gauge measurement is given by the blue line in Figure 1.2. A wide range of wave shapes can be observed with typical wave characteristics like the crest, trough, and wavelength. However, the measured waves are captured in a single moment in time, while individual waves in the ocean continuously change shape. Therefore, the Eulerian approach is better at describing the properties of the wave field instead of individual waves. Another way of describing ocean waves is through the Lagrangian approach, which describes the motion of propagating waves. Lagrangian measurements are carried out by floaters such as free-floating buoys measuring the surface elevation as a function of time and time-varying horizontal position. Their horizontal position is influenced by waves, wind, and currents. Hence, Lagrangian measurements are especially useful for studying wave-induced transport in the ocean (Olbers, et al., 2012).

Individual waves change over time and are all different. Therefore, describing the waves based on the wave height and length is not ideal. Consequently, a description of the wave field is used instead. This

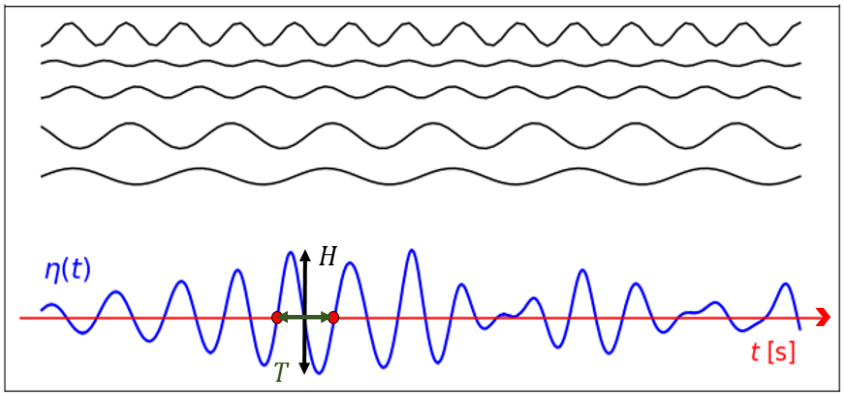

Figure 1.2 In blue the surface elevation time series which is composed of multiple harmonics shown in black above.

description of the surface elevation is made using the random phase/amplitude model. This is the basic model to describe the moving surface elevation $\eta(t)$ in deep-water conditions. The surface elevation is assumed to be composed of the sum of a large number of independent stationary harmonic components (i.e. a Fourier series), each with a constant amplitude a_i, phase α_i, and frequency f_i (Figure 1.2). The number of harmonic components N is dependent on the frequency interval $\Delta f = 1/D$, where D is the duration of the surface elevation time series. In reality, however, the harmonic components are not completely independent. Nevertheless, in deep-water conditions, these interactions are weak and can be ignored, making the model the basic model to describe ocean waves (Holthuijsen, 2007). The surface elevation $\eta(t)$ is reproduced by:

$$\eta(t) = \sum_{i=1}^{N} a_i \cos(2\pi f_i t + \alpha_i) \tag{1.1}$$

The individual waves in a surface elevation time series $\eta(t)$ can be defined using a zero-up crossing method. In this method, a wave is defined by the profile of the elevation between two successive upward zero-crossings of the surface elevation with the mean water level. This is illustrated by the red dots in Figure 1.2. The wave height H is then defined by the difference between the highest point in the crest to the lowest point in the trough and the wave period T is defined as the time between the two successive up-crossings with the mean water level. Additionally, from the surface elevation time series, individual wave heights, and wave periods statistics can be applied to characterize the wave field. These statistics will be discussed in chapter 4 focusing on experimental data analysis.

Furthermore, the amplitude of each harmonic component is used to compute the variance $0.5a_i^2$. The variance is a more relevant quantity than the amplitude as it is proportional to the energy of the waves, which in turn is related to the wave-induced velocity of a water particle (Holthuijsen, 2007). For each frequency, the variance can be estimated and a variance density spectrum results from:

$$E(f) = \lim_{\Delta f \to 0} \frac{1}{\Delta f} E\{\frac{1}{2} a_i^2\} \tag{1.2}$$

The energy spectrum is acquired by multiplying the variance of the surface elevation $E(f)$ by the density of water ρ and the gravitational constant g. In the variance density spectrum, the expected amplitude for each frequency is given from which different sea states can be identified. When the distribution of the variance density spectrum is narrow, the wave field is described by a small range of frequencies indicating that the waves are approximately the same (i.e. regular waves), while for

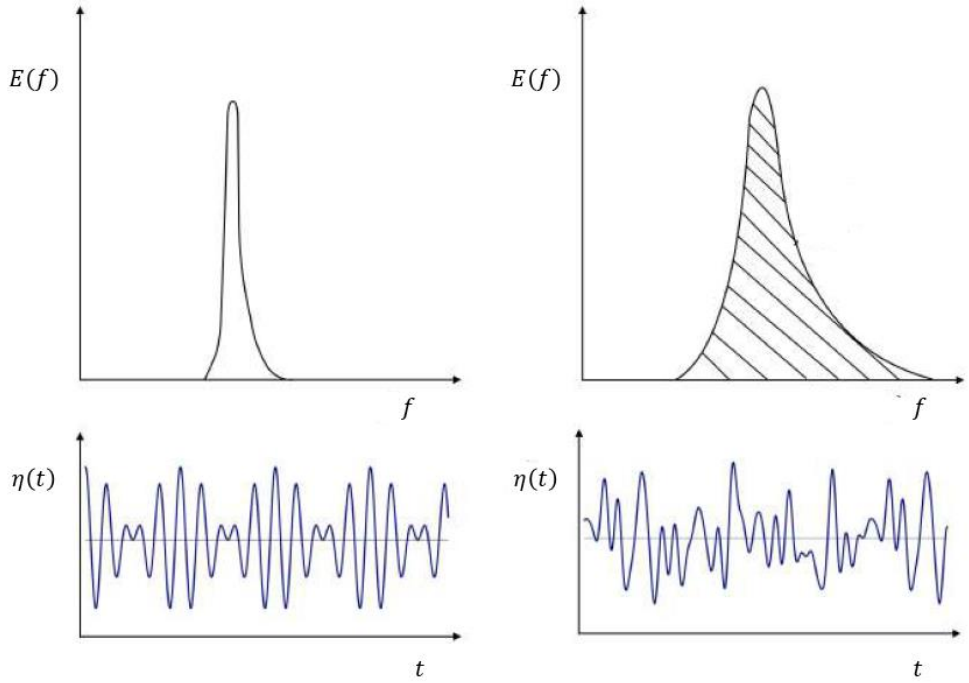

Figure 1.3 Variance density spectrum $E(f)$ and surface elevation $\eta(t)$. (Left) A narrow spectrum corresponding to a 'regular' sea. (right) A broad spectrum corresponding to an irregular sea. (Doeleman, 2019)

widely distributed wave spectra multiple frequency components interact, which indicates an irregular wave field (Figure 1.3).

In the ocean, deep-water waves have a natural tendency to form groups. Wave groups are sequences of waves with wave heights higher than a threshold value H_{gr} and with a length defined by the number of waves. They occur do the reinforcement between individual wave components. A wave group can be formed by 2 harmonics traveling in the same direction with slightly different frequencies (Figure 1.4). At the location of reinforcement, the wave height is increased. Wave groups can therefore contribute to the occurrence and strength of breaking events. The velocity of the individual waves within the wave group travels twice as fast as the wave group itself. As a result, the individual waves travel to the front of the group and disappear, while at the tail of the group a wave is formed.

Goda (1970) was the first to give a simple methodology for analysing the presence of wave groups in random seas. In his research, Goda used the length of runs of waves to measure wave groups and defined a spectral peakedness parameter, which indicated that larger wave groups are related to higher values of spectral peakedness. The spectral peakedness is a measure indicating whether the ocean wave field is made up of many or a few different frequencies. When the wave field is more peaked, the combination of waves reproducing the surface elevation have their frequencies close to the central frequency and hence contain only a few frequencies. The Goda methodology has been the most widely used to analyse wave groups from real ocean records (Ramasamy, et al., 2015). Rye (1982) analysed methodologies and observations of wave groups in random seas and concluded that all of the significant characteristics of wave groups in records of sea surface elevation could be obtained from the energy spectrum.

There are many definitions of wave groups. Longuet-Higgins (1984) used the envelope approach to analyse the wave groups. In this approach, a wave group is considered to be composed of all waves exceeding a specified elevation threshold during two consecutive up-crossings of an envelope. A downside of this method is that it also resulted in wave groups only having a single wave crest exceeding the threshold. Another method to identify wave groups is by their energy. Funke &

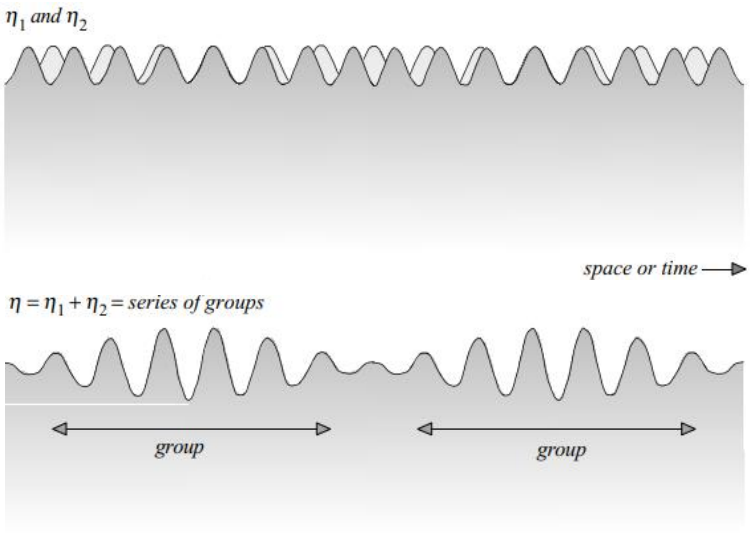

Figure 1.3 Two harmonics with surface elevation η reinforce each other to form two wave groups (Holthuijsen, 2007)

Mansard, 1979 applied smoother instantaneous wave energy history (SIWEH) to isolate wave groups within a wave record. In this study, the authors proposed a new simulation program for random waves based on a target wave power spectrum and a SIWEH sequence to obtain the wave series with a given group structure. Battjes and van Vledder (1984) validated the identification methods and confirmed that groups can correctly be analysed from one-dimensional wave records in deep water. Although real ocean waves are non-stationary by nature and the conventional Fourier analysis assumes a stationary stochastic process.

1.1.2 Characterizing the wave breaking phenomenon

Quantifying the wave-breaking-induced transport requires the identification of breaking waves in a wave field. Generally, a wave-breaking event is described by a water particle near the wave crest that exceeds the velocity of the wave itself and falls down the front of the wave. In the ocean, two types of breaking events can be classified. The strongest type is the plunging breaker, wherein the wave starts to overturn and forms a forward-moving sheet of water which plunges into the water in front resulting in air entrainment and eddies. Plunging breakers are common at beaches but much less in deep water. Most breakers in deep water are of the spilling type, which is characterized by a white breaking front falling down the front face of the wave. The familiar white cap is a result of entrained air bubbles and drops created at the surface. Nevertheless, the breaking of short gravity waves also occurs without air entrainment in the form of microscale breakers (Banner & Peregrine, 1993).

The initiation of spilling breakers in deep water is not completely clear. In most approaches, the geometry of the waves is the characteristic used to detect and quantify breaking waves. However, the presence of wind may locally create extra shear on the surface of the waves, which leads to a reduction of the maximum wave height at breaking compared to a steady wave (Phillips & Banner, 1974). Additionally, a current against the propagation direction of the waves can be generated by previous breaking waves. This current may steepen the waves leading to earlier breaking events. Furthermore, ripples are present at the surface of the ocean. Large wave crests are catching up with these ripples. The ripples steepen the larger waves which overtake them. Popat (1989) showed that for a wide range of gravity waves the small ripples that cause steepening of the waves also contribute to the initiation of spilling breaking. Thus, characterizing the initiation of breaking waves is a complex phenomenon which remains difficult to accurately predict based on its geometry. However, it does indicate when breaking is likely to occur

1.1.3 Review of literature on wave-breaking-induced transport

The analysis of the wave-breaking phenomenon in the ocean has been going on for more than a century. Series of laboratory experiments, deployment of instrumentation at sea, and numerical simulations have led to a several empirical and theoretical discoveries. Due to variability in measurements of breaking waves, a prediction of the transport of breaking waves is not universal. Progress has been made as more accurate and extensive measurements have become available. In this section, relevant findings into deep-water wave-breaking-induced transport at the surface of the ocean are presented.

Deike et al. (2017) used direction numerical simulations to study wave-breaking-induced mass transport. In that study, wave groups were described by two-phase air-water Navier-Stokes equations. Additionally, a simple model was proposed to estimate surface transport by breaking. They found that surface transport depends linearly on the wave slope and the characteristic phase velocity. A scaling factor was added to match the model results with the direct numerical simulations. Pizzo et al. (2019) applied this quantitative model from Deike et al. to estimate the Lagrangian transport by non-breaking and breaking deep-water waves at the ocean surface. They extended the model with wave-breaking statistics in the field deduced by Philips (1985) along with environmental conditions such as the wind input. Their results showed that the drift induced by breaking can be as much as 30% of the classical Stokes drift and becomes more important with increasing significant wave height (Pizzo, Melville, & Deike, 2019).

Deep-water waves often occur in groups (i.e. sequences of waves). In the laboratory, this phenomenon is simulated using a dispersive focusing technique. The initiation of longer faster waves and shorter slower waves is modified in such a way that the group of waves become superimposed at a specific location and break (Rapp & Melville, 1990). Using the dispersive focusing technique, Lenain, Pizzo, and Melville (2016), analysed the breaking of individual wave groups. They found that breaking waves greatly enhances mass transport compared to non-breaking focusing wave groups and that the strength of the surface drift increased sharply for larger slopes of the wave groups. Sinnis et al. (2021) used the dispersive focusing technique to determine the dependence of the spectral bandwidth from the wave group to the surface transport for non-breaking and breaking deep-water waves. This work was an extension of the model from Deike et al. (2017). They found that the surface transport of breaking waves is inversely proportional to the spectral bandwidth and proposed a model for the transport of breaking wave groups, which incorporates the spectral bandwidth, the wave slope, and the breaking threshold slope of the wave group.

In the ocean, Brown et al. (2019) observed the kinematics and statistics of breaking waves by using SWIFT buoys. They deployed surface wave instrumentation floats with high sampling frequency by helicopter ahead of five large storms. The strength of the breaker appeared to increase with the wave height, wave period, and steepness of the wave and decreases with the spectral bandwidth. The latter was confirmed by recent research from Sinnis et al (2021). In their research, Sinnis et al. developed a transport relationship for a breaking wave group taking into account the bandwidth of the wave group, central frequency, linear prediction of the slope at focusing, and breaking threshold slope of the wave group. Their relationship was evaluated with data from archived and new laboratory experiments and an agreement was found for the transport of isolated breaking wave groups.

1.2 Problem description

Despite extensive study of wave breaking phenomenon, it is still not possible to predict the surface transport for breaking deep-water waves in the ocean. The most recent research into wave-breaking-induced drift was conducted by Sinnis et al. (2021). In this study, isolated wave groups were used in

the experiment; however, single wave groups are not representative of a real sea state. Waves in the ocean consist of many wave groups with different periods, directions, amplitudes, and phases. Furthermore, the wave-breaking variability of real sea states is significant. In literature, the threshold for breaking waves and wave groups shows great variability. Research under more realistic conditions of the ocean surface is required for a better understanding of the breaking-induced drift. Therefore, an extension of the transport relationship from Sinnis et al. is necessary to be valid for a real sea state.

In the existing literature, multiple parameters are discussed to be of importance to the transport of wave breaking. The effect of the bandwidth, the linear slope, and the empirically measured breaking-threshold-slope of the wave group have all shown to be relevant variables for transport and dissipation in breaking waves (Sinnis et al., 2021). Experiments have shown that the drift increases linearly with increasing linear slope and decreasing spectral bandwidth of the wave group; however, current transport relationships about the wave-breaking-induced drift in random deep-water sea states do not take into account the bandwidth of the wave group. Those relationships have yet to be applied to the wave groups of a deep-water random sea.

Lastly, removing plastics from the ocean has a large ecological and economical value. Predicting where plastic accumulates is therefore crucial for its removal from the environment. Despite its significant contribution to surface transport, wave breaking is not taken into account in any dispersal models estimating near-surface currents, and likewise in particle tracking models (Wichmann et al., 2019; Mansui et al., 2015; Liubartseva et al., 2018). The reason for this is that coupling the smaller scale, numerically complex, breaking phenomenon to a larger scale dispersal model presents challenges. The computational capability of modern computers is not sufficient to resolve the calculations of the breaking waves resulting in very large computational times. However, accurately capturing the influence of small-scale features like breaking waves is necessary for developing more reliable predictive models in a scaled-up framework. Therefore, a simplification of the transport for breaking waves is required.

1.3 Scope

Several physical mechanisms play a role in the transport at the ocean's surface including waves, large geostrophic flows and wind drift. In this research, we specifically focus on the role of the wave field. As previously discussed, the wave induced Lagrangian drift is comprised of the Stokes drift and the wave-breaking-induced drift. The main focus of this research is the wave-breaking-induced drift. Besides, vertical transport processes caused by breaking events reaching into the water column are not taken into account. Additionally, the wave-breaking-induced transport studied here is in oceanic conditions. Therefore, deep-water wave conditions are taken into account meaning that the water depth d is much larger than the wave length L (i.e. $kd >> 1$, where $k = \frac{2\pi}{L}$ is the wave number).

Furthermore, the wave field of the ocean is multidirectional; however, the experiments performed in the Atlantic Basin at Deltares consist of a unidirectional wave field. Therefore, the project is limited to studying unidirectional wave fields. Lastly, there are 4 basic types of breaking waves. These are plunging, spilling, collapsing and surging breakers. In the ocean the breaking waves are mostly limited to the spilling type (Heebneret al., 1997). Hence, all breaking waves are assumed to be of the spilling type.

1.4 Research objective and questions

In this master thesis, I will develop a theoretical model to predict the breaking enhanced drift in random seas. I will do this using the relationship of the breaking enhanced drift for isolated wave groups by Sinnis et al. (2021). The theoretical model will be an extension of the breaking-induced

transport relationship by Sinnis (2021). To validate the theoretical model, I will conduct deep-water random sea experiments in the Atlantic Basin at Deltares as part of an existing large-scale experimental campaign. Based on this theoretical model a software tool is developed that calculates the enhancement factor of the Stokes drift for random sea states. To reach this objective, the main research question is:

What is the contribution of breaking waves to the wave-induced Lagrangian drift at the surface of a deep-water unidirectional random sea?

In order to answer this question, 3 sub-questions need to be answered first. These sub-questions are:

1. *How can the wave-breaking-induced drift be determined from experimental data?*
2. *How can a model be defined to determine the wave-breaking-induced drift?*
3. *How accurate are the model results compared to the experimental results?*

1.5 Approach and thesis outline

This thesis consists of a literature study and an experimental campaign. Part of the literature study is presented in the background information discussed in this introductory chapter. More literature regarding wave-induced transport is present throughout the chapters. The background information defined the knowledge gap, which lies in estimating the wave-breaking-induced transport in deep-water irregular seas. Therefore, the main research question defined in section 1.4 is whether the contribution of breaking waves to the wave-induced Lagrangian drift at the surface of a deep-water unidirectional random sea can be quantified.

To do this, first, experiments were conducted in the Atlantic basin of Deltares. In these experiments, quasi-Lagrangian particles were tracked, which were floating on the surface of deep-water unidirectional irregular wave fields. The measured trajectories resulting from the experiments require processing, whereafter they are analysed. In the analysis of the experimental data, the drift from non-breaking and breaking waves is identified. From the experimental analysis, research sub-question 1 is answered.

Secondly, in addition to the experimental results, a theoretical model is developed to studied whether the wave-induced transport for breaking and nonbreaking waves can be estimated from measured surface elevation data. To do this, the transport relationship from Sinnis et al. (2021) was used, wherein a relationship for the transport of breaking wave groups was defined based on the wave group characteristics. A literature study is used to extend the relationship from Sinnis et al. to wave groups in irregular wave fields. This extension is based on the approximation of the measured surface elevation spectrum by Gaussian wave groups to which the transport relationship from Sinnis et al. can be applied. The extension of the transport relationship from Sinnis et al. is programmed in Python and applied to the surface elevation data from the Deltares experiment. Consequently, research sub-question 2 is answered.

To validate the results of the contribution of breaking waves to the wave-induced Lagrangian drift for a deep-water random sea, the experimental data and the theoretical model results are compared. The validation results in the answering of research sub-question 3. Besides, a conclusion is drawn whether the theoretical model is a good approximation of the wave-breaking-induced drift. Lastly, the main research question is answered based on the results from the theoretical model and the experimental campaign.

The structure of this report is based on the approach. The introductory chapter addresses the relevance of the research. Additionally, the approach to reach the objective is presented within a specified scope. The setup of the experimental campaign at Deltares is described in Chapter 2. The processing of the experimental data is in Chapter 3 and the analysis of the experimental data is in Chapter 4. Chapter 5 discussed the description and application of the theoretical model. In Chapter 6, the results of the experimental campaign and the theoretical model are discussed and compared. The limitations of the research and the assumptions regarding the model are reflected. Finally, in Chapter

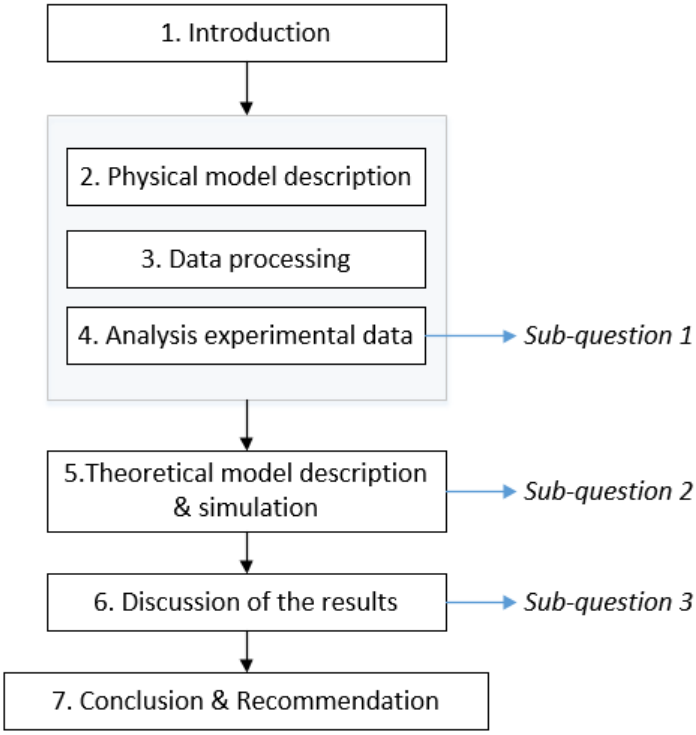

Figure 1.4 Schematical overview of the structure of the thesis

8 conclusions are drawn regarding the research questions and recommendations are given for further research. In Figure 1.4 a schematical overview of the structure of the thesis is given.

2

Laboratory experiments

This chapter describes the laboratory experiment. The goal of the experiments is to investigate wave-breaking-induced transport in oceanic conditions. To do this, plastic particles were dropped in the Atlantic Basin of Deltares wherein an oceanic wave field was generated. The behavior of these plastic particles experiencing wave-induced surface transport was tracked. The experiments were part of a large-scale experimental campaign launched by the European Space Agency (ESA). In this chapter, first, a general description is given of the Atlantic Basin. Thereafter, the equipment used to measure the hydraulic conditions is reviewed. Lastly, the input conditions are described and an overview of the conducted tests is presented.

2.1 Facility description

Quantitative data on the wave-breaking-induced transport is gathered from measurements at the Atlantic Basin test facility in the Deltares Hydrohall. The Atlantic Basin is a flume of 8.7 m wide and 75 m long, in which both waves and currents can be generated. The combination of a wave generator with a pumping system allows for a realistic simulation of oceanic waves interacting with a current. The waves are generated with a segmented piston-type wave board, which consists of twenty wave paddles installed at one end of the basin. The wave board can generate any wave spectrum with a maximum significant wave height of 0.25 m for irregular waves, wherein the significant wave height is the average of the highest third of the waves in the generated wave field. The maximum wave height for regular waves is 0.45 m. At the other end of the basin, a beach is located (Figure 2.1). Furthermore, a current can be generated either following or opposing the waves using three pumps; each with an individual capacity of 1 m^3/s. The pumps together with three adjustable weirs at both ends of the basin are used to keep the still water level at 1 m. The test section is located at the center of the basin with an access bridge to mount instrumentation. The bottom of the test section is filled with compacter non-cohesive sand with a $d_{50} \approx 150$ µm.

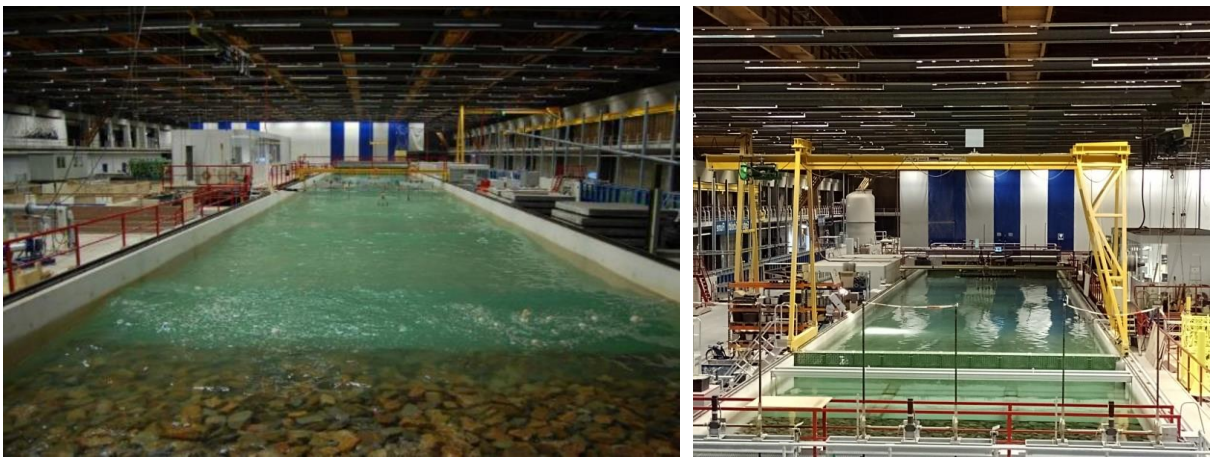

Figure 2.1 Overview photos of the Atlantic Basin in the Deltares Hydrohall taken from the dissipative beach towards the wavemaker.

2.1.1 Wave reflection reduction

The Atlantic Basin is of infinite length, meaning that the waves are reflected at the end of the flume and will propagate in the opposite direction toward the wave paddle. These reflected waves distort the incoming waves. Therefore, the aim is to reduce the reflection of the waves. To reduce the incoming waves a beach is located at the end of the basin. The beach consists of large stones so the waves are optimally absorbed and dissipated. Nonetheless, some wave reflection still occurs. The wave height of the reflected wave was analysed by Deltares. This was done using three wave gauges which were positioned at fixed intermediate distances and the formulation for wave reflection by Mansard and Funke (1980). It was found that the reflected wave height was about 10-20% of the incoming wave height. For significant wave height input cases of 5 and 9 cm, the reflected waves were absorbed by the wave paddle which was equipped with active reflection compensation (ARC). ARC detects unwanted surface elevations or depressions and absorbs this energy width additional forward and backward movements, However, ARC was not possible for significant wave height input cases of 13 and 17 cm due to limitations of the maximum length of the paddle sweep. Thus, second-order subharmonic waves are reflected from the beach and the wavemaker. The reflected subharmonic waves have a significant effect on the mean flow fields driven by waves, which will result in errors when calculating the displacements of the particles discussed in chapter 4 (Li & Li, 2021). The long subharmonic waves decay slowly in the flume, which cannot be eliminated in the laboratory. Therefore, experiments performed later in the day have larger errors induced by the subharmonic waves. Additionally, these second-order waves lead to the expansion of the linear waves' energy spectrum.

2.2 Setup of measurements and equipment

An overview of the flume layout and the location of the measurement equipment in the basin are shown in Figure 2.2. The data is collected using three different instruments: wave gauges are used to measure the surface elevation and hence the wave heights, sensors equipped with floaters are used to measure the surface elevation, and electromagnetic velocity sensors (EMS) are installed to measure the current. Additionally, to measure the wave-induced transport from breaking waves quasi-Lagrangian plastic spheres were dropped approximately 2 m before the test section. The plastic spheres accurately followed the wave-induced surface transport. A particle dispenser was used to create specific densities of particles in the test section. The movement of the plastic particles was tracked by a downward-looking camera. In the following sections, the equipment used for measuring and regulating the hydraulic conditions is briefly discussed. All measurement equipment was calibrated by Deltares in advance of the experiments.

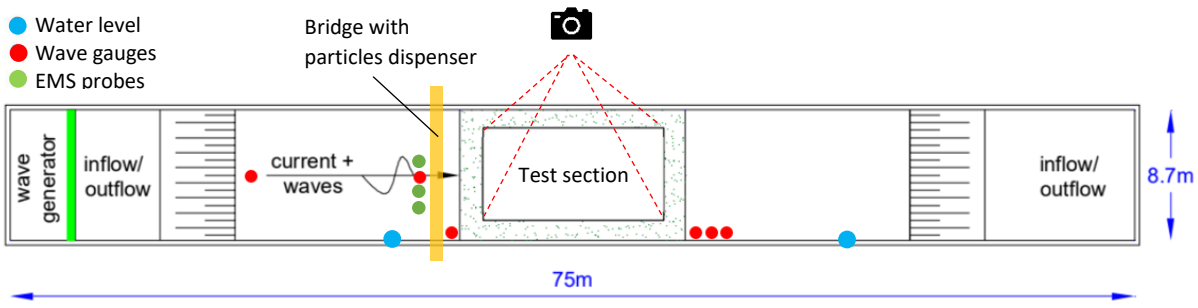

Figure 2.2 Schematical overview of the Atlantic basin with the location of the wave gauges, EMS probes, and water level gauges.

Figure 2.3 Measurement equipment used in the physical model (left) the electromagnetic velocity sensor, (center) the wave gauge, and (right) installed wave gauges at the side of the basin.

2.2.1 Water level

The water level in the facility was measured through two position sensors equipped with highly accurate Temposonic R-series floaters, which are mounted along the wall of the facility. These floaters have an accuracy of 0.1 mm. Based on the water level measurements, the weirs and pump capacity were regulated to maintain the water depth of 1 m.

2.2.2 Wave height

The wave heights in the physical model were measured at different locations by wave gauges of the resistance type, which are compensated for conductivity (temperature) variations of the water through a reference electrode. The wave gauges consist of two parallel stainless steel rods and a platinum reference electrode at the bottom of the rods. The wave gauges measure the offset from the mean surface in time with an accuracy of about 0.5 mm. In this experiment, the measurement frequency of the wave gauges is 256 Hz and 64 Hz.

2.2.3 Eulerian currents

Eulerian current velocities were measured using three electromagnetic current sensors (EMS). This sensor consists of one stainless steel with a probe at the bottom. The probe has a diameter of 30 mm under which the velocity is measured in 2 horizontal directions (Figure 2.3). The accuracy of the velocity sensors is about 1 cm/s. The current velocities were measured at three different depths and at the same horizontal position from the wavemaker ($(x,\ y)$ = (14.2, 4.05-4.65) m). This allowed for the estimation of the basin-specific Eulerian-mean flow for each experimental condition at fixed depths of z = -20, -30, and -50 cm with z = 0 the still-water level. In this experiment, the measurement frequency of the electromagnetic current sensor is 256 Hz and 64 Hz.

2.2.4 Flow rate

At the end of the basin, leakages occur. Therefore, a low flow is added to the facility to compensate for the losses and regulate the water level. This flow rate is induced by a single pump, which is set to 0.03 m^3/s. The water level was then kept stable by adjusting the weirs. During the experiment, the flow rate was measured using the electromagnetic flow meters (EMF) which were part of the facility.

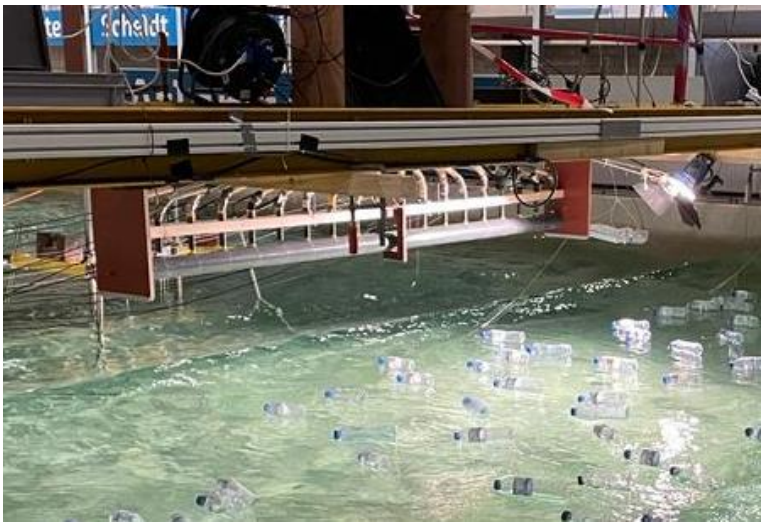

Figure 2.4 The particle dispenser mounted to the bridge at the center of the basin 16.7 m from the wavemaker.

Figure 2.5 The plastic spheres used in the experiment.

2.2.5 Particles dispenser

The plastic spheres were released in the basin using an automated dispenser mounted to the bridge, which was located at the centre of the basin and approximately 2 m before the camera's field of view (Figure 2.4). The dispenser has a width-wise span of 3.0 m and twenty tubes which were equally spaced at 15 cm. The tubes placed the spheres on a rotating cylinder from where the spheres were periodically dropped into the basin. The rotational speed of the cylinder determined the time step for which the spheres were dropped in the basin and, thus, determined the density of spheres in the area of interest. The time step was calculated based on the required density and the Stokes drift resulting from the wave conditions during the test. However, the time step for some densities was so large that the video footage of the surface elevation did not record any particles as they had already left the frame of the camera. Therefore, tubes were taped off to increase the time step without changing the density. The outer tubes and three tubes in between the open tubes were tapped off. Consequently, collisions of particles was reduced even further, which was positive for the tracking process discussed in chapter 3. The frequency at which the particles are dropped is shown in Table 2.1. Furthermore, different concentrations of spheres in the test area were used. The spheres were released in the basin in an automated manner by the sphere dispenser. This dispenser released the spheres with a predefined time interval. The time step was calculated based on the required density and the Stokes drift resulting from the wave conditions during the test. This way, the required concentrations could be calculated. Table 2.1 gives the concentrations of spheres for the different experiments.

Table 2.1 shows the number of open tubes from which the particles reach the dispenser and the time interval Δt with which they are dropped in the basin for tested significant wave height condition H_s.

H_s [cm]	Open tubes [#]	Δt [s]	Particle concentration [g/cm^2]
5	5	40	10
9	5	20	20
13	19	28	18
17	5	40	10

2.2.6 Plastic particles

The particles dropped in the Atlantic basin were spheres made of polypropylene with a diameter in the range of 19 and 20 mm. The weight of the sphere varied between 3.5 to 3.6 g. The density of the particles was in the range of 872 and 974 kg/m^3. The experiments were carried out in freshwater (998 kg/m^3). Therefore, the particles follow the motion of the fluid, but remain afloat and hence are detectable by the camera. The colour of the spheres is yellow, which makes them more easily tracked by the camera. The plastic particles are shown in Figure 2.5.

2.2.7 Video camera

The displacement of the particles was measured from images of a downward-looking camera shooting at a rate of 24 frames per second. A Z-cam camera was mounted at a height of 11.9 m above the basin, allowing it to capture an area of about 8 m along the length of the basin and 6 m of its width. The footage shows a top view of the Atlantic Basin with different wave heights and the yellow plastic spheres randomly distributed floating on top of the surface.

2.3 Test configurations

This section defines the set of parameters used to generate oceanic conditions in the Atlantic Basin through the energy spectrum. First, it is described how oceanic waves differ from coastal waves. Secondly, the energy spectrum of irregular deep-water waves is discussed.

2.3.1 Ocean wave conditions

Waves in the marine environment come in different shapes and have random patterns. The wave's random pattern is a result of different waves that interfere with each other, which have been generated by earlier winds at other locations in the ocean. Consequently, wave fields are best characterized by means of a wave spectrum. The wave spectrum includes all wave frequencies and their respective amplitudes that can be found in the ocean. Furthermore, waves in the ocean have different shapes than in shallow water conditions. Waves in deep water conditions do not feel the bottom of the ocean, while shallow water waves are subject to friction induced by the bottom. Consequently, the orbital particle motion, which is influenced by the shape of the wave is different in both depth conditions. In Figure 2.6, an overview is given of the orbital motion for waves in different water depths. The identification of whether the waves are in deep or shallow water is based on the multiplication of the wavenumber k and the water depth d. When kd reaches an infinite value the wave conditions are considered to be in deep water, while kd goes to zero for shallow water waves.

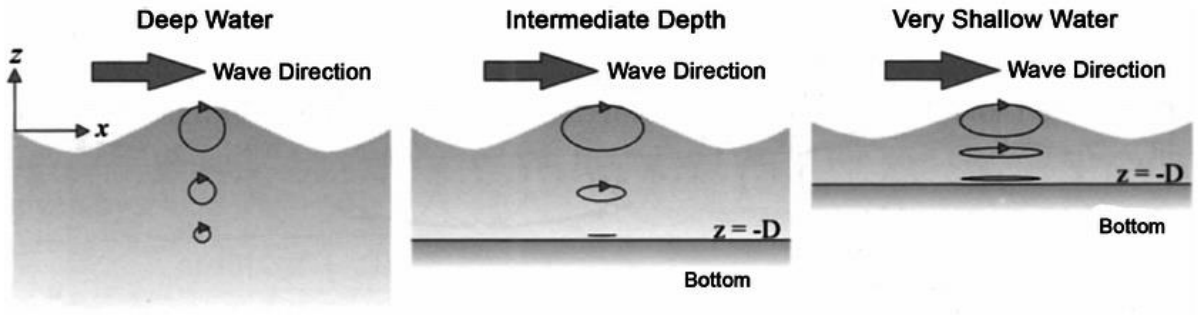

Figure 2.6 The orbital motion of water particles at different depths (Rafiuddin Ahmed, et al., 2010).

2.3.2 Tested wave conditions

The wave-breaking-induced transport is studied for deep water random seas. The conditions of the wave field in the experiment should be such that the waves are in deep water conditions and that the waves are unidirectional and irregular. First, the deep water requirement is discussed. For a wave to be considered in deep water, the wavelength should be smaller than 2 times the water depth. The

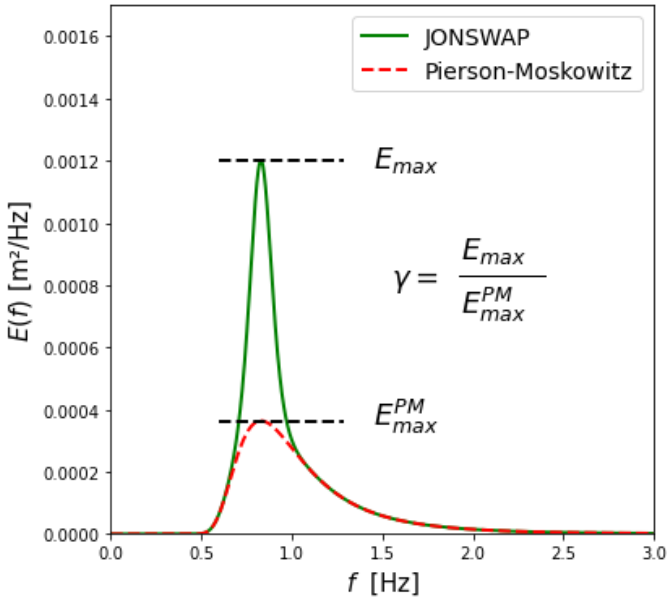

Figure 2.7 The Pierson-Moskowitz (PM) spectrum is represented by the red dashed lined and the JONSWAP spectrum by the green solid line. The peak enhancement factor γ is calculated by the ratio between the maxima of both spectra.

water depth in the Atlantic basin is fixed at 1 m. Thus, the maximum wavelength should be smaller than 2 m. The generation of waves in the facility is limited by the water depth, wave steepness, and acceleration of the wave paddle. Consequently, wavelengths smaller than 2 could not be generated. The maximum peak wave period that could be generated considering the limitations of the facility was 1.2 s, which corresponds to a wavelength of 2.2 m via the dispersion relation. This gives the closest value to deep water conditions that could be generated by the facility. The second requirement is the generation of irregular waves. These conditions are best described by means of the energy density spectrum for waves. The wave spectrum gives a complete statistical description of the surface elevation of the ocean waves and will be discussed in more detail in chapter 4. Results from many studies have shown that the JONSWAP spectrum is best at describing irregular wave conditions (Holthuijsen, 2007). Therefore, the energy density spectrum for all experiments is the JONSWAP spectrum $E_{JONSWAP}(f)$:

$$E_{JONSWAP}(f) = \alpha g^2 (2\pi)^{-4} f^{-5} \exp\left[-\frac{5}{4}\left(\frac{f}{f_p}\right)^{-4}\right] \gamma^{\exp\left[-\frac{1}{2}\left(\frac{f/f_p - 1}{\sigma}\right)^2\right]}$$

Pierson-Moskowitz shape

JONSWAP

with the frequency of the waves f, the gravitational acceleration g, the peak frequency f_p, spectral width σ_s = 0.07 for $f \leq f_p$ and σ_s = 0.09 for $f > f_p$, the Phillips parameter α, and the peak enhancement factor γ. Because the experiments were part of a large-scale experimental campaign, the JONSWAP spectrum was predefined by Deltares. The four (input) significant wave height conditions examined are H_s = 0.05, 0.09, 0.12, and 0.17 m. The significant wave height is the average of the highest third of the waves in the wave field. The Phillips parameter α is related to the significant wave height, and therefore the characteristic wave steepness $\epsilon_{ch} = k_0 H_s/2$, where k_0 is the dominant wave number. Increasing the Phillips parameter leads to more energy in the wave field by larger significant wave height conditions and thus steeper waves. Using OrcaFlex, which is a software package

for marine systems analysis, α can be defined for a specified H_s and T_p. The peak enhancement factor γ is related to the spectral bandwidth and therefore also to the wave steepness. The peak enhancement factor determines how much the peak of the Pierson-Moskowitz spectrum is increased. Hence, the peak enhancement factor is the ratio between the maximum value of the Pierson-Moskowitz spectrum and the maximum value of the desired JONSWAP spectrum (figure 2.7). The Pierson-Moskowitz spectrum is the assumed spectrum for fully developed conditions in deep water. Increasing γ leads to an increase in wave steepness. The phases of a discretised spectrum were chosen randomly in order to create an irregular wave times series. The duration of the experiments was set to 70 minutes for H_s = 0.05, 0.09 and 0.17 m and 30 minutes for H_s = 13 cm. The duration, phases, energy density spectrum, and the requirement for unidirectional waves were used as input for the forcing of the wavemakers. An overview of the tests conducted is given in Table 2.2.

Table 2.2 An overview of the experimental input parameters with the wave field characteristics; the significant wave height H_s, the peak period T_p, and the wave steepness ϵ_{ch}. The concentration of the particles in the test section is given in g/m².

Experiment number	$\boldsymbol{H_s}$ [cm]	$\boldsymbol{T_p}$ [s]	$\boldsymbol{\epsilon_{ch}}$	Duration [min]	Wave spectrum
1	5	1.2	0.056	70	JONSWAP
2	9	1.2	0.010	70	JONSWAP
3	13	1.2	0.145	30	JONSWAP
4	17	1.2	0.190	70	JONSWAP

3

Data processing

In this chapter, the trajectories of the particles are extracted from the video footage of the overhead camera. To do this, a computer vision and machine learning program in Python is used. Some implications arise from the tracking of the particles using the Python program. Therefore, the goal is to process the trajectories in order to remove these implications. To do this, first, the tracking process of the plastic particles is discussed. From the tracking process, the trajectories of the particles are obtained. These trajectories are distorted by the curvature of the lens and have their coordinate system in pixels. Therefore, secondly, the trajectories are undistorted and translated to a coordinate system in millimetres. Lastly, two requirements are imposed on the trajectories to remove any remaining implications and errors.

3.1 Tracking the particles

The displacement of the particles is determined from images of a downward-looking camera. The images show a top view of the Atlantic Basin with yellow plastic particles randomly distributed floating on the surface of a wave field (Figure 3.1a). The particles are identified and tracked using OpenCV. OpenCV is a state-of-the-art computer vision and machine learning open-source library, which operates in the programming language Python. The particles are identified using a HUE saturation value model. Using this model, an optimal range in the HUE colour space is specified for which only the yellow colour of the particles is visible to the computer (Figure 3.1b). To obtain the trajectories of all individual particles the OpenCV library offers a total of 7 trackers. Their performance was analysed in Appendix A. From the trackers, the Discriminative Correlation Filter with Channel and Spatial Reliability (CSRT) tracker performed best regarding the accuracy, precision, and number of objects capable of tracking. The CSRT tracker is assigned to all the individual particles in the frame. This is done

(a) *(b)*

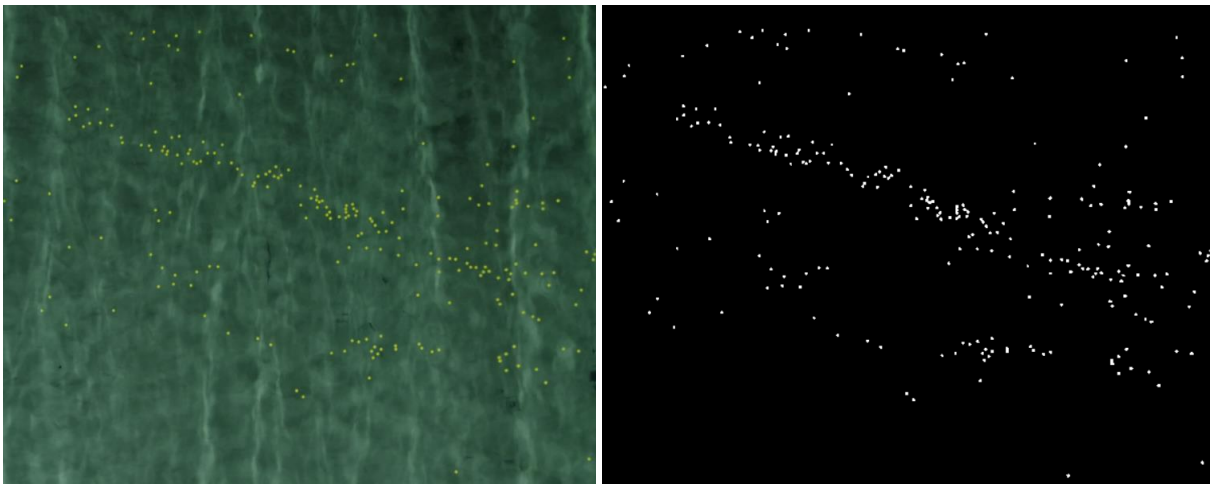

Figure 3.1 (a) Footage of the Atlantic Basin from the downward-looking camera. The small yellow spheres can be seen floating in the wave field. (b) Identification of the spheres after application of the HUE saturation value model in OpenCV.

by selecting a bounding box around the particles. The bounding box identifies the selected object based on its shape and colour. Reliability weights are given to the pixels indicating the location of the object. Consequently, over multiple frames, the tracker learns to reduce the background noise using the reliability weights resulting in better performance of the tracker. Additionally, the speed and the direction of the object's movement in the bounding box are tracked, which allows for the prediction of the new position of the object. Particles coming into the frame are not automatically assigned a CSRT tracker. CSRT trackers are only assigned to particles in the first frame. To get approximately the same duration for all trajectories in an experiment, only the particles located at the right half of the first frame are selected and the tracking process is stopped when the first tracker leaves the frame. To obtain a large number of tracked particles, the videos of the experiments were divided into smaller videos. The duration of the smaller videos was such that the same particle was not tracked twice. The trajectories of the particles are automatically saved in the (u, v) coordinates system of the pixel space from the camera.

3.2 Undistorting and translating the particle trajectories

The trajectories obtained from the CSRT tracker are distorted due to the curvature of the lens and have their coordinate system in pixels. In this section, the trajectories are undistorted and the coordinate system is transformed from pixels to millimetres. First, the method for undistorting the trajectories is discussed. To do this, the camera matrix and distortion coefficients are used. The camera matrix describes the projection of 3D points in the world to 2D points in the image. The camera matrix is composed of the camera intrinsics, which are governed by the focal length and resolution of the camera. The distortion coefficients correct the camera matrix such that the image becomes undistorted. To obtain the camera intrinsics and distortion coefficients, video footage of the calibration board floating on the surface of the Atlantic basin was analysed. The pixel space of the calibration board was related to its real-world sizes in millimetres. The calibration board consist of a grid of 75x75 mm squares, which was moved over the surface of the Atlantic Basin until the whole field-of-view of the camera was covered. This was necessary to correctly undistort the whole image. Subsequently, the corners of the squares from the calibration board were identified and matched with their pixel coordinates using cv.findChessboardCorners from OpenCV (Figure 3.2a). Hence, for multiple images, the distances in millimetres and pixels are related at different locations by analysing the calibration board in the camera's field-of-view. The coordinates of the corners of the calibration board in millimetres and in pixels were taken as input arguments for the OpenCV function cv.calibrateCamera, which returned the camera matrix, rotation matrix, translation vectors, and distortion coefficients. The trajectories are then undistorted with the function cv.undistort using the camera matrix and the distortion coefficients. Secondly, the coordinate system of the trajectories in the pixel space is transformed into millimetres. To do this, a single image of the calibration board for which the coordinate of the top left square is known in the coordinate system of the Atlantic basin is used (Figure 3.2b). This image is undistorted using cv.undistort with the previously discussed camera matrix and distortion coefficients. Subsequently, from the undistorted image, the camera matrix, rotation matrix, and translation vectors are calculated. The real-world coordinates are then calculated with the camera's intrinsic and extrinsic parameters based on a pin-hole camera:

$$s\begin{bmatrix} u \\ v \\ 1 \end{bmatrix} = \underbrace{\begin{bmatrix} f_x & 0 & c_x \\ 0 & f_y & c_y \\ 0 & 0 & 1 \end{bmatrix}}_{\text{Intrinsic parameters}} \underbrace{\left[\begin{array}{ccc|c} r_{11} & r_{12} & r_{13} & t_1 \\ r_{21} & r_{22} & r_{23} & t_2 \\ r_{31} & r_{32} & r_{33} & t_3 \end{array}\right]}_{\text{Extrinsic parameters}} \begin{bmatrix} X \\ Y \\ Z \\ 1 \end{bmatrix} \tag{3.1}$$

(a) *(b)*

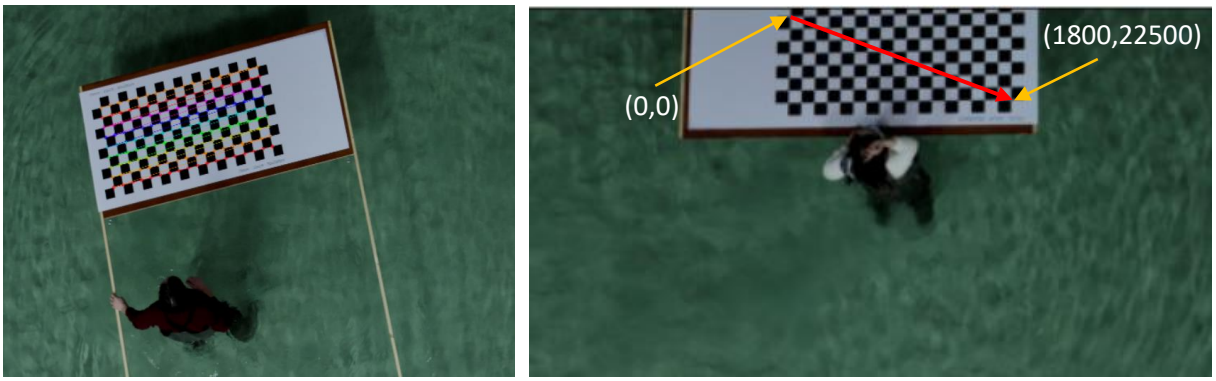

Figure 3.2 (a) the identified calibration board from its corners and (b) the image which is undistorted and translated to the tank coordinates system

with on the left-hand side the scaling factor s and the coordinates (u, v) of the projection point in pixels. The first matrix on the right-hand side is the part of the camera matrix containing the intrinsic parameters f_x and f_y, which are the focal lengths expressed in pixel units and (c_x, c_y), which is a principal point that is the image center. The second matrix on the right-hand side is an augmented matrix consisting of the rotation matrix and the translation vector. Lastly, (X, Y, Z) are the coordinates of 3D points in the world coordinate space. In this research, the calibration board remains on the surface of the basin and therefore Z in the real word coordinates system is set to zero.

Summarizing, the u and v coordinates of the trajectories are undistorted with the camera matrix and distortion coefficients obtained from the first calibration and thereafter, transformed to the real word points using the camera intrinsic and extrinsic parameters from the second calibration of the undistorted image and (3.1). The coordinate system of the undistorted and transformed particle is then translated to the coordinate system in the basin by modifying the location from the top left corner, of the calibration, which is set by the Python function as the first corner and thus (0,0), to the right bottom corner where the known location is in the Atlantic basin coordinate system namely, (1800,22500) (Figure 3.2b). After translating the (0,0) to the right bottom corner, 1800 is added to the X coordinate, and 22500 is added to the Y coordinate for all points.

3.3 Post processing the particle trajectories

The trackers and trajectories are inspected manually and limitations are perceived concerning the CSRT tracker. In this section, two major limitations are evaluated and solutions are proposed. The first limitation concerns the colour of the particle. As discussed in section 3.1 the tracker identified the particle based on its shape and colour. During wave-breaking events, the particles become slightly submerged resulting in particles appearing a different colour. Additionally, due to the generation of bubbles in the wave-breaking front, the background becomes lighter in colour. Hence, the colour of the particle and its surroundings change. Whereupon the tracker is not able to recognize the sphere. Consequently, the tracker loses the particle and remains still at the last position where the particle is identified or directly moves to the top-left corner of the image where it remains still. The second limitation follows from the distribution of the particles in the field-of-view of the camera. A large concentration of particles tends to accumulate resulting in collisions. During these collisions, trackers overlap and multiple particles are present in a single tracking region. As a result, trackers sporadically jump from the particle they are tracking to the particle it collides with. Consequently, multiple trackers track a single particle and the other particles are not tracked anymore. The limitations are schematized in Figure 3.3.

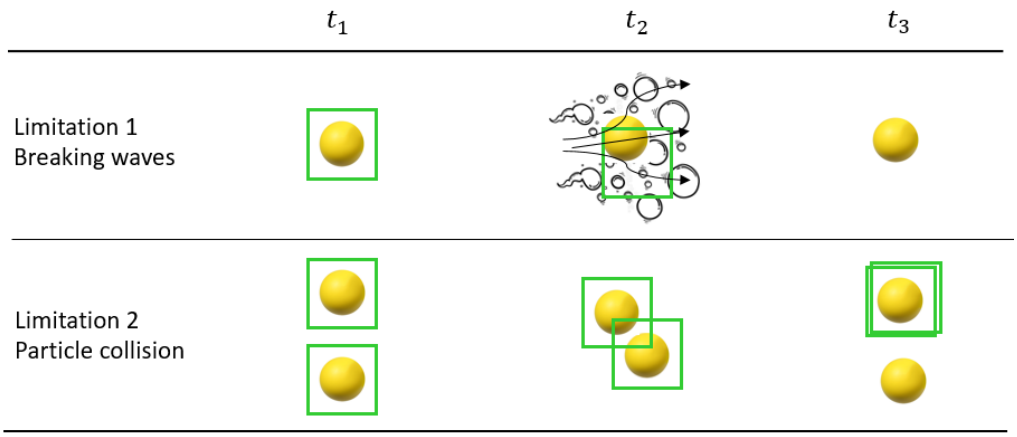

Figure 3.3 Schematization of the limitations of the CSRT tracker. The green box indicated the region of interest of the tracker in which the particle is identified.

These limitations are solved in post-processing. This is done by recognizing the error in the trajectories of the particles. For the first limitation. the tracker remained still or moved to the top-left corner of the image. Hence, if a particle remained motionless for 40 consecutive frames then the trajectory is removed from the first frame the object remained still. Additionally, when the coordinates of the trajectory are located in the top corner and remain still for 20 consecutive frames their trajectory is removed. For the second limitation when the trackers are tracking the same particle due to a collision, the trajectory of one of the trackers is removed. To do this, first, the trackers which are tracking the same particle are identified based on their coordinates. If the coordinates of both trackers are the same, for 20 consecutive frames, a collision is identified. Subsequently, the tracker that jumped to the other particle is removed. The identification of this tracker is based on the distance travelled during the occurrence of the collision. Because the tracker jumps to another particle its travelled distance is larger than for the other particle. Hence, the tracker with the largest travelled distance during the collapse is removed. After post-processing the data, the trajectories are obtained for individual particles in the coordinates system of the Atlantic Basin.

4

Analysis of the experimental data

This chapter aims to obtain the wave-breaking-induced transport from the trajectories of the particles, which were processed in chapter 3. This is achieved by analysing the hydrodynamics in the tank and identifying the breaking waves in the trajectories of the particles. First, the hydrodynamics in the tank are studied. This is done using the data from the wave gauges and the electromagnetic velocity meters (EMS). From the wave gauge data, the surface elevation time series is obtained and the wave field is characterized using a spectral analysis. Additionally, the surface elevation spectrum is used to estimate the number of breaking waves in the wave field. From the EMS data, the influence the Eulerian current on surface transport is quantified. Subsequently, the trajectories of the particles are analysed. The particle trajectories are studied by distinguishing between breaking and non-breaking waves using a velocity threshold. The velocity threshold is adjusted for each experiment based on the analysed hydrodynamics in the tank. The experimentally and theoretically estimated hydrodynamics are compared to see whether they are in agreement. Lastly, the quantified wave-breaking-induced transport is used to calculate the enhancement factor, which calculates the enhancement of the Stokes-induced transport by the wave-breaking-induced transport in a wave field.

4.1 Analysis of wave gauge data

In this section, the characteristics of the wave fields from the experiments are assessed using a spectral analysis. The spectral analysis discusses the distribution of wave height with respect to the frequency of the measured irregular waves. The spectral analysis gives an understanding of the wave-induced surface transport for non-breaking waves in the Atlantic basin through the energy spectrum. Consequently, the Stokes drift and the number of breaking waves are calculated from the wave gauge data. This is done based on a literature study into the hydrodynamics of the waves.

4.1.1 Spectral Analysis

The time series of the surface elevation $\eta(t)$ from the experiment gives a first insight into the wave characteristics and the distribution of energy over different wave frequencies. The surface elevation is 1-dimensional in time and measured at a fixed location. The wave characteristics analysed in this paragraph are the input period T and the significant wave height H_s. To obtain these characteristics, the random phase/amplitude model is used, which is discussed in paragraph 1.1.1. This is the basic model to describe the moving surface elevation $\eta(t)$ in deep water conditions. In this model, the surface elevation is assumed to be composed of the sum of a large number of independent stationary harmonic components (i.e. a Fourier series), each with a constant amplitude a_i, phase α_i, and frequency f_i. The amplitude a_i and phase α_i for each harmonic component are determined by applying a Fourier transform to the surface elevation data. The Fourier transform decomposes the surface elevation into harmonic components with an amplitude and phase for each frequency. Summing those components up gives the surface elevation $\eta(t)$. The amplitude of each frequency is used to compute the variance $0.5a_i^2$. The variance is a more relevant quantity than the amplitude as it is proportional to the energy of the waves. For each frequency, the variance is estimated and a

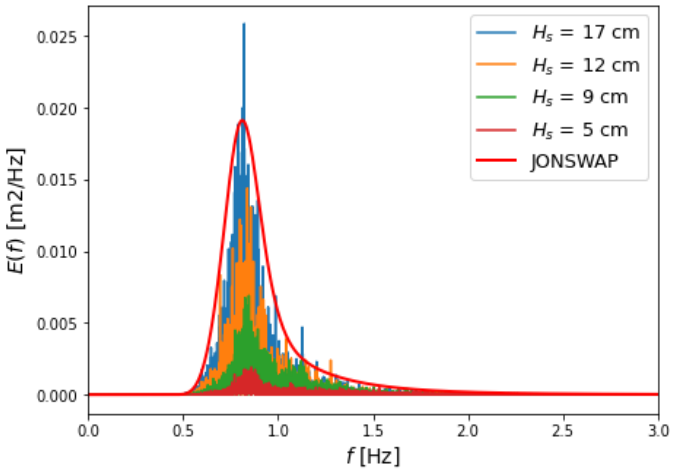

Figure 4.1 The variance density spectra for different input significant wave heights H_s. The JONSWAP spectrum is plotted in red and represents the shapes of the input spectra to generate irregular wave conditions.

variance density spectrum is generated. The energy spectrum is acquired by multiplying the variance of the surface elevation $E(f)$ by the density of water ρ and the gravitational constant g. Figure 4.1 shows the variance spectra for all input significant wave height cases H_s. The surface elevation time series used to create the spectra are measured at wave gauge 3. Wave gauge 3 is located closest to the region of interest at 21.4 m from the wave paddle. The input time series of the spectra are not binned and comprise about 443000 discrete frequencies. All spectra follow the same JONSWAP shape corresponding to the irregular sea state steered by the wave maker. The peak frequency $f_{p,exp}$ of the variance density spectra in Figure 4.1 is approximately 0.82 Hz. The peak frequency is inversely proportional to the peak period $T_p = 1/f_p$ and agrees thereby well with the input period of 1.2 s.

The significant wave height is statistically analysed from the experimental results. It is calculated from the variance density spectrum $E(f)$ and compared to the input values of H_s. To rewrite the significant wave height in terms of spectral characteristics, the random sea surface elevation is assumed to be a stationary, Gaussian process. Additionally, the spectrum is assumed to be narrow and the analytical expression from Rice (1944) is used, where he related the wave statistics to the spectrum. Consequently, it is assumed that the probability density function of the crest height $p_{\eta_{crest}}(\eta)$ follows a Rayleigh distribution and can be written in terms of the zeroth-order moment m_0 of the variance density spectrum $E(f)$:

$$p_{\eta_{crest}}(\eta) = \frac{\eta}{m_0} \exp\left(-\frac{\eta^2}{2m_0}\right), \tag{4.1}$$

although the spectrum in this research is wide, observations have shown that this method also gives good results for the estimation of the significant wave height from broader spectra. The moments in (4.3) are statistical characteristics of the variance density spectrum and are determined by $m_n = \int_0^\infty f^n E(f) df$, where n is the order. Here only the zeroth-order moment is used, which is equal to the total variance of the surface elevation. The wave height H is approximately equal to two times the crest height $H \approx 2\eta_{crest}$. Therefore, the probability density function of the wave height $p(H)$ also follows a Rayleigh distribution:

$$p(H) = \frac{H}{4m_0} \exp\left(-\frac{H^2}{8m_0}\right), \tag{4.2}$$

The significant wave height is defined as the mean value of the highest third of this Rayleigh distribution $\int_{H^*}^{\infty} p(H)dH = \frac{1}{3}$, where H^* is the minimum value for which the area is the highest third. The mean of the area of the highest third can be rewritten as an expected value using the zeroth-order moment m_0 and first-order moment m_1 of $p(H)$. The first-order moment divided by the zeroth-order moment gives the mean. Hence, the significant wave height is given by:

$$H_{m_0} = \frac{\int_{H^*}^{\infty} Hp(H)dH}{\int_{H^*}^{\infty} p(H)dH} \ , \tag{4.3}$$

Substituting (4.2) into (4.3) gives the spectral significant wave height H_{m_0} in deep water:

$$H_{m_0} \approx 4\sqrt{m_0} \ , \tag{4.4}$$

The result of the spectral significant wave height and peak period from the spectral analysis are presented in Table 4.1. The spectral significant wave height H_{m_0} is underestimating for the input significant wave height cases $H_s = 13$ and 17 cm. The reason for this is the number of breaking waves, which increases for larger H_s. This enhanced breaking for larger H_s results from an increase in steepness, which will be discussed in paragraph 4.1.3. The breaking waves dissipate energy and as a result, the wave height decreases.

Table 4.1 The input significant wave height H_s together with the obtained spectral significant wave height H_{m_0} and peak period T_p from the variance density spectrum.

H_s [cm]	H_{m_0} [cm]	T_p [s]
5	5.32	1.16
9	8.92	1.18
13	12.12	1.19
17	13.60	1.22

4.1.2 Stokes drift estimation

Non-breaking surface gravity waves induce a net drift in their propagation direction known as the Stokes drift (Stokes, 1847). In the Atlantic basin, the Stokes drift contributes to the transport of the upper layers together with the Eulerian current. However, calculating the Stokes drift in experiments is challenging (Monismith, 2020). The main challenge is caused by the finite length of the basin forcing the condition of no net flow. Consequently, when the mass of the wave-induced transport meets the no-flow boundary imposed by the beach it drives an opposite return flux, often in the form of an undertow, which influences to the transport at the surface (Swan, 1990). Additionally, during the laboratory experiments, the mean Eulerian flow changes as the effects of the sidewall, surface, and bottom boundary layers begin to influence the flow in the interior of the tank (Longuet-Higgins, 1953). Moreover, to which extent the waves are absorbed by the beach at end of the tank also influences the return flow in the interior of the tank. Sub-harmonic waves are reflected back toward to wave paddle and affect the surface transport (Calvert, et al., 2019). However, Calvert et al. (2019) note that in deep-water experiments, sub-harmonic error waves are found to have a negligible effect, while it is a considerable effort to mitigate them.

Furthermore, the spectral analysis in section 4.1.1 can give an understanding of the wave-induced surface transport for non-breaking waves in the Atlantic basin through the energy spectrum. Kenyon (1969) used the energy spectrum to calculate the average Stokes drift of a wave field. Therefore, the Stokes drift for irregular waves with a broad-banded spectrum in deep-water is estimated using the formulation by Kenyon (1969). In his paper, the Stokes drift was calculated in terms of the directional

energy spectrum. As discussed in the previous paragraph this spectrum is created from the surface elevation $\eta(t)$ and its corresponding Fourier components. These components can be seen as individual waves for which the Stokes drift $\bar{u}_s$ at the surface (z = 0) can be calculated using the formulation of Stokes (1847) for deep water unidirectional monochromatic waves:

$$\bar{u}_{st} = \omega k a^2 \ , \tag{4.5}$$

where ω is the wave frequency, k is the wave number, and a is the amplitude. The Stokes drift can be rewritten in terms of the wave period T and the phase speed $c = gT/2\pi$ using the dispersion relation in deep water conditions $\omega = \sqrt{gk}$, where $k = 2\pi/L$ and $\omega = 2\pi/T$:

$$\bar{u}_{st} = \frac{(2\pi)^3}{gT^3} a^2 = (ak)^2 c \ , \tag{4.6}$$

where g is the gravitational constant and L the wave length. The dispersion relation originates from linear wave theory, which gives a linearized description of the propagation of gravity waves on the surface of a homogeneous fluid layer from which local wave characteristics can be computed (Holthuijsen, 2007). The Stokes drift appears to positively scale with the phase speed of the wave and quadratic with the wave steepness ak.

Kenyon (1969) relates the Stokes drift to the energy spectrum by taking the variance $0.5a_i^2$ of the harmonic components from the surface elevation $\eta(t)$ and multiplies it by the density of the water ρ, and the gravitational acceleration g to create a two-dimensional energy spectrum $\iint_0^\infty F(\boldsymbol{k})d\boldsymbol{k}$, where $F(\boldsymbol{k})$ is the directional wave spectrum and $\boldsymbol{k}$ is the wave number vector. However, in this research, the wave direction is unidirectional. Therefore, the energy spectrum is simplified to a one-dimensional spectrum $f(\omega)$ by setting the integral of the directional spreading to 1. The total energy of a one-dimensional spectrum equals the summation over all harmonic components:

$$E_{total} = \rho g \eta^2 = \int_0^\infty f(\omega) d\omega \ , \tag{4.7}$$

where η^2 is the total variance the surface elevation. The mean second-order drift velocity of the wave field is then derived by applying the formulation of Stokes (1847) for individual waves, which involves the superposition of the average motion in the wave direction for each wave component. Resulting in the formulation for the mean Stokes drift velocity $u_{st,\eta}(z)$ for a one-dimensional energy spectrum and for arbitrary depth by Kenyon, where the subscript η indicates that the Stokes drift is calculated from the surface elevation time series of the experiment:

$$u_{st,\eta}(z) = \frac{2}{\rho g^2} \int_0^\infty f(\omega) \omega^3 e^{2\omega^2 z/g} d\omega \ , \qquad for -\infty \leq z \leq 0 \tag{4.8}$$

(8) calculates the Stokes drift over the whole depth. However, in this research, only the surface drift is relevant. Therefore, the exponential term considering the depth component is not taken into account (i.e. z = 0). The approximation of the Stokes drift at the surface of deep-water irregular waves $u_{st,\eta}$ simplifies to:

$$u_{st,\eta} = \frac{2}{\rho g^2} \int_0^\infty f(\omega) \omega^3 d\omega \ , \tag{4.9}$$

This formulation for the Stokes drift appeared to over-estimates the observed drift in the experiments. The spectral tail contributes significantly to the Stokes drift. The Stokes drift defined here is calculated for Lagrangian tracers, which follow the water particles perfectly. However, the particles in the experiment are not Lagrangian tracers for all frequencies.

Based on Calvert et al. (2021) we assume that the particles are Lagrangian tracers when the object diameter is smaller than 10% of the wavelength. The particles have a maximum diameter of 20 mm. Hence, the maximum wavelength for which the particles are considered Lagrangian tracers is 20/0.1 = 200 mm. Using the maximum wavelength L_{lagr} and the dispersion relation $2\pi f_{lagr} = \sqrt{gk}$, where $k = 2\pi/L_{lagr}$, the corresponding frequency is calculated. The contribution of the frequencies above the maximum frequency for Lagrangian tracers f_{lagr} is negligible to the Stokes drift and the higher frequencies are therefore removed from the spectrum. A cut-off frequency of 2.8 Hz is found, which is equal to $\omega = 5.6\pi$ rad/s and $3.5f_0$, where f_0 is the peak frequency (≈ 0.82 Hz). To estimate the Stokes drift from the surface elevation spectrum, we truncate the spectrum to $f < 3.5f_0$ taking only the frequencies below $3.5f_0$.

$$u_{st,\eta,f<3.5f_0} = \frac{2}{\rho g^2}\int_0^{5.6\pi} f(\omega)\omega^3 d\omega\,, \tag{4.10}$$

Table 4.2 confirms once more the influence of the tail of the spectrum. The wave gauges which were used for the experiment with the input significant wave height H_s of 13 cm had a frequency sampling $f_{sampling}$ of 64 Hz compared to the 256 Hz of the other H_s cases. Therefore, the tail of the H_s = 13 cm is 4 times shorter. The highest possible frequency is equal to the Nyquist ($0.5f_{sampling}$), which can be described by the smallest possible wave the wave gauge can measure. However, according the formulation by Stokes (1847), the Stokes drift should increase with the wave steepness, but this is not the case for the H_s = 13 cm compared to the H_s = 9 cm experiment, because the contributions in the tail are significant. This problem is solved with the Stokes drift in the truncated spectrum $u_{st,\eta,f<3.5f_0}$ where the tail is the same for all experiments.

Table 4.2 The input significant wave height H_s together with the Kenyon Stokes drift apporiximation $u_{st,\eta}$ and the Stokes drift approximation with a cut-off frequency at $u_{st,\eta,f<3.5f_0}$.

H_s [cm]	$u_{st,\eta}$ [mm/s]	$u_{st,\eta,f<3.5f_0}$ [mm/s]
5	49.06	13.47
9	62.02	28.29
13	48.99	43.78
17	100.32	50.75

4.1.3 Wave breaking percentage

Deep-water waves break when their steepness exceeds a threshold (Chen & Zou, 2022). The geometry of the breaking waves is well defined by the wave amplitude $a = H/2$ and the wave length L. The wave steepness ϵ is related to these parameters:

$$\epsilon = kH/2\,, \tag{4.11}$$

where $k = 2\pi/L$ is the wavenumber. To identify the waves in the wave spectrum $\eta(t)$ a zero-up crossing analyses is applied. From the waves, the wave height H is defined by the difference between the highest point in the crest to the lowest point in the trough and the wave period T is defined as the

time between two up-crossings of the surface elevation relative to the mean water level. Using the dispersion relation the wave number k is calculated from the wave period T.

When ϵ increases the wave becomes more non-linear. The geometry of a non-linear wave is described by a steeper wave-crest and a flatter wave-through compared to a linear wave. When ϵ nears the breaking threshold for the steepness, the wave displays asymmetry as the front face steepens further after which a limit is reached and wave breaking occurs. According to Stokes' (1880) this limiting value of ϵ is 0.443 when the crest angle becomes 120°. Experimental observations have shown that the limiting steepness is commonly smaller than the breaking limit from Stokes. Duncan (1981) produced steady spilling breakers by towing a submerged, two-dimensional hydrofoil at constant depth and speed finding a limiting steepness of 0.31. The breaking-wave steepness varies over a large range. Tulin & Waseda (1999) studied the nonlinear evolution of wave groups, which were initiated by unstable three-wave systems and found that the steepness is in the range of 0.22 to 0.41. In experiments conducted by Tian et al (2012), the steepness of some spillers was considerably higher than that of some plungers. In conclusion, the breaking-wave steepness is rather arbitrary. Other characteristics are also known to have a significant influence on the breaking onset such as three-dimensional effects and wave directionality. As most breaking events during this experiment were spilling breakers the criterion by Duncan (1981) is used. However, another factor that strongly affects breaking is the presence of currents.

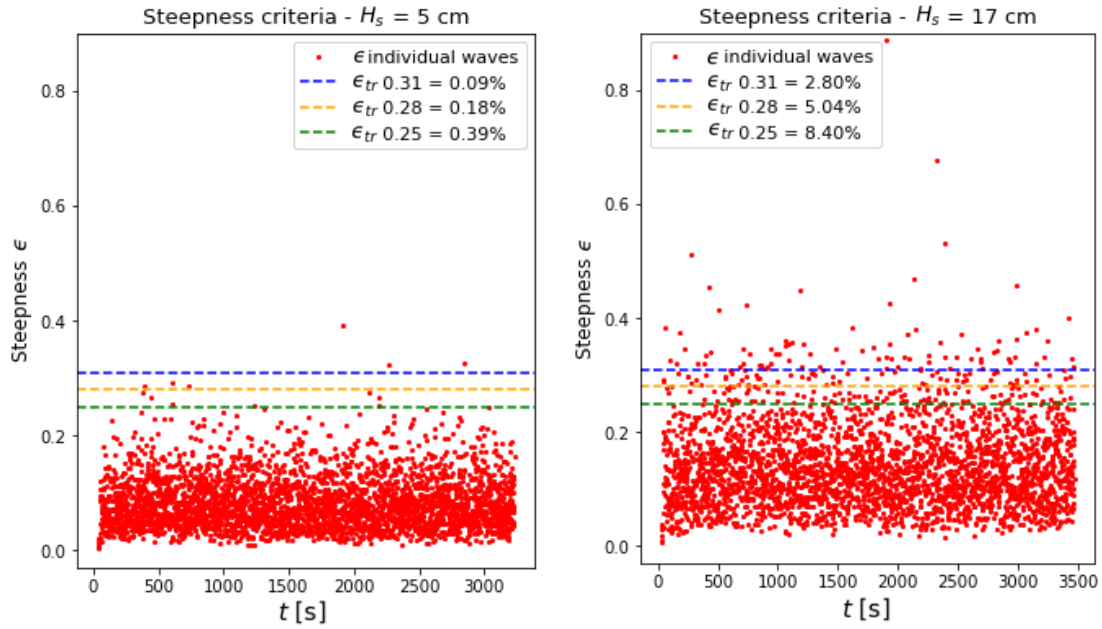

Figure 4.2 The red dots represent the steepness ϵ of individual waves. When the steepness of a wave is above the one of the dashed threshold lines ϵ_{tr} , the waves is identified as a breaking wave. The wave field with larger significant wave height H_s = 17 cm has steeper waves than the wave field with H_s = 5 cm and hence more breaking events.

In this research, an opposing current was generated, which contributes to more unstable waves (Eliasson & Haas, 2014). Therefore, for a first estimation, the steepness threshold for breaking ϵ_{tr} is lowered to a value of 0.28. To analyse the sensitivity of this threshold the percentage of breaking is calculated for ϵ_{tr}= 0.31, 0.28, and 0.25 in H_s = 5 cm and H_s = 17 cm. For the H_s = 5 cm experiments almost no breaking events were observed and for H_s = 17 cm breaking was almost continuously observed. Figure 4.2 shows the number of breaking waves for all steepness thresholds ϵ_{tr} in H_s = 17 and 5 cm. The waves with steepness ϵ exceeding the breaking threshold ϵ_{tr} are identified as breaking waves. Table 4.3 shows the breaking percentages for all threshold values per input significant wave height conditions H_s. The percentages for ϵ_{tr} = 0.31 in H_s = 17 cm are much lower than the observed

number of breaking waves. This confirms that this steepness threshold is too high. The percentages of ϵ_{tr} = 0.28 and 0.25 are more realistic with the observations. Therefore, we expect the breaking percentage for the different significant wave heights to be in these ranges.

Table 4.3 An overview of percentages of breaking waves for different breaking thresholds ϵ_{tr} in the input significant wave height conditions H_s

H_s [cm]	ϵ_{tr} = 0.25 [%]	ϵ_{tr} = 0.28 [%]	ϵ_{tr} = 0.31 [%]
5	0.39	0.18	0.09
9	1.92	0.57	0.21
13	5.59	3.10	1.58
17	8.40	5.04	2.80

4.2 Current analysis from EMS data

In the direction of the waves, the vertical velocity profile near the surface is predominantly influenced by the Stokes drift, breaking waves. In the opposing direction, the Eulerian current is of importance. This Eulerian current is a result of the pump-induced flow, which maintains a constant water level in the basin, and from the return flux induced by the mass of the wave-induced transport meeting the no-flow boundary at the end of the basin. The velocity measurements over the vertical are available from the EMS data. The EMS data indicates the velocity profile for different significant wave heights H_s at a depth of approximately 0.2, 0.3, and 0.5 m below the mean water level. The EMS sensors are located in the centre of the tank at 14.3 m from the wave paddle. Figure 4.3a shows the results of the EMS data in H_s = 5, 9, and 17 cm. A strong negative current (opposing the waves) is observed at 0.2 m below the mean surface elevation, which is a result of the induced current generated by a constant discharge from the pump and the return flux from the waves. To compensate for this current a flow with a maximum around of 0.3 m below the mean surface elevation is present. Further down the water column (i.e. near the bottom), the velocity profile becomes negative again as a result of the return flux from the waves. Moreover, we see that the current at 0.2 m below the surface shows a strong increase in the opposing wave direction for larger significant wave height input conditions H_s. When waves oppose the current, an increase in the current intensity is achieved near the mean water level. Therefore, the mass transport in the upper part of the water column is reduced. In most nonlin-

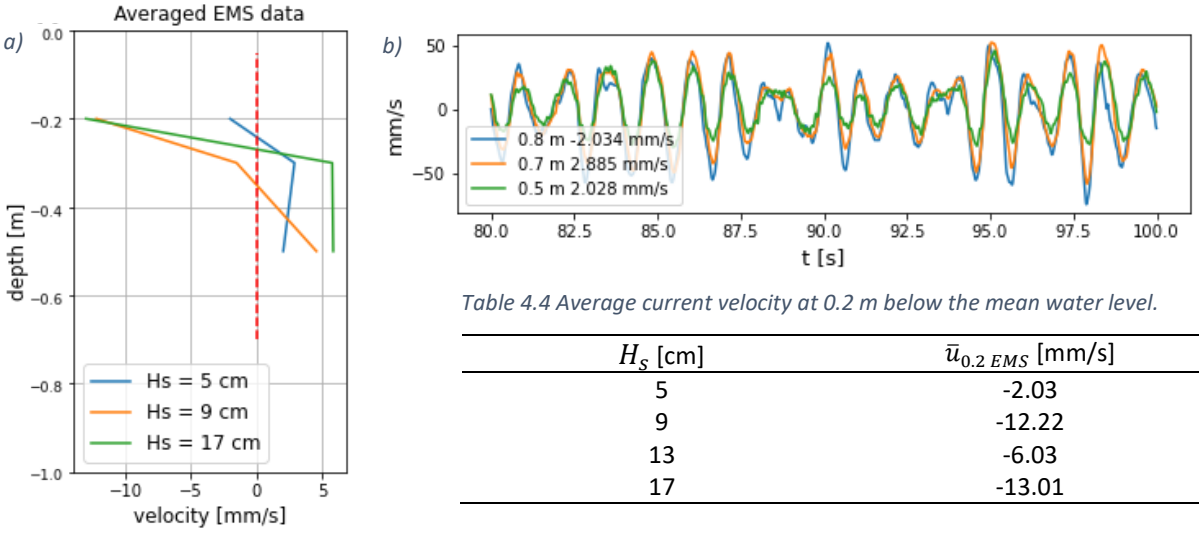

Table 4.4 Average current velocity at 0.2 m below the mean water level.

H_s [cm]	$\bar{u}_{0.2\ EMS}$ [mm/s]
5	-2.03
9	-12.22
13	-6.03
17	-13.01

Figure 4.3 (a) Averaged velocities over the vertical, where the mean water level is at depth 0.0. Negative values indicate the current flowing opposing the wave propagation direction (b) Wave-induced transport is clearly visible in the EMS data.

ear opposing cases, these superficial currents can show negative velocities. This effect is counteracted in the middle part of the water column by an increase in the current intensity (Olabarrieta, Medina, & Castanedo, 2010). Unfortunately, it is not possible to take EMS measurements at the surface and the influence of this opposing current on the transport on the surface is not yet completely understood. Besides, extrapolating the EMS data from 0.2 m below the surface to the mean water level gives unrealistically high return flows. Hence, we assume that the measured current at 0.2 m below the surface directly influences the drift at the surface. The EMS data at 0.2 m below the surface (i.e. 0.8 m above the bed) is averaged over the total duration of the experiment. In this way, the averaged current at 0.2 m below the mean water level $\bar{u}_{0.2\,EMS}$ is obtained. The average Eulerian current velocities for each experiment are presented in Table 4.4.

Furthermore, experiments in the Atlantic basin have been conducted without waves but solely with the pump-induced current. However, for those experiments, only video footage was available but no EMS data. The experiment consisted of 86 particles. The particles appeared to be floating back to the wave paddle confirming the opposing pump-induced flow. Additionally, the results showed that the particles near the side of the tank have lower velocities than those in the middle of the basin.

4.3 Particle trajectory analysis

In this section, I will explain how the wave-breaking-induced transport is obtained from the trajectories of the particles. First, the displacement of the particles is discussed by identifying breaking and non-breaking waves. Hereafter, a breaking threshold is defined using the analysis of the hydrodynamics in the tank and the characteristics of breaking waves from the previous paragraphs.

4.3.1 Displacement of particles in breaking and non-breaking case

The trajectory or drift of the particles is a result of multiple hydrodynamic processes occurring simultaneously in the Atlantic basin during the experiment. Non-breaking waves induce a net averaged forward motion on the particles known as the Stokes drift. For breaking waves, the transport of particles is much faster than for non-breaking waves. Particles may surf on the waves due to wave breaking and be subject to transport faster than the Stokes drift (Pizzo et al. 2019; Lenain & Pizzo 2020b). Meanwhile, to maintain a constant water level, an opposing current was generated by the pump located at the end of the basin. Besides, large vortices were created by researchers walking circular patterns in the tank during the removal of the spheres. In the worst cases, these vortices were so large that the waves were no longer unidirectional and the experiment had to be stopped. These components of the trajectories are analysed using a literature study and measurements to make an accurate estimation of the wave-induced drift in breaking waves. In summary, the motion of the trajectories is composed of:

$$Object\ Drift = Stokes + Breaking + Current\ , \tag{4.12}$$

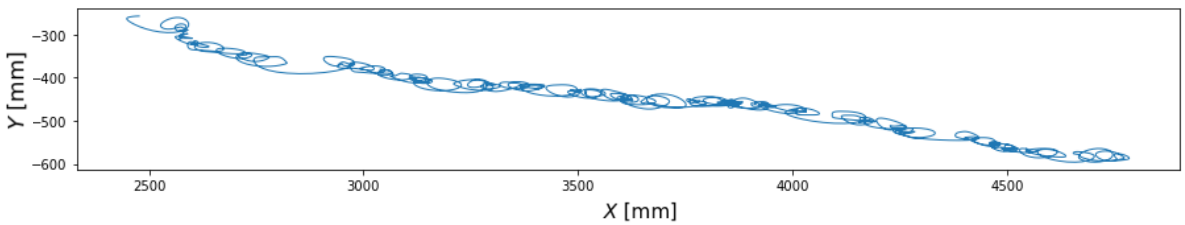

Figure 4.4 The top view of a single particle travelling from right to left through the area of interest. The axis in this image are scaled. At X_i = 3000 mm to X_i = 2700 mm a breaking event is observed.

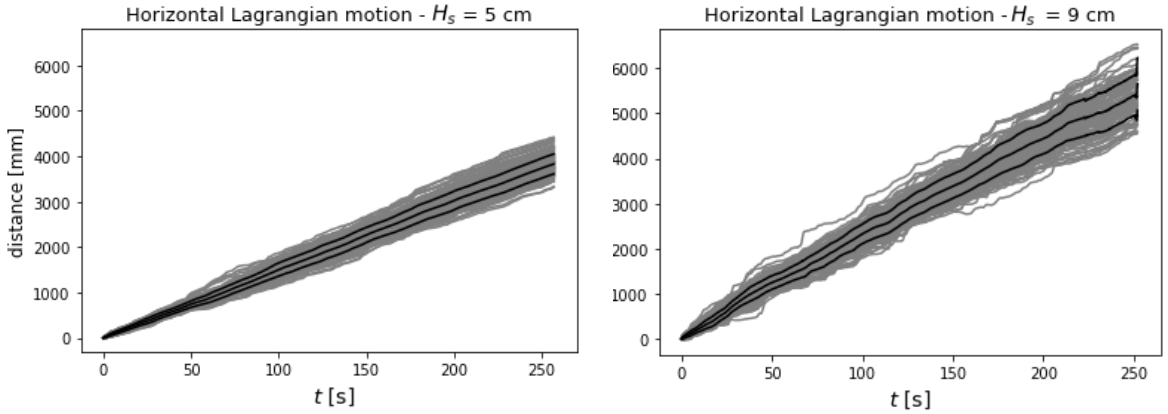

Figure 4.5 The cumulative horizontal motion of the particles over time for H_s = 5 cm on the left and H_s = 9 cm on the right. Within the same time span more distance is travelled by the particles in H_s = 9 cm compared to H_s = 5 cm.

Figure 4.4 shows a top view of the total displacement of a single particle at the surface $\{X_i(t), Y_i(t)\}$ over time t. The trajectory of the particle in non-breaking waves show similar behaviour in the form of small circular motions corresponding to the periodic motion of the waves. This circular motion of the particles is a result of the fluid moving with the wave at the crest and opposing the wave at the through. In most breaking waves, the particles experience a significant horizontal jump, which can be observed at X_i = 3000 mm to X_i = 2700 mm. Therefore, the net drift in the horizontal direction for a breaking wave is larger than for non-breaking waves. However, the horizontal drift depends heavily on the location of the particle during breaking waves. Close to the breaking point the particles experience a large displacement, which can be an order of magnitude larger than for non-breaking waves or for particles further downstream from the breaking point. The particles located more downstream show a subtle increase in distance and acceleration and may still have a significant contribution to the object's drift (Brown, et al., 2019).

Figure 4.5, shows the horizontal displacement in time for all individual particles in the significant wave height conditions H_s = 5 cm and 9 cm. For each individual particle, the total horizontal displacement $\sum x(t)$ is averaged by the total duration tend the particle is being tracked, yielding the object's average drift $\langle \bar{u}_{ob} \rangle$. The average object drift per significant wave height $\langle \bar{u}_{ob} \rangle$ is determined by taking the average of all individual averaged object drifts $\langle \bar{u}_{ob} \rangle$ for each significant wave height. The values of $\langle \bar{u}_{ob} \rangle$ are given in Table 4.5. The average object drift $\langle \bar{u}_{ob} \rangle$ increases with increasing significant wave height. This is a result of an increasing Stokes drift and a larger number of breaking waves. The characteristic Stokes drift at the surface for deep water unidirectional monochromatic waves $\bar{u}_{st} = \omega k a^2$ can be written in terms of the peak period T_p and wave amplitude $a = H_s/2$ using linear wave theory:

$$\bar{u}_{s,ch} = \frac{(2\pi)^3}{g{T_p}^3} a^2 \ , \tag{4.13}$$

Where the peak period T_p is 1.2 s for all experiments. Hence, the only variable is the wave amplitude. The relation between the Stokes drift and wave amplitude is positive and quadratic. Therefore, an increase in significant wave height results in an increase of the Stokes drift along with the average object drift. Besides, during breaking events, particles travel larger distances over a shorter period, leading to an increase in the average object drift. These breaking events were observed to increase for larger significant wave heights during the experiments. Breaking is known to occur for steep waves. The characteristic wave steepness ϵ_{ch} is related to the peak wave number k_p and the significant wave height H_s by:

$$\epsilon_{ch} = k_p H_s/2 \ , \tag{4.14}$$

Similar to the Stokes drift, the dispersion relation is used to rewrite the peak wave number k_p in terms of the peak period T_p, which remains constant. Again, the only remaining variable of the characteristic steepness is the significant wave height. The characteristic steepness is positively related and therefore increases with increasing significant wave height. Once the waves become steeper they become more unstable. Unstable waves lead to an increase in the number of breaking events and hence, an increase of the average object drift $\langle \bar{u}_{ob} \rangle$.

Table 4.5 The average drift $\langle \bar{u}_{ob} \rangle$ of the trajectories from the particles per significant wave height H_s

H_s [cm]	Number of particles [#]	$\langle \bar{u}_{ob} \rangle$ [mm/s]
5	168	14.92
9	160	22.05
13	85	31.05
17	148	33.26

4.3.2 Wave breaking identification

Deep-water waves break when their steepness exceeds a threshold. Breaking waves in the ocean consist of plunging and spilling breakers. Plunging breakers were not observed during the experiment. Therefore, we limit ourselves to spilling breakers. The phenomenon of a spilling breaker is characterized by the top of the wave spilling over the front of the wave. In those cases, the velocity of the water particles on the surface can be significantly larger than for non-breaking waves (Lenain, Pizzo, & Melville, 2019). When a plastic particle is caught by a wave-breaking front a strong increase in the forward travelled distance is observed in the data. This can be seen in figure 4.6, where the Lagrangian trajectory of a particle has an oscillatory motion for non-breaking waves and a sudden steep jump for breaking waves, whereafter it returns to the oscillatory motion. However, as mentioned particles located further away from the onset of the breaking front experience a smaller jump but still experience a larger velocity than non-breaking waves.

Hence, characteristics of a breaking wave are the increase in distance travelled and an increase in velocity of the particles compared to the dominant oscillatory motion. In this research, 2 criteria are defined to identify breaking waves based on these characteristics. The results of both criteria are subsequently combined to get the most accurate estimation of the breaking events. The first method associates the periodic movement of the spheres with the periodic movement of the waves. The mot-

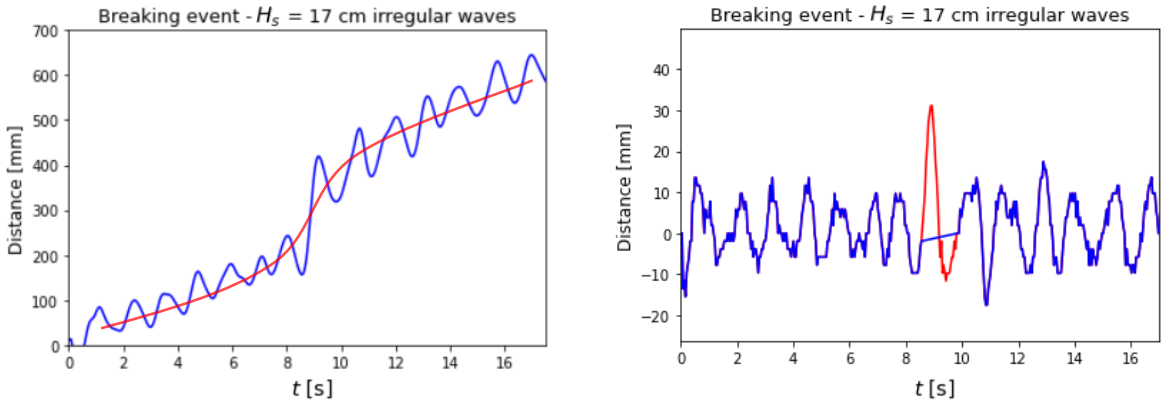

figure 4.6 left the cumulative trajectory of a particle showing an indication of breaking between t = 8 and t = 10 s. The red line shows the average speeds which increases significantly in-between t = 8 and t = 10 s. Right shows in red an identified breaking wave in the oscillations of a trajectory. The travelled distance appears to be significantly larger for breaking waves.

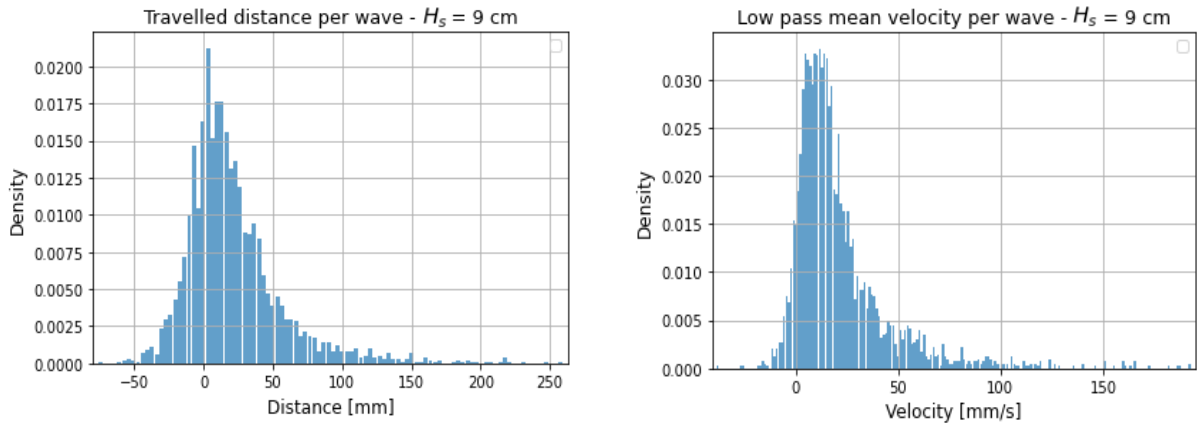

figure 4.7 left the distance travelled by a particle in individual breaking or nonbreaking waves. Right, the average velocity experienced by a particle in individual breaking or nonbreaking waves.

ion of the spheres is a result of the motion of the wave it encounters. A breaking wave will give a large positive jump as can be seen in figure 4.6. Therefore, the distance it travels is proportional to the wave characteristics. To identify the waves in the trajectories of the particles a zero up-crossing analyses is applied. However, due to the noise in the signal unrealistically small waves are encountered. Therefore, a Fourier transform on the motion of the particles is applied and a low pass filter is used on the spectrum to remove the high frequencies and de-noise the signal. The 70th percentile of the spectrum is taken as a hard boundary for the filter. Using this boundary, the periodic motion was still followed accurately but the noise was removed. Subsequently, a zero-up crossing is applied to the de-noised signal and the individual waves are given an identification number. For each wave, the distance it travels per consecutive time frame is summed, giving the total travelled distance per wave for a single particle $\Delta x_{ob,w}$. Figure 4.7 shows the total travelled distance of a particle for all individual waves that are encountered by 19 particles for a single video with input significant wave height H_s = 9 cm. For the breaking criteria, the waves beyond the 50th percentile of the travelled distance distribution are taken to optimize the calculation time. Besides, the 50th percentile is a first estimate as this is where breaking occurs. However, within the 50th percentile, a lot of non-breaking waves are also present. Especially for the smaller values exceeding the 50th percentile threshold.

Sporadically, large travelled distances can be the result of weak backward-moving motions over a wave period that might occur. Therefore, method 2 is applied. Method 2 takes into account the slope of wave motion, or in other words, the velocity that the particles encounter during the passing of a wave. A low pass filter is applied on the spectrum of the trajectories and filters out all Fourier components above 0.5*f_p. The fast oscillations from the high frequencies are removed and only the low frequencies remain. In this way, a much steeper slope is observed for breaking events when the distance travelled is plotted over time. Similar to method 1, method 2 identifies the individual waves using zero up-crossing. The slope from the low pass filter corresponding to the wave is matched based on their moment in time. The slope is averaged over the wave motion to obtain the average velocity $\bar{u}_w$ of the particle during an identified wave. For the breaking criterion, the maximum possible Stokes drift $\bar{u}_{st,\eta,tr}$ is calculated from the surface elevation data $\eta(t)$ by employing the maximum steepness criteria for waves ϵ_{tr} = 0.25. For the largest non-breaking wave, the Stokes drift is calculated using linear theory and Stokes formulation $\bar{u}_{st} = \omega k a^2$. Because, this maximum value is calculated from the surface elevation measurements, the Eulerian current is not taken into account. However, the particles do experience the Eulerian current. Therefore, The threshold is formulated by the Stokes drift of the largest non-breaking wave $\bar{u}_{st,\eta,tr}$ minus the average Eulerian current $\bar{u}_{0.2\,EMS}$. This threshold is equal to two times or more the measures Stokes drift for the different H_s. In summary,

the breaking criteria are: $\Delta x_{ob,w} > 0$ and $\bar{u}_{ob,w} > (\bar{u}_{st,\eta,tr} - \bar{u}_{0.2\,EMS})$. The identified breaking waves from both methods are compared and if they match in time the wave is considered a definite breaking event. After removal of breaking waves on the average object drift $\langle \bar{u}_{ob} \rangle$, the average velocities of the trajectories are decreased. The average object drift without breaking waves per significant wave height input will be denoted by $\langle \bar{u}_{ob} \rangle_{H_s - Br}$. Table 4.6 gives an overview of the average object drift $\langle \bar{u}_{ob} \rangle$and the new average object drift without breaking $\langle \bar{u}_{ob} \rangle_{H_s - Br}$. for all significant wave height conditions. The average drift induced by breaking $\langle \bar{u}_{br,ob} \rangle$ on the average drift $\langle \bar{u}_{ob} \rangle$ from thetrajectories of the particles is calculated by:

$$\langle \bar{u}_{br,ob} \rangle = \langle \bar{u}_{ob} \rangle - \langle \bar{u}_{ob-Br} \rangle \ , \tag{4.15}$$

Table 4.6 The average object drift per significant wave height $\langle \bar{u}_{ob} \rangle$, the average object drift without breaking $\langle \bar{u}_{ob-Br} \rangle$, and the average breaking induced drift $\bar{u}_{breaking}$.

H_s [cm]	$\langle \bar{u}_{ob} \rangle$ [mm/s]	$\langle \bar{u}_{ob-Br} \rangle$[mm/s]	$\langle \bar{u}_{br,ob} \rangle$ [mm/s]
5	14.92	14.81	0.11
9	22.05	19.77	2.28
13	31.05	23.77	7.28
17	33.26	22.58	10.68

4.4 Discussing the experimental results

In this section, the results of the transport are presented and discussed. First, the wave-breaking-induced transport is discussed for the different significant wave height conditions. Subsequently, the quantified wave-breaking-induced transport is used to calculate an enhancement factor, which calculates the enhancement of the Stokes-induced transport by the wave-breaking-induced transport. Lastly, the sensitivity of the enhancement factor is analysed based on the breaking threshold.

4.4.1 Discussing the breaking induced transport

The transport of breaking waves is obtained from four different input significant wave height conditions H_s = 5, 9, 13, and 17 cm. Figure 4.8 show the transport for the breaking waves in H_s = 9 cm and H_s = 17 cm, respectively. For the significant wave height case H_s = 17 cm, the steepness is larger than for H_s = 9 cm. The strength and number of the breaking events increase with wave steepness as discussed in section 4.1.3. As a result, the transport $\langle \delta x \rangle$ is much larger and more numerous for H_s = 17 compared to H_s = 9 cm. Besides, the results show values for the transport below 1 m for H_s = 9 cm, while H_s = 17 cm does not show these values. Even though contact events

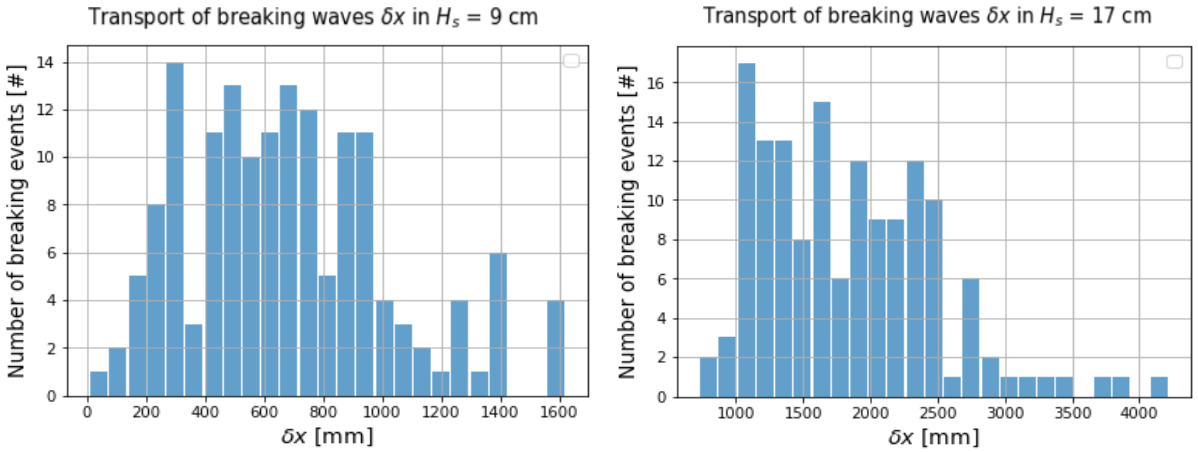

Figure 4.8 The transport of identified breaking waves on the left for H_s = 9 cm and on the right for H_s = 17 cm. The histograms show that the strength of the breaking events is larger for H_s = 17 cm, because the values for the transport are larger.

should be present for particles in both significant wave height cases. This could be an indication that the threshold for breaking waves is too large for H_s = 17 cm.

4.4.2 Calculating the enhancement factor

To approximate how much the transport from the Stokes drift is enhanced by the identified breaking waves in the trajectories of the particles, an enhancement factor χ_{ob} for the transport of non-breaking waves is calculated for each input significant wave height case H_s. To do this, the transport of the breaking waves is removed from the total transport. What remains are two datasets. One dataset contains the transport of the breaking waves $\delta x_{br,ob}$ and the other one contains the transport of the non-breaking waves, which are also influenced by the current $\delta x_{s+c,ob}$. The transport of the breaking waves $\delta x_{br,ob}$ is summed to obtain the total wave-breaking-induced transport.

The transport from the Stokes drift is obtained by summing the transport of the nonbreaking waves in the trajectories of the particles. However, the Stokes drift is influenced by the return current. Therefore, the measured return current $\bar{u}_{0.2\,EMS}$ is multiplied by the total duration of non-breaking waves in the trajectories of the particles $T_{s,ob}$ and added to the total transport without breaking waves. Hence, the total Stokes transport is calculated by:

$$\Sigma\delta x_{s,ob} = \Sigma\delta x_{s+c,ob} + \bar{u}_{0.2\,EMS}\, T_{s,ob} \ , \tag{4.16}$$

it is assumed that the breaking transport is not influenced by the return current. Subsequently, the Stokes transport enhancement factor χ_η is calculated by

$$\chi_{ob} = \frac{\Sigma\delta x_{s,ob} + \Sigma\delta x_{br,ob}}{\Sigma\delta x_{s,ob}} \ , \tag{4.17}$$

where $\Sigma\delta x_{br,ob}$ is the summation of the wave-breaking-induced transport. The values for χ_η are shown in table 4.7. For H_s = 5 cm no breaking waves are identified by the model. Thus, the enhancement factor is 1. When the input significant wave height increases, the enhancement factor takes on a visually observed linear trend. The drift due to breaking is enhanced up to 1.76 times the Stokes transport for H_s = 17 cm. However, this enhancement factor takes into account all breaking waves. Therefore, when comparing the drift enhancement factor χ_{ob} with the number of breaking waves derived from the trajectories of the particles in the Deltares experiment a probability factor should be taken into account. Otherwise, the drift enhancement factor overestimates the enhanced experimental drift. This probability factor is related to the average number of breaking waves encountered by the particles.

Table 4.7 The total Stokes transport $\Sigma\delta x_{s,ob}$, the total breaking induced transport $\Sigma\delta x_{br,ob}$, and the enhancement factor of the Stokes transport χ_{ob}.

H_s [cm]	χ_{ob}
5	1.01
9	1.22
13	1.45
17	1.65

4.4.3 Sensitivity of the enhancement factor

In this section, the sensitivity of the enhancement factor is examined based on the wave-breaking threshold discussed in section 4.3.2. It was argued that the value for the steepness threshold ϵ_{tr} was 0.2, as it corresponded best to existing research and hydrodynamics in the tank. To examine the

sensitivity, the value for the breaking threshold is varied. The range of the variation of the steepness threshold is based on potential values discussed in section 4.1.3. Research showed that the deviation of the threshold was in the range of 0.02. Therefore, the enhancement factor is calculated for ϵ_{tr} = 0.24 and ϵ_{tr} = 0.20. The results are shown in figure 4.9 by a green shaded interval. This interval increases with increasing significant wave height conditions H_s. This can be explained by looking at the number and strength of the breaking events for different H_s. Table 4.8 shows that changing ϵ_{tr} has a larger influence on the number of breaking events for H_s = 13 and 17 cm than for H_s = 5 and 9 cm. The larger H_s conditions have stronger breaking events. Therefore, more contact events occur between the particles and the wave-breaking front compared to lower H_s conditions. Because the average speed of a particle during the cycle of a wave is used these small contact events only slightly enhance its average drift. Therefore, much more of these average drifts for larger H_s are close to the threshold for breaking. The enhancement factor is strongly influenced by the large number of average drifts that are taken into account. Hence, the range of the enhancement factor increases strongly with increasing significant wave heights.

Table 4.8 The percentages of breaking waves per significant wave height conditions H_s and steepness threshold ϵ_{tr}.

H_s [cm]	ϵ_{tr} = 0.20 [%]	ϵ_{tr} = 0.22 [%]	ϵ_{tr} = 0.24 [%]
5	0.29	0.14	0.13
9	4.14	2.24	1.51
13	9.02	5.25	3.42
17	10.94	8.15	5.21

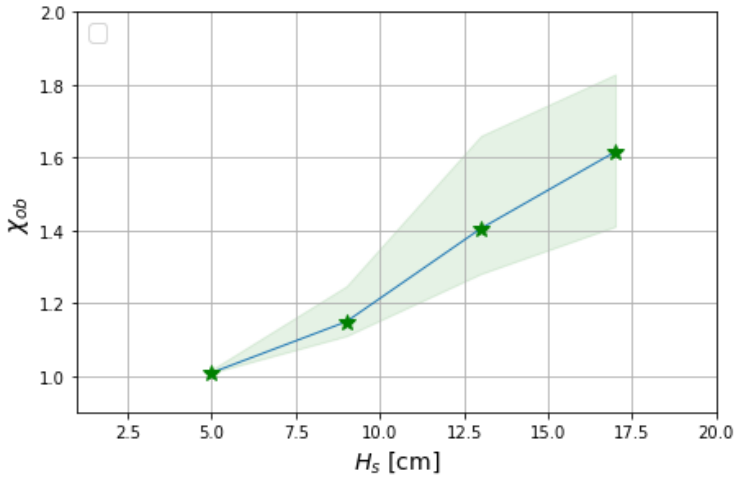

figure 4.9 The nhancement factor χ_{ob} per input significant wave height H_s condition inlcuding the error margin. The error margin increases for wave fields with larger H_s.

5

Theoretical model description

The analysis of wave-breaking in the ocean has been going on for more than a century. Series of laboratory experiments, deployment of instrumentation at sea, and numerical simulations have led to a number of empirical and theoretical relations describing the strength and threshold of breaking events. However, a model that quantifies the breaking-induced drift at the surface of deep-water irregular seas does not yet exist. The most recent research into wave-breaking-induced drift has been conducted by Sinnis et al. (2021). The transport relation for breaking waves developed by Sinnis et al. is based on the characteristics of isolated wave groups. However, a single wave group is not representative of a real sea state. Therefore, in this chapter, I will extend the transport function for a isolated breaking wave group to a unidirectional random sea. I will do this by approximating the surface elevation of a deep water irregular unidirectional sea as a summation of Gaussian wave groups. Subsequently, the transport relation from Sinnis et al. is used to calculate the transport for the breaking Gaussian wave groups. Finally, an enhancement factor is calculated, which quantifies the enhancement of the surface transport from non-breaking waves by breaking waves in four different significant wave height conditions.

5.1 Analysis of the transport model for a single breaking wave group

Quantifying the transport by breaking wave groups is a recent line of research. Initially, Lenain, Pizzo, and Melville (2016) and Deike et al. (2017) found that the steepness of the wave groups was the main contributor to the transport of breaking wave groups. More recent research by Sinnis et al. (2021) showed that the spectral bandwidth of the wave groups also makes a significant contribution to transport. In their research, Sinnis et al. quantified the transport for isolated wave groups based on the spectral bandwidth Δ and linear slope S. Their relationship for the transport of breaking wave groups will be referred to as the Sinnis relationship throughout this chapter. The relationship defined by Sinnis et al. for the transport induced by breaking and nonbreaking waves is:

$$u_{L,S} = \frac{\delta x}{T}, \tag{5.1}$$

$$\delta x k_c \Delta = \chi_l \sqrt{S - S_*} + \beta, \tag{5.2}$$

wherein $u_{L,S}$ is the Lagrangian speed of a fluid particle, δx is the average transport for a breaking or nonbreaking wave group, T is the wave period, k_c is the spectral wavenumber, Δ the non-dimensional spectral bandwidth, S the linear slope of the wave group, and S_* the breaking threshold. The last five variables are wave group characteristics. Furthermore, χ_l is a scaling factor and β describes the relationship between the slope of the wave group and the transport for non-breaking waves ($\beta \propto S^2$). (5.2) shows that the linear slope determines the strength of breaking. Larger S implies a larger wave height at breaking and, as a result, more transport, while a larger bandwidth (i.e., narrower wave group) decreases the transport.

This relationship was established from experimental results, where breaking wave groups were generated using a dispersive focusing technique. From this technique, the location of breaking could be determined by modifying the phase of a finite band of waves. At the location of breaking, the amplitudes of these wave components become superimposed. Following Drazen et al. (2008), the time series of the free surface $\eta(t)$ at the location of focusing of the wave groups in this experiment were of the form:

$$\eta(t) = \sum_{n}^{N} a_n \cos(\omega_n (t - t_b)) \,, \tag{5.3}$$

where a_n is the amplitude of the nth Fourier component, $\omega_n = 2\pi f_n$ the radian frequency of the Fourier component, and t_b is the moment in time when the wave packet focusses as predicted by linear theory. Because the peak wave period used in the experiment from Sinnis et al. is not an integer, the endpoints of the surface elevation are discontinuous. These artificial discontinuities show up in the Fourier transform as high-frequency components which are not present in the original signal. The energy spectrum given by the Fourier transform is, therefore, not the actual spectrum. The energy appears smeared over the frequencies (Cerna & Harvey, 2000). Therefore, the wave train described by (5.3) is windowed in frequency space, so that only a single wave packet is generated as the amplitude goes smoothly to zero toward the endpoints. This wave packet is characterized by the non-dimensional spectral bandwidth Δ_{Sinnis} and the linear prediction of the slope S_{Sinnis}. Physically, the linear prediction of the slope is a measure of the nonlinearity of the system and determines the height of the wave group, while the bandwidth is a measure of the time (or equivalently space) scale over which the waves interact (i.e. the width of the wave group). The larger the bandwidth, the narrower the width of the wave group, and the larger the slope the more nonlinear the wave group. Both measures are non-dimensional. Hence, the width and height of the wave groups were modified by the non-dimensional spectral bandwidth and the linear slope, respectively. For different combinations of the spectral bandwidth and the linear slope, the transport of breaking wave groups was measured.

Furthermore, to simplify the spectrum, the formulation by Drazen et al. applies the constant-amplitude approach to the spectral shape. This approach sets the amplitudes a_n of all wave components equal. Therefore, at the location of breaking, the maximum height of the surface elevation η_{max} is simply defined by multiplying the number of components N by the amplitude a_n. Hence, $\eta_{max} = N a_n$. Consequently, the constant amplitude method will result in a uniformly distributed spectrum. This uniform spectral distribution allows for a clear definition of the bandwidth around the central frequency f_c. The normalized bandwidth Δ_{Sinnis} is defined as:

$$\Delta_{Sinnis} \equiv \frac{f_N - f_1}{f_c} \,, \tag{5.4}$$

where f_N is the highest frequency, f_1 is the lowest frequency, f_c is the central frequency, and N is the number of Fourier components. From the frequency spectrum, the wave numbers k_n are calculated using the linear dispersion relation $\omega_n^2 = g k_n \tanh(k_n d)$ and $f_n = 2\pi/\omega_n$, where d is the water depth, g is the gravitational constant and ω the angular frequency. The wavenumbers (associated with the length scale $L = 2\pi/k$) together with the height of the wave group η_{max} characterize the slope. The linear prediction of the maximum slope S at focus is then defined by:

$$S = \sum_{n=1}^{N} a_n k_n \,, \tag{5.5}$$

where a_n is the amplitude and k_n the wavenumber of the nth Fourier component. Using (5.3), (5.4), and (5.5), the surface elevation time series from the experiments of Sinnis et al. can be recreated. The importance of recreating this surface elevation time series lies in the extension of the Sinnis relationship to the wave groups of an irregular sea. This is explained in paragraph 5.2.

5.2 Developing a transport model for a unidirectional random sea

The transport relationship from Sinnis et al. for isolated wave groups is at the basis of the developed transport model for a unidirectional random sea. The developed model aims to isolate the wave groups in the surface elevation time series, whereafter the transport relationship from Sinnis et al. can be applied to those isolated wave groups. In this section, it is explained how the wave groups from surface elevation measurements of the Deltares experiment are isolated.

There are many options for identifying wave groups as discussed in paragraph 1.1.1. In this research, the envelope approach from Longuet-Hoggins (1984) is used to identify the wave groups. The main challenge, however, is to obtain the relevant parameters from the identified wave groups. Most theory defining the characteristics of the wave groups discusses the relation between spectral shape and wave grouping (Goda (1970), Battjes and van Vledder (1984). Mere averages of the wave group characteristics are usually obtained. The characteristics of isolated wave groups in an irregular wave spectrum do not have universal formulations. Another complicating factor is that the wave groups generated in the experiments from Sinnis et al. are based on the assumption that the variance density spectrum follows a uniform distribution, while the variance density spectrum from the Deltares experiment follows a JONSWAP shape, which means that the spectral bandwidth Δ_{Sinnis} of the identified wave groups in the experiment from Deltares cannot be obtained using (5.4). Thus, the wave groups in the measured surface elevation need to be isolated and also be related to wave groups of the experiment from Sinnis et al. to obtain the wave group characteristics and apply the transport relationship.

To do this, a simplified approximation is made of the measured surface elevation spectrum. Gaussian wave groups are used to recreate the surface elevations. The Gaussian wave groups are similar in shape and energy to the wave groups from the measured wave spectrum. Gaussian refers to the shape of the energy spectrum of the wave groups, which is equal to a Gaussian distribution. The Gaussian wave groups can be seen as a bridge between the isolated wave groups from Sinnis et al. and the isolated wave groups from the Deltares experiment. The energy and shape of the spectrum of Gaussian wave groups are similar to the JONSWAP spectral shape of the Deltares Experiment as can be seen in Figure 5.1. Besides, the symmetrical spectral shape of the Gaussian wave groups allows for a clear definition of the non-dimensional bandwidth and linear slope, from which the transport relationship from Sinnis et al. can be applied. However, some differences between the Gaussian and JONSWAP spectra regarding the spectral bandwidth are present, which become clear when comparing the definitions of both energy density spectra:

$$E_{JONSWAP}(f) = \alpha g^2 (2\pi)^{-4} f^{-5} \exp\left[-\frac{5}{4}\left(\frac{f}{f_p}\right)^{-4}\right] \gamma^{\exp\left[-\frac{(f-f_p)^2}{2\sigma_{JONSWAP}{}^2}\right]}, \tag{5.6}$$

$$E_{Gaussian}(f) = \frac{H_s^2}{4} \frac{1}{\sigma_{Gauss}\sqrt{2\pi}} \exp\left[-\frac{(f-f_p)^2}{2\sigma_{Gauss}{}^2}\right], \tag{5.7}$$

where the relevant parameters describing the non-dimensional bandwidth of the JONSWAP spectrum are the enhancement factor γ and the width $\sigma_{JONSWAP}$, while for the Gaussian spectrum only the width

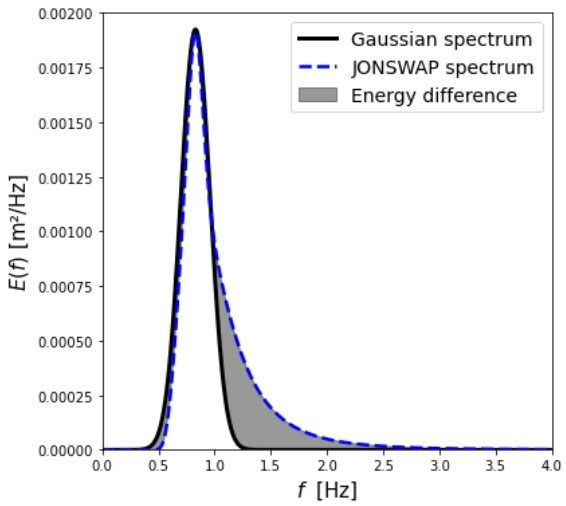

Figure 5.1 (a) The energy spectrum of the measurements with the Gaussian and JONSWAP shapes plotted over it (b) The surface elevation measured from wave gauge 3 corresponding to a wide variance density spectrum. The wave groups are harder to distinguish.

parameter σ_{Gauss} determines the non-dimensional bandwidth. Increasing the enhancement factor localises and increases the energy of the wave field around the peak frequency, while also increasing the spectral bandwidth. For the Gaussian wave group, the energy can only be more localized around the peak frequency when the spectral bandwidth is decreased. Therefore, for JONSWAP spectra with large enhancement factors, the Gaussian approximation becomes less accurate because the deviation in energy between the two spectra increases with the increasing value of the enhancement factor. Furthermore, Figure 5.1 shows that the Gaussian and JONSWAP spectral shapes are different in energy. The JONSWAP spectrum has more energy located in the tail, which is not present in the Gaussian spectrum. This error in energy is an inevitable result of the simplification by the Gaussian spectrum. Therefore, the aim is to define the approximated wave groups such that the error between both energy spectra is minimal.

To approximate the wave groups from the measured surface elevation spectrum by Gaussian wave groups, several steps are taken. First, the wave groups from the measured surface elevation spectrum are identified. This is done using the envelope approach introduced by Longuet-Higgins (1984). In this approach, a wave group is considered to be composed of all waves exceeding a specified elevation threshold during two consecutive up-crossings of an envelope. Therefore, the envelope of the measured surface elevation is calculated using the maximum crest height of the individual waves and cubically interpolating between the crests. It is assumed that wave groups only occur for peaks exceeding a threshold of 0.1 times the input significant wave height H_s to prevent small positive disturbances around the mean water level to be identified as wave groups. Figure 5.2a shows the envelope of the measured surface elevation and the threshold level. The wave groups are defined between two up-crossings of the envelope or by the 'peaks' (i.e. maximum elevation of the envelope of the wave group) in between two up-crossings. At the location where the envelope has peaks exceeding the threshold level $0.1H_s$, a wave group is identified. Therefore, the envelope of a Gaussian wave group is applied to these peaks from which the Gaussian wave group can be generated. However, because of the strongly irregular behaviour of the measured surface elevation, peaks occur in short sequence as can be seen at $t \approx 62$ s and at $t \approx 63$ s in figure 5.2a. It is more likely that these are two peaks in the same wave group. Hence, the approach from Longuet-Higgins is likely to underestimate the group length. For that reason, to avoid fitting multiple Gaussians to the same wave group, the minimal distance between two peaks is set to 6 seconds. The largest waves in wave groups are generally at the centre of the wave group (Holthuijsen, 2007). Thus, multiple peaks are primarily

present within 5 waves located at the centre of the group. This is additionally confirmed visually from the measured surface elevation data. Hence, with a peak period of 1.2 seconds and a spread of approximately 5 waves, the minimal distance between peaks is set to 6 seconds to avoid multiple peaks in the same wave group. Hence, the wave groups are identified from the peaks of the envelope.

Secondly, to generate Gaussian wave groups at the location of the identified wave groups from the measured surface elevation the envelope of the Gaussian wave group is fitted to the identified peaks using the following formula:

$$\eta_{G,env}(t) = Ae^{-\frac{(t-t_0)^2}{2(\frac{1}{2}w\Delta t)^2}}, \tag{5.8}$$

where $\eta_{G,env}(t)$ is the envelope of a single Gaussian group, A is the maximum surface elevation of the peak, t_0 is the location of the peak at the centre of the envelope, Δt is the time step and w is the non-dimensional width of the Gaussian envelope. The deviation of the Gaussian wave group in (5

.6) is expressed in the number of time steps so that the non-dimensional width w is multiplied by Δt to obtain the width in seconds $w\Delta t$. The maximum elevation A and location of the peak t_0 are obtained from the maximum value of the envelope of the wave group (i.e. the peak) as can be seen in Figure 5.2b. The non-dimensional width of the wave group is iteratively determined based on the error between the envelope of the measured surface elevation spectrum and the Gaussian envelope of the approximated surface elevation spectrum. This means that the Gaussian envelope of all individual wave groups is merged. To do this merge, first, the Gaussian envelopes are fitted to the peaks as shown in Figure 5.2c. Thereafter, the envelopes are merged. As can be seen from figure 5.2d, where the envelopes of the Gaussian wave groups may overlap, where the maximum value is used for the locations of overlapping envelopes. Subsequently, the error between the envelope of the approximated Gaussian surface elevation spectrum and the envelope of the measured surface elevations spectrum is calculated for which the non-dimensional width w is changed until the error between the envelopes of both spectra is minimal:

$$w = \underset{w}{\operatorname{argmin}} \sum_{t=0}^{n} (\eta_{env}(t) - \eta_{G,env,m}(t,w))^2 , \tag{5.9}$$

in which $\eta_{env}(t)$ is the envelope of the measured spectrum, $\eta_{G,env,m}(t,w)$ is the merged envelope for the approximated Gaussian spectrum for a specific non-dimensional width w, and n is the number of time steps Δt. After defining all parameters from the surface elevation and the optimal non-dimensional width w, the isolated Gaussian wave groups are generated (Figure 5.3a). The Gaussian wave groups consist of a carrier wave a period T of 1.2 s corresponding to the input peak period of the experiments. The carrier wave is a linear wave for which the amplitude follows the shape of the Gaussian envelope. The surface elevation of the isolated Gaussian wave group (i.e. carrier wave) $\eta_{G,c}(t)$ is defined by:

$$\eta_{G,c}(t) = Ae^{-\frac{(t-t_0)^2}{2(\frac{1}{2}w\Delta t)^2}} \cos(2\pi f t), \tag{5.10}$$

where f is the frequency of the carrier wave, which is equal to the inverse of the input period T^{-1}. (5.7) gives the isolated Gaussian wave groups. In order to get approximated surface elevation spectrum

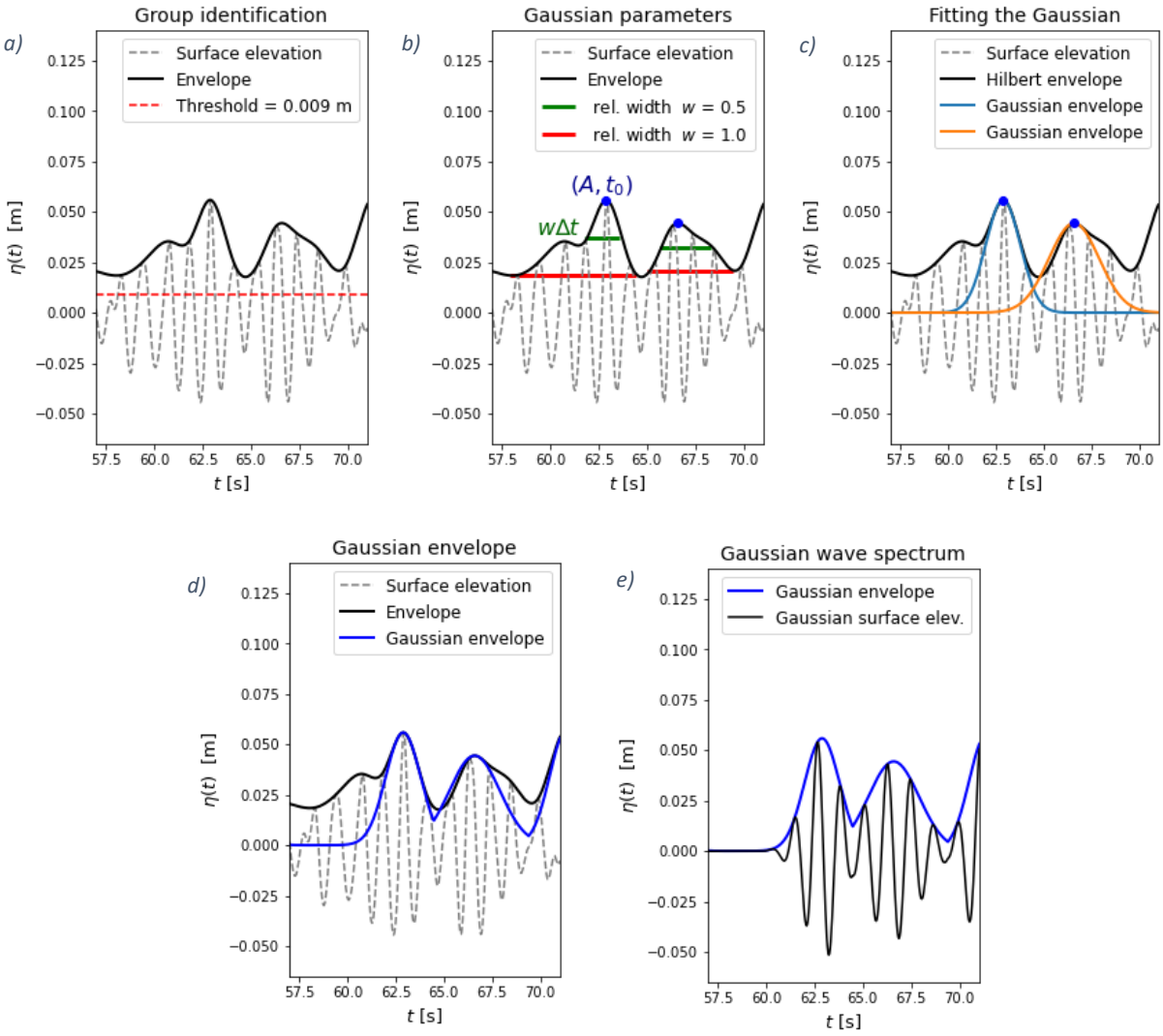

figure 5.2 (a) Identification of the wave group based on the threshold and envelope. (b) Obtaining the wave group characteristics to define the Gaussian envelope. (c) Plotting the Gaussian envelopes to the peaks. (d) Merging the envelopes of the Gaussian wave groups. (d) Generating the new surface elevation spectrum below the wave groups.

for the whole time series, the envelope of the merged Gaussian envelope is used. Below the merged Gaussian wave envelope the spectrum is generated similarly to (5.7). The results of the approximated surface elevation spectrum using Gaussian wave groups is shown in Figure 5.2e.

Furthermore, it should be noted that the carrier wave in the Gaussian wave group is linear. Second-order effects are therefore not taken into account resulting in a deviation of energy between the Gaussian wave groups and the wave groups from the measured surface elevation. These nonlinearities occurred during the experiment and caused the waves to have sharper crests and flatter troughs. To examine the contribution of these nonlinearities to the energy the formulation by Stokes (1847) for nonlinear waves in deep water is used (Holthuijsen, 2007):

$$\eta(x,t) = \varepsilon\eta_1(x,t) + \varepsilon^2\eta_2(x,t) \ , \tag{5.11}$$

where $\eta(x,t)$ is the surface elevation of the nonlinear wave, $\eta_1(x,t)$ is the base harmonic, $\eta_2(x,t)$ is the added harmonic and $\varepsilon = (ak)$ is the steepness of the wave with a the amplitude and k the wave

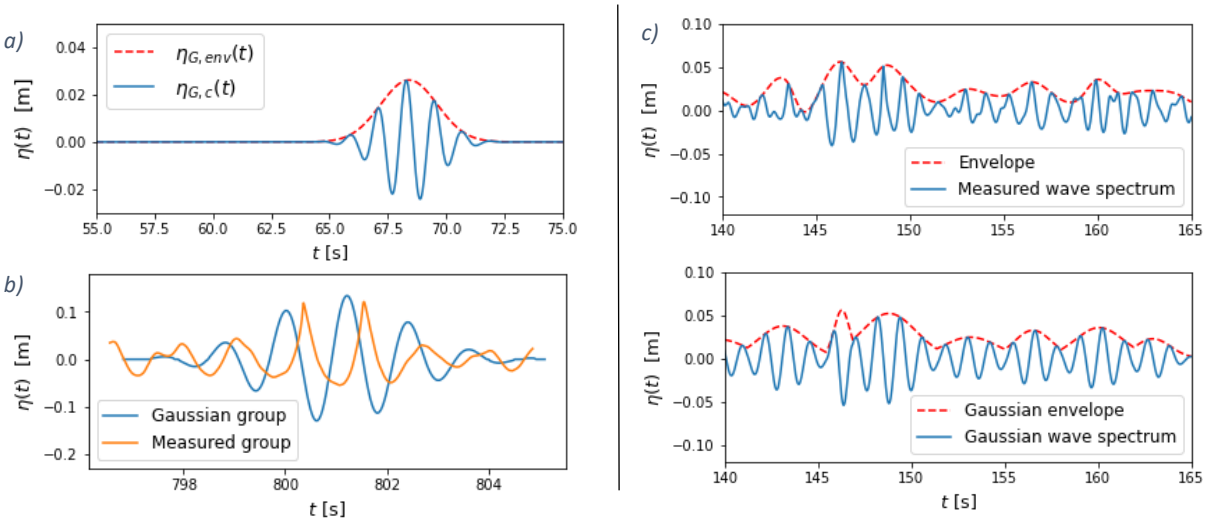

figure 5.3 (a) A generated Gaussian wave group. (b) A comparison between a Gaussian wave group and the wave group it approximates based on the surface elevation time series. (c) The upper figure shows the measured surface elevation spectrum and the bottom figure shows the approximated Gaussian spectrum.

number. The contribution of the base harmonic to the nonlinear wave is calculated using the characteristic steepness ε_{ch} by $\varepsilon_{ch}/(\varepsilon_{ch}+{\varepsilon_{ch}}^2)$. It is found that for all input significant wave height conditions H_s, the contribution of the base harmonic is larger than 90%. Additionally, the corrections of the added harmonics in the amplitude of the surface elevation are minor. The latter results in the amplitude of the added harmonic to be smaller than that of the base harmonic. Thus, due to the small contribution of the amplitude of the nonlinear term we argue that the energy is affected minimally and therefore their energy is neglected.

5.3 Transport model parameters

In this paragraph, the non-dimensional spectral bandwidth and linear slope are calculated from the Gaussian wave group and related to the wave groups from the experiment of Sinnis et al. to calculate the wave-breaking-induced transport for the isolated Gaussian wave groups in the approximated surface elevation spectrum defined in paragraph 5.2.

5.3.1 Deriving the wave group characteristics

The characteristics required from the Gaussian wave groups are the linear slope, spectral wave number, and spectral bandwidth in order to calculate the wave-breaking-induced transport. The bandwidth of the Gaussian wave group is discussed first. The formulation of the Gaussian spectral bandwidth is defined based on the length scale of the wave group (Calvert, et al., 2019). The length scale of the modulation is equal to the standard deviation of the Gaussian envelope: $\sigma = 0.5w\Delta t$. The normalized bandwidth Δ_{Gaus} for the Gaussian wave groups with a narrow-banded spectrum centered around the carrier wave is defined by:

$$\Delta_{Gaus} \equiv \frac{1}{k_0\sigma}, \tag{5.12}$$

where k_0 denotes the carrier wave number and σ the packet length scale. The carrier wave number k_0 is calculated using the peak period of the carrier wave T_0 and the dispersion relation: $k_0 = (2\pi/T_0)^2/g$. The carrier wave number k_0 is also equal to the spectral wave number k_c. The length scale σ from the standard deviation from (5.8) has its units in seconds, which has to be converted to a length scale. This is done by multiplying the standard deviation of the Gaussian envelope $\eta_{G,c}(t)$ by two times the group velocity c_g (The derivation is shown in Appendix B). The group velocity c_g is

calculated from the phase velocity of the carrier wave $c = gT_0/2\pi$ and the deep water assumption ($k_0 d \gg 1$) wherein $c_g = 0.5c$.

For the calculation of the Gaussian linear slope $S_{Gaussian}$ the same formula is used as for the wave groups generated by $S_{Sinnis} = \Sigma a_n k_n$. However, not all Fourier components are taken into account for the summation. The amplitude spectrum contains a several nonlinear frequencies even though the carrier wave is linear. These frequencies are not a result of lower or higher harmonic components induced by hydraulic processes in the basin but result from the Fourier transform of the Gaussian wave group, which results in a Gaussian-shaped spectrum again with an infinite tail. The dependence of the slope S can be significant for this tail because the wave number k_n is related to the frequencies by the dispersion relation $k_n = (2\pi f_i)^2/g$. Hence, the slope is enhanced even more by the quadratic relation for the higher frequency components. Therefore, to comply with the linear assumption, only the components that lie around the central frequency $f_0 = f_c$ and bandwidth Δ_{Sinnis} are used. The bandwidth is increased slightly until the value of the linear slope almost remains constant. In this way, the frequencies in the tail are not taken into account resulting in a better estimation of the linear slope. The bandwidth used for this linear prediction is the Sinnis bandwidth Δ_{Sinnis}, because it is directly related to the frequency spectrum. Consequently, the corresponding Gaussian bandwidth Δ_{Gaus} is converted to the bandwidth from Sinnis et al. Δ_{Sinnis}. This is done using a linear relationship between both bandwidths, which is described in more detail in paragraph 5.3.1.1.

5.3.1.1 Relating the wave group characteristics

The normalized bandwidth Δ_{Sinnis} defined in Sinnis et al. is based on the width of the frequency range Δf, the central frequency f_c and the assumption that the frequency spectrum follows a uniform distribution. This formulation differs from the Gaussian bandwidth Δ_{Gaus}, in the sense that the bandwidth of the Gaussian wave groups is based on the length scale σ of the wave group. For this reason, a relationship is established between the Gaussian bandwidth and the bandwidth from Sinnis et al. to be able to calculate the transport using (5.2). Despite the fact that the same method is used to calculate the linear slope for both wave groups, still some implications remain. The spectrum defined by Sinnis et al. assumes a constant amplitude for all Fourier components, while the spectrum of the Gaussian wave groups does not follow this formulation. Therefore, the values for the slope can be significantly different.

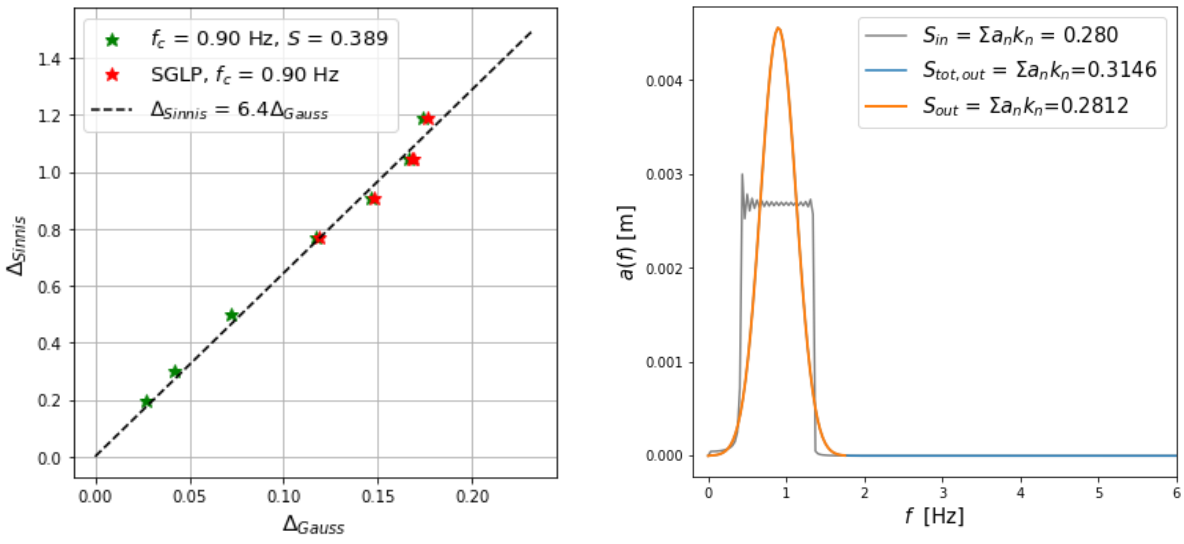

figure 5.4 (left) the linear relationship between Δ_{Sinnis} and Δ_{Gaus}. (right) The uniform and Gaussian spectra for the same wave group generated from wave group characteristics of the experiment from Sinnis et al..

With the objective to investigate the different values and obtaining a relationship, the surface elevation time series of the focussed wave groups from the experiments from Sinnis et al. are recreated using (5.3), (5.4), (5.5), and Table 1 of the paper from Sinnis et al.. The surface elevation time series of each experiment consists of an isolated focussed wave group. The focussed wave group is in turn approximated by a Gaussian wave group using the method discussed in paragraph 5.2. From the approximated Gaussian wave group, the bandwidth $\Delta_{Gaussian}$ and linear slope $S_{Gaussian}$ are calculated in accordance with paragraph 5.3. This is done for all experiments from Sinnis et al. with varying Δ_{Sinnis} and S_{Sinnis}, to determine $\Delta_{Gaussian}$ and $S_{Gaussian}$. Besides, extra focussed wave groups were created with values of Δ_{Sinnis} and S_{Sinnis} close to zero and values exceeding the experimental values from Sinnis et al. to study any implications of this relationship between wave group characteristics from Sinnis et al. and the Gaussian wave group characteristics. The wave group characteristics used for the generation of these wave groups and its relationship to the length scale σ is elaborated in more detail in Appendix C.

The values of the bandwidth are plotted and a linear curve is drawn as a best fit for the data points. Figure 5.4 shows the data points and the linear relationship between the bandwidths. The relationship is defined by:

$$\Delta_{Sinnis} = 6.4\Delta_{Gaussian}\ , \tag{5.13}$$

the wave groups in the Deltares experiment are much wider in space than the wave groups in the experiments from Sinnis et al.. Therefore, the spectral bandwidth is smaller for the Deltares experiment. The dependence on the bandwidth, however, for larger length scales σ (i.e. width) of the wave groups decreases, because the relationship between the length scale and the bandwidths is inverse (5.12), which implies that the length scale of the wave groups decreases in dependence when the bandwidth decreases.

The Gaussian spectral bandwidth can also be related to the widely used spectral bandwidth parameter ν introduced by Longuet-Higgins (1975). In his research, the bandwidth is defined based on the spectral moments: $\nu = \sqrt{m_2 m_0/m_1^2 - 1}$, where m_n is the nth moment of the energy spectrum. The energy spectrum is dependent on the length scale of the Gaussian wave group σ. Therefore, the bandwidth parameter ν can be rewritten in terms of σ. It is found that $\nu \approx 1.06\Delta_{Gaussian}$.

Furthermore, he Gaussian wave groups have approximately the same width and maximum surface elevation $\eta_{max} = \Sigma a_n$ as the wave groups from Sinnis et al., which it approximates. This is a first indication that the linear slope, which is a measure of the wave height and width (i.e. length) for both wave groups should approximately be equal. Besides, the total energy $E_{tot} = \rho g \int E(f) df$ of both wave groups should also approximately be equal. Therefore, using the requirements of conservation in maximum surface elevation η_{max}, total energy E_{tot} and requirement that the spectral distribution is symmetrical around the central frequency f_c, results in the amplitude distribution of the Gaussian spectrum to be such that the linear slope $S_{Sinnis} = \Sigma a_n k_n$ for is also conserved. This is confirmed by the calculation of the Gaussian slope for the generated wave groups from the experiment from Sinnis et al. (figure 5.4, right). It was found that the maximum deviation of the linear slope was in the order of 1% resulting from small deviations of the total energy due to the small inaccuracies in the Gaussian approximation method.

The linear slope is directly related to the wave height. In both experiments, the wave heights are in the range of 5 and 17 cm. Hence, no significant implications are expected because of the similarity in wave height. However, the central frequency f_c for both experiments is different, which does affect the

linear slope. In the Deltares experiment, the central frequency is f_c = 0.83, while in the experiment from Sinnis et al the frequency is $f_c = 0.90$. Based on the dispersion relation, the lower frequency f_c = 0.83 indicates lower wavenumbers k (i.e. larger wavelengths L, $k = 2\pi/L$). Hence, for experiments with equal linear slope S_{Sinnes} and bandwidth Δ_{Sinnis}, but with different central frequencies f_c = 0.83 and 0.90, the amplitude components a_n must be larger for the f_c = 0.83 case in order to get the same linear slope $S = \Sigma a_n k_n$. The difference in this amplitude increase, however, is in the order of millimetres, which confirms the implication for the wave height to be minimal for the different frequencies.

Additionally, when the amplitude a_n is kept constant, the linear slope S decreases for smaller frequencies f. As discussed before, smaller frequencies f have smaller wavenumbers k and therefore longer lengths L. Hence, the smaller central frequency of the Deltares experiment results in a decrease of the linear slope. Thus, with a longer wavelength and a constant wave height, the slope, which is a measure of the wave height and width (i.e. length), decreases. This decrease is in the order of 10% $((S_{Sinnis,f_c=0.83} - S_{Sinnis,f_c=0.90})/S_{Sinnis,f=0.83})$. Hence, no implications to the linear slope are expected for the smaller central frequency.

5.3.2 Setting the transport factors

The transport factors χ_l and β are two pre-determined constant values in the transport function from Sinnis, where χ_l is a scaling factor, which is determined by fitting the data points from the experimental results from Sinnis et al.. The value for the best fit in his research is χ_l = 7.39. Whereas, β is a vertical offset parameter. This parameter is the maximum-normalized surface transport, which is measured for non-breaking wave packets. The vertical offset parameter β does not vary between wave packets because it is normalized by the bandwidth and the central frequency (Sinnis et al. 2021). In the research from Sinnis et al., the offset parameter has a value of β=0.69. In their experiments, the values for χ_l and β are constant. Because the main goal of this research is to study whether the transport relationship by Sinnis et al. can approximate the transport in the unidirectional deep water random sea from the Deltares experiment. Therefore, to be consistent with the results from his research the scaling factor χ_l and offset parameter β are not changed.

5.3.3 Defining the breaking threshold for wave groups

In this research, wave breaking is associated with the exceedance of a steepness threshold. Hence, a wave group contains a breaking wave when the threshold for the linear slope S is exceeded. Using theoretical and numerical models, Pizzo and Melville found that the breaking threshold slope is a function of the spectral bandwidth Δ. In laboratory experiments from Sinnis et al. (2021), it was also found that the breaking threshold slope increases with increasing spectral bandwidth and in more recent research by Pizzo (2021), this dependence of the bandwidth with the breaking threshold slope was quantified using numerical models where the slopes and bandwidths were varied. The model was validated using the experiments from Sinnis et al. (2021) and Drazen (2008). An agreement between the numerical model and experiments was found. Therefore, the breaking threshold slope can be approximated without taking into account the rapidly varying processes that occur during the focussing of a wave group. In his research, Pizzo (2021) proposed a global criteria to predict the breaking threshold slope S_{tr} with a sole dependence on the spectral bandwidth Δ_{Sinnis}:

$$S_{tr} = -0.0579\Delta_{Sinnis}^2 + 0.2177\Delta_{Sinnis} + 0.1417 \ , \qquad (5.14)$$

when the linear slope S_{Sinnis} of a wave group is larger than the threshold value S_* breaking occurs. When S_{Sinnis} is slightly above the breaking threshold S_* a spilling breaker occurs, and as the linear slope S_{Sinnis} increases, the breaking event transitions to plunging breakers or multiple breakers in an isolated wave group. In this research, no plunging breakers were observed. Therefore, all breaking

events are considered spilling breakers. Besides, for simplification, it is assumed that only a single wave breaks per wave group. Furthermore, due to the quadratic term in (5.14), the dependence of the bandwidth to the slope becomes stronger for narrower banded wave groups (i.e. with larger bandwidths).

Having quantified the breaking threshold slope S_{tr}, the linear slope S_{Sinnes}, and the assumption that only a single wave breaks per wave group, the percentage of breaking is determined by dividing the total number of breaking wave groups by the total number of individual waves from the surface elevation time series recreated by the Gaussian wave groups. Table 5.1 shows the percentage of breaking waves per input significant wave height H_s. The values are in the same order as the theoretical prediction from chapter 4. However, the breaking percentages for the wave groups are smaller than the breaking percentages for the analysis of individual waves and smaller than the breaking percentages measured from the analysed trajectory data of the particles. This could potentially be the result of the assumption that only a single wave breaks per wave group with large linear slopes S_{Sinnes}.

Research has shown that wave breaking is affected by the wave group. Sutherland (1992) found that waves in a shorter group break at a lower height and Sinnis et al (2021) showed that the critical steepness is affected by the wave spectral shape. Thus, the breaking threshold for wave groups S_{tr} is scientifically more correct than the breaking threshold for individual waves by Duncan, because it takes into account the wave group characteristics. The values of the breaking threshold slope S_{tr} are in the range of 0.20 to 0.34, which corresponds to values found by Drazen et al. (2008) and Rapp & Melville (1990) where the onset of breaking wave groups was studied based on the experimental results of Sinnis et al..

Table 5.1 The percentage of breaking waves per input significant wave height H_s

H_s [cm]	$S_{Sinnes} - S_{tr} > 0$ [%]
5	0.00
9	1.01
13	3.15
17	5.90

5.4 Breaking model results

In this section, the results of the wave-breaking-induced transport are discussed. This is done, firstly, based on the transport of individual wave groups in different significant wave height conditions and, secondly, based on the enhancement factor. Thereafter, the sensitivity of the enhancement factor is analysed by varying the breaking threshold.

5.4.1 Discussing the wave-breaking-induced transport

The transport is calculated for breaking wave groups in four different input significant wave height conditions H_s = 5, 9, 13, 17 cm. Figure 5.5 show the transport for the breaking Gaussian wave groups in meters. H_s = 9 cm has 630 wave groups and H_s = 17 has 625 wave groups respectively. For the significant wave height case H_s = 17 cm, the linear slope S_{Sinnes} is larger because of the amplitude is larger, while the bandwidth remains approximately the same throughout the different experiments. As a result, the transport $\delta x_{\eta,br,g}$ is much larger and numerous for H_s = 17 compared to H_s = 9 cm.

Furthermore, in figure 5.5, there are two notable outcomes. In order to calculate the transport $\delta x_{\eta,br,g}$ in meters, the bandwidth Δ_{Sinnis} is in the denominator on the right hand side of (5.2). Therefore, smaller bandwidths (i.e. larger widths) of the wave groups increase the transport. Correspondingly, the red dots shown in figure 5.5 are from the small bandwidths, which have the

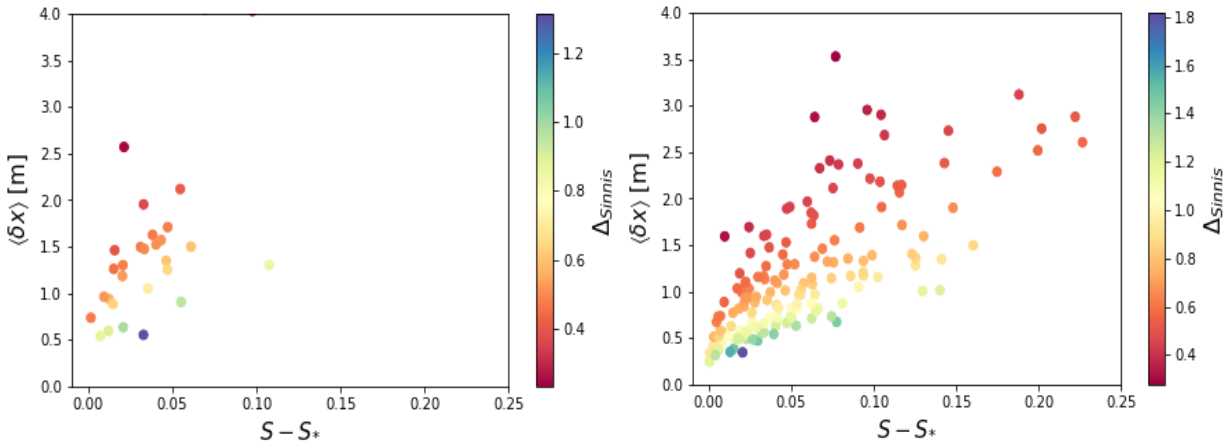

Figure 5.5 shows the transport $\langle\overline{\delta x}\rangle$ for individual wave groups as a function of the linear slope S minus the threshold slope S_* for H_s = 9 (left) and 17 cm (right), respectively.

largest transport $\delta x_{\eta,br,g}$. Additionally, the transport increases with increasing linear slope, which is also in agreement with (5.2). Because the transport of breaking wave groups is still an ongoing research, measurements for the transport of breaking waves with larger H_s have not been carried out. Therefore, the transport relationship from Sinnis et al. is extrapolated for $S - S_{tr}$. Sinnis defined larger values for $S - S_{tr}$ as plunging breakers. Plunging breakers exert more transport $\langle\delta x\rangle$ than spilling breakers. However, in this research, no plunging breakers were observed. Consequently, for large slopes and narrow bandwidths, the transport function (5.2) overestimates the transport. Because actually, these wave groups are not plunging breakers. With the current knowledge, however, this line is our best theoretical approximation.

5.4.2 Calculating the enhancement factor

To approximate how much the transport from the Stokes drift is enhanced by these breaking wave groups, a drift enhancement factor χ_η is calculated for each input significant wave height case H_s. In order to do this, the breaking-induced transport for the wave groups that exceed the threshold value ($S_{Sinnes} - S_{tr} > 0$) is computed and summed. Additionally, to remain consistent with the transport model of breaking waves also the transport for nonbreaking waves is computed using the approximated Gaussian wave spectrum. Hence, the Stokes transport is calculated from the Gaussian wave groups. The transport for non-breaking waves can also be calculated using the formulation defined by Sinnis et al., which simplified to: $\delta x = \beta/k_c\Delta$. However, this gives unrealistically high values for the Stokes drift, which is likely to be caused by the fact that Sinnis et al. found in their experimental study values for the Stokes drift of wave groups near their breaking threshold and thus for very non-linear waves. Another formulation is used to calculate the transport for non-breaking waves. First, the kinematics of the wave groups is assumed to have no dispersion to simplify the calculation of the Stokes transport. Fundamentally, as time progresses the wave group becomes wider in space due to dispersion. However, van den Bremer & Taylor (2015) showed that leading-order frequency dispersion does not affect the Stokes drift velocities. Therefore, the formulation by van den Bremer and Taylor (2015) is used to calculate the Stokes transport $\delta x_{s,\eta,g}$ of the wave groups without dispersion:

$$\delta x_{s,\eta,g} = 2\sqrt{\pi}\sigma_{Gaussian}\alpha^2 \ , \tag{5.15}$$

where $\sigma_{Gaussian}$ is the length scale of the Gaussian wave group and $\alpha = k_0|A_0|$ is the steepness of the wave group, where k_0 denotes the wavenumber of the carrier wave and $|A_0|$ is the magnitude (of the leading-order component in bandwidth) of the complex envelope of the surface elevation (i.e. the

maximum value of the Gaussian envelope $\eta_{G,env}(t)$ for a specific wave group). The Stokes transport is calculated for all wave groups. Subsequently, the drift enhancement factor χ_η is calculated by:

$$\chi_\eta = \frac{\Sigma\delta x_{s,\eta,g} + \Sigma\delta x_{\eta,br,g}}{\Sigma\delta x_{s,\eta,g}} , \tag{5.16}$$

where $\Sigma\delta x_{s,\eta,g}$ is the Stokes drift and $\delta x_{\eta,br,g}$ is the breaking-induced drift. The values for χ_η are shown in table 5.2. For H_s = 5 cm no breaking waves are identified by the model. Thus, the enhancement factor is 1. When the input significant wave height increases, the enhancement factor takes on a visually observed linear trend. The drift due to breaking is enhanced up to 1.76 times the Stokes transport for H_s = 17 cm. However, this enhancement factor takes into account all breaking waves. Therefore, when comparing the drift enhancement factor χ_η with the number of breaking waves derived from the trajectories of the particles in the Deltares experiment a probability factor should be taken into account. Otherwise, the drift enhancement factor overestimates the enhanced experimental drift. This probability factor is related to the average number of breaking waves encountered by the particles.

Table 5.2 the Stokes drift from the truncated frequency spectrum $u_{st,\eta,3.5f_0}$, duration of the experiment T_{exp}, the total summed transport from breaking wave groups $\Sigma\langle\overline{\delta x_{br}}\rangle$, and the drift enhancement factor χ_η per input significant wave height H_s.

H_s [cm]	Wave groups [#]	$\Sigma\delta x_{s,\eta,g}$ [m]	$\Sigma\delta x_{\eta,br,g}$ [m]	χ_η
5	660	44.31	0.00	1.00
9	630	125.03	42.05	1.32
13	421	116.74	52.54	1.45
17	625	290.92	216.86	1.76

5.4.3 Sensitivity of the enhancement factor

In this section, the sensitivity of the enhancement factor is examined based on the parameters of the theoretical model discussed in section 6.2. The parameters analysed are the breaking threshold, the relative width of the Gaussian wave groups, and the number of wave groups taken into account for the calculation of the enhancement factor.

First, the breaking threshold is varied. The breaking threshold is a function of the spectral bandwidth. Therefore, the variation of the threshold is based on the relationship between the Gaussian bandwidth and the spectral bandwidth discussed in section 6.3.1.1. The values of the bandwidth that determine the relationship have a maximum deviation of 0.01 from the linear best fit. Therefore, the calculated bandwidths are increased ad decreased by 0.01 for the variation of the threshold. The maximum deviation of the enhancement factor is in the order of 2%.

Secondly, the relative width of the Gaussian wave groups is varied. The relative width strongly influences the spectral bandwidth. Thus the variation is expected to be significant. In order to keep a realistic value for the bandwidth, the variation of the relative width is based on the energy of the total measured surface elevation spectrum and the approximated Gaussian spectrum. The deviation of the energy should not be more than 10%. This corresponds approximately to a deviation of 0.5 for the relative width. The maximum deviation of the enhancement factor is in the order of 7%. lastly, the threshold for which wave groups are identified is varied. The value used for the initial calculation is equal to $0.1H_s$. This value is varied between the mean water level and $0.2H_s$. The maximum deviation of the enhancement factor is in the order of 1%. Summing the total deviation gives a value of 10%. The total error margin is plotted in figure 5.6.

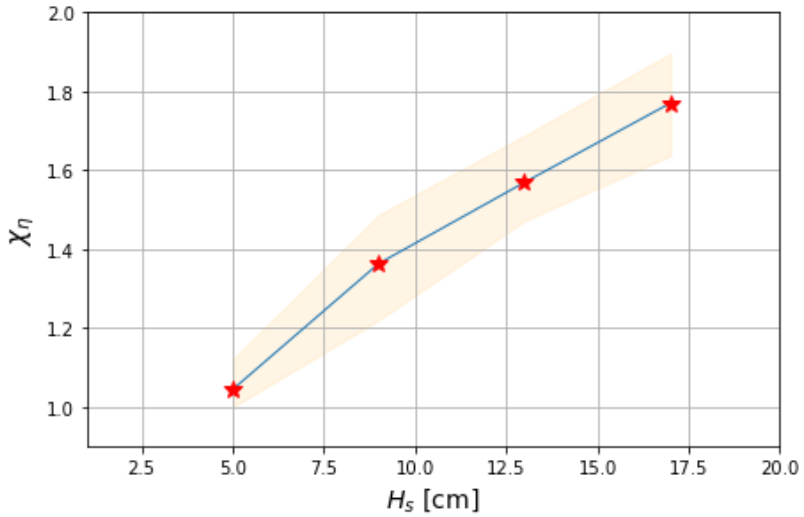

Figure 5.6 Enhancement factor χ_η per input significant wave height H_s condition with the maximum error margin

6

Discussion of the results

The objective of this paper is to quantify the contribution of breaking waves to the wave-induced Lagrangian drift at the surface of a deep-water unidirectional random sea. To do this, I introduced a drift enhancement factor $\chi_\eta = (\Sigma\delta x_{s,\eta,g} + \Sigma\langle\overline{\delta x}\rangle_{\eta,br,g})/\Sigma\delta x_{s,\eta,g}$, where $\Sigma\delta x_{s,\eta,g}$ is the transport induced by the Stokes drift and $\langle\overline{\delta x}\rangle_{\eta,br,g}$ is the transport from breaking waves. The enhancement factor quantifies how much the Stokes transport of perfectly Lagrangian tracers in a wave field without an Eulerian flow is enhanced by breaking waves. In chapters 4 and 5, I determined the enhancement factor for the experimental data and the theoretical model, respectively. In this chapter, the accuracy and limitations of the model are described. This is done by comparing the number of breaking waves, the wave-breaking-induced transport, and the enhancement factors of the experimental and model results.

6.1 Comparing the theoretical model predictions to the experimental results

In this section, the theoretical model and experimental results are evaluated. First, the number of breaking events is discussed. Secondly, the wave-breaking-induced transport, and lastly the enhancement factor. Arguments are given explaining the deviations in theoretical and model results.

6.1.1 Number of breaking events

The percentages of breaking waves in the experimental data and theoretical model results are presented in Table 6.1 which shows that the breaking percentages from the theoretical model are smaller than the breaking percentages measured in the trajectories of the particles. In this paragraph, possible explanations are given for this observation. First of all, the principle difference is the measurement approach. Identification of breaking waves in the theoretical model occurred at a fixed location (Eulerian) using the wave gauges, while in the experiment, the breaking waves were identified in the trajectories of Lagrangian particles. Consequently, the principle difference is that the particles in the experiment also encounter contact events of breaking waves. The theoretical model, on the contrary, defines breaking waves based on the geometry of a wave group at a fixed location. Therefore, breaking only occurs when a steepness threshold is exceeded implying large breaking events and thus no contact events. Additionally, the wave spectrum for irregular waves is continuously changing, a wave that is not identified as a breaking wave at the location of the wave gauge might evolve into a breaking wave when encountering a particle. Besides, the particles are distributed over the whole region of interest in the Atlantic basin. Therefore, the probability that a particle encounters a breaking event is larger than for the wave gauge.

Besides, the breaking threshold of the theoretical model for the wave groups S_{tr} is derived and validated based on wave groups generated by a dispersive focusing technique. Rapp & Melville (1990) found that incipient wave breaking due to dispersive focusing can occur at a much lower wave steepness, depending on the bandwidth of the wave group. The breaking threshold for the experimental data ϵ_{tr} is dependent on research by Duncan (1981) who did not take into account the bandwidth. Hence, the threshold for the theoretical model S_{tr} is lower leading the more breaking events. This is not necessarily a problem, as discussed in chapter 4.2, other hydrodynamics in the tank

Table 6.1 The breaking percentages from the theoretical model and from the experimental results

H_s [cm]	Breaking waves in experiment [%]	Breaking waves in theoretical model [%]
5	0.14	0.00
9	2.24	1.01
13	5.25	3.15
17	8.15	5.90

like the opposing current were present, which were compensated for by decreasing the threshold for breaking waves in the experiment ϵ_{tr}. The hydrodynamics were not taken into account in the threshold from the theoretical model S_{tr}.

Furthermore, research has shown that wave breaking is affected by wave group characteristics. Sutherland (1992) found that waves in a shorter group break at a lower height and Sinnis et al (2021) showed that the critical steepness is affected by the spectral shape of the wave group. Thus, the breaking threshold for wave groups S_{tr} is scientifically more complete than the breaking threshold for individual waves by Duncan. The values of the breaking threshold slope S_{tr} are in the range of 0.20 to 0.34, which corresponds to values found by Drazen et al. (2008) and Rapp & Melville (1990) where the onset of breaking wave groups was studied based on experimental results

Lastly, in the theoretical model, it was assumed that only a single wave breaks in a breaking wave group. However, observations have shown that wave groups with large steepness may have multiple breaking waves in a single wave group (Wang & Wijesekera, 2018). Therefore, this assumption also contributes to a smaller number of breaking waves for the theoretical model.

6.1.2 Wave breaking induced transport

In this section, the wave-breaking-induced transport from the theoretical model and the experimental results are compared. This is done by discussing the strength of the breaking events in significant wave height conditions H_s = 9 and 17 cm. Figure 6.1a and b show the wave-breaking-induced transport for individual wave groups from the theoretical model. Figure 6.1c and d show the histograms of the wave-breaking-induced transport encountered by individual particles during the experiment. On the x-axis, the wave-breaking-induced transport is shown. The results show that for both significant wave height cases, the values for the wave-breaking-induced transport are in the same range. This indicates that the theoretical model is able to calculate the strength of the breaking events.

Some differences can be observed. The experimental results in H_s = 9 cm show more values for the breaking-induced transport below 0.5 m, while the theoretical model in H_s = 9 cm does not show transport values below 0.5 m. The reason for this is contact events, which are measured by the particles in the experiment and are not measured by the wave gauge and consequently also not by the theoretical model. Furthermore, the largest values of the transport from the theoretical model in H_s = 9 cm appear in the range of 1.9 to 2.6 m, while the largest transport value measured by the particles is 1.5. Hence, the transport of the maximum outlier from the theoretical model is more than 1 m larger compared to the maximum transport value from the experimental results. As can be seen in Figure 6.1b, the outlier corresponds to the smallest value of the spectral bandwidth. Therefore, it is likely that the theoretical model has overestimated the width of the Gaussian wave group.

Furthermore, H_s = 17 cm has many breaking-induced transport values below 0.6 m, while the breaking-induced transport from the particles from the experiment has none. The spectral bandwidth is likely the cause of this large number of small transport values for the theoretical model. Because H_s = 13 cm and H_s = 17 cm did not have active reflection compensation, waves were reflected back from the beach and the wave paddle resulting in a lot of disturbances of the envelope of the surface elevation

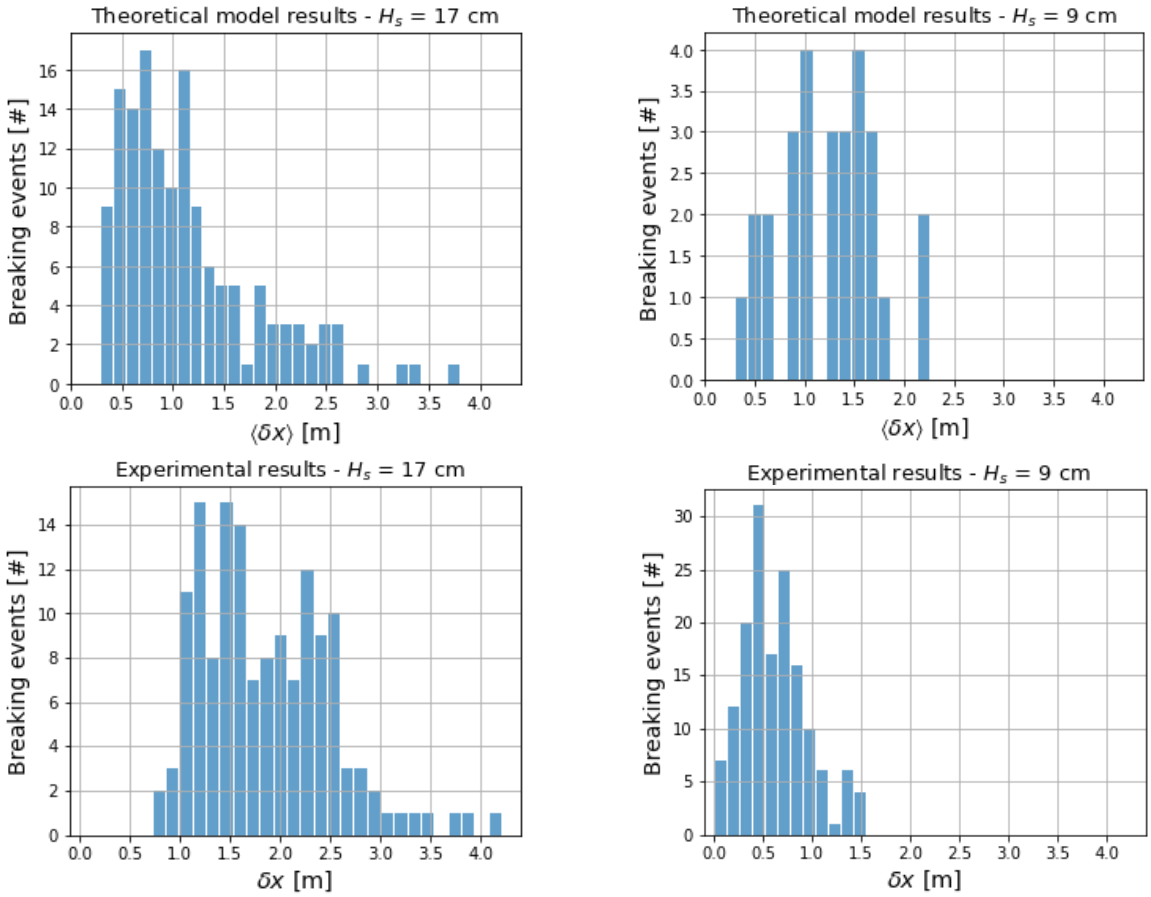

figure 6.1 The upper graphs show the transport of breaking waves from the theoretical model and the lower histograms show the transport of of breaking waves from the experimental results.

spectrum from which the width of the Gaussian wave group is determined. Due to the large amount of undulations in the envelope the width of the wave group is much more difficult to define accurately. Therefore, the width of the wave groups is likely taken too small, which results in smaller values for the breaking-induced transport and lower threshold values S_{tr} for the theoretical model, which is related to the spectral bandwidth.

6.1.3 Enhancement factor

We have seen that the theoretical model is capable of calculating the right order of magnitude for the transport of breaking wave groups. Additionally, the number of breaking events between the theoretical prediction and the experimental analysis also shows similar results. In this section, the enhancement factor is evaluated. The enhancement factor of the particles is based on the breaking and non-breaking transport identified from their trajectories and the enhancement factor of the theoretical model is calculated based on the transport of the breaking and non-breaking wave groups and as is discussed in chapters 4 and 5, respectively. The results are shown in Figure 6.1. The enhancement factor of the theoretical model appears to over-predict compared to the values of the experiment. The main reason for this is that the theoretical model calculates the transport of the whole wave breaking front whereas the experimental merely contact events are taken into account with much smaller transport. However, the mean values of the enhancement factors are close to each other, follow a similar linear trend, and have a significant amount of overlap regarding the margins from the sensitivity analysis.

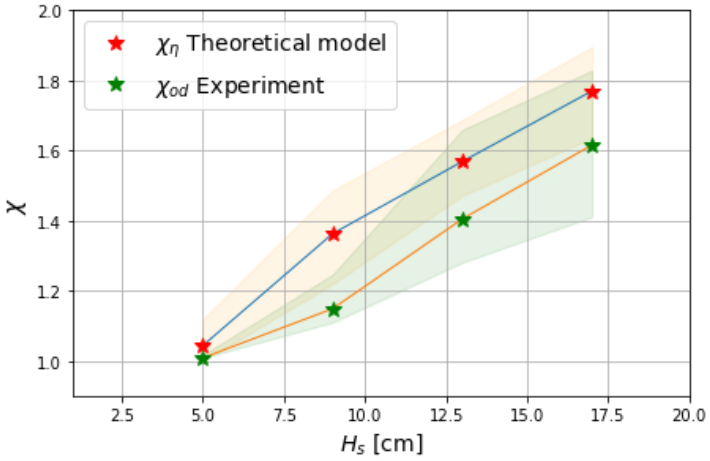

Figure 6.1 The enhancement factors of the theoretical model and the experimental results with their error margins.

6.2 Discussion on the accuracy of the theoretical model

Based on the comparison of the breaking probability, the breaking-induced transport, and the enhancement factor, it is discussed whether the theoretical model can predict the wave-breaking-induced drift or whether the uncertainties remain too large.

6.2.1 Uncertainties of the theoretical model

As discussed in section 5.4.2, the main contributors to the uncertainty are the definition of the relative width, the breaking threshold, and the number of wave groups taken into account. The sensitivity of these parameters was analysed and it was found that the breaking threshold and the number of wave groups only had limited influence on the sensitivity of the enhancement factor. The main uncertainty of the theoretical model is the relative width of the Gaussian wave group. The relative width of the Gaussian wave group was chosen for which the total energy of the approximated surface elevation time series was equal to the energy of the measured surface elevation times series. Thus, the relative width of the Gaussian wave group has a significant contribution to the total energy of the approximated surface elevation spectrum and also to the spectral bandwidth of the wave group. The spectral bandwidth has a large contribution in calculating the transport. Because the envelope of the wave groups in irregular waves shows undulations, the exact width of the wave group is not always taken into account. For example, when a wave group contains a wave with a large amplitude then the model assumes the relative width is only related to the width of this one wave. Consequently, the spectral bandwidth which is calculated from the relative width can show deviations. However, this is expected to have occurred to a very minimal extent.

6.2.2 Limitations of the theoretical model

The main limitation of the theoretical model is being unable to determine the relative width of the wave groups with high accuracy. In the theoretical model, all wave groups have the same relative bandwidth (this does not mean that the width of all wave groups is equal), which was determined based on the energy of the measured and approximated surface elevation. However, each wave group has its own specific amount of energy. Therefore, it would be better to tune the relative width of the Gaussian wave group based on the energy of the measured wave group that it represents instead of comparing the energy of the whole spectrum as is done in this research. Additionally, the calculated transport from the theoretical model is based on the parameters for wave groups. When waves travel to shallow water, other types of breaking waves occur such as surging and plunging breakers. The theoretical model, however, is limited to spilling breakers. Hence, the transport function is limited to deep water waves where mostly spilling breakers occur.

6.3 Limitations of the theoretical model in a realistic sea

In this section, I will argue what the limitations are of the theoretical model in oceanic wave conditions. The principle limitation is the threshold for breaking waves, which is determined based on the geometry of a wave or wave group. In the ocean, however, other factors also play a role that can initiate wave breaking. Factors responsible for wave breaking are the friction velocity depending on the wind speed and currents, which are not taken into account in the theoretical model. Besides, in this study, I have considered long-crested or unidirectional waves. In the ocean, short-crested or directionally spread sea states are common. Therefore, capturing wave groups using a Eulerian approach is more challenging because of the highly dynamic nature of the surface elevation. Therefore, the theoretical model could not be used to highly irregular directional wave field as the wave group are hard to define.

7

Conclusion and recommendations

7.1 Conclusion

This thesis focused on determining the enhancement of the Stokes transport at the surface of a unidirectional random sea by breaking waves. To do this, an enhancement factor was calculated $\chi = (\Sigma\delta x_s + \Sigma\delta x_{br})/\Sigma\delta x_s$ based on the total Stokes transport $\Sigma\delta x_s$ and the total breaking-induced transport $\Sigma\delta x_{br}$ from measured surface elevation data and trajectories of Lagrangian particles. This enhancement factor was calculated from experimental results and complemented by a theoretical model. Three sub-questions were formulated to reach this goal, which are evaluated in this conclusion.

The first evaluated sub-question discussed whether the wave-breaking-induced drift can be determined from experimental data. During the experiment, particles were released in the Atlantic basin of Deltares, wherein a unidirectional random sea with breaking waves, non-breaking waves, and Eulerian current were present. The particles were filmed in the area of interest using an overhead camera and tracked using OpenCV, an open-source computer vision library in Python. The trajectories were undistorted and translated to real-world coordinates. From the trajectories of the particles, the breaking waves were identified based on a velocity threshold. The velocity threshold is more than two times larger than the average Stokes drift of the corresponding wave field, as discussed in paragraph 4.3.2. The sensitivity of this threshold was evaluated in paragraph 4.4.3, which showed that the enhancement factor had a maximum deviation of 12% from the mean. The deviation increased for wave fields with larger significant wave heights H_s. Particles do not always travel the whole wave breaking front, but merely encounter contact events. Larger number of breaking waves resulted in more contact events and hence more velocities around the breaking threshold. Therefore, the sensitivity is larger for wave fields with many breaking events. Nonetheless, considering the large variability in the breaking waves in the field, a maximum deviation of 12% is reasonable for an estimate of the breaking-induced enhanced surface transport. Lastly, the wave fields with H_s = 5, 9, 13, and 17 cm showed values for the enhancement factor of χ = 1.01, 1.22, 1.45, and 1.65, respectively. Hence, almost no enhancement of Stokes-induced surface transport for wave fields without breaking (i.e. low H_s case) and an almost linear increase in the enhancement factor when H_s increases.

The second sub-question discussed whether a model can be defined to determine the wave-breaking-induced drift. To do this, the breaking transport relationship from Sinnis et al. (2021) was used. In their research, they quantified the surface transport of isolated breaking wave groups in deep water based on the spectral bandwidth and linear slope. In this research, the relationship from Sinnis et al. was applied to wave groups of a unidirectional random sea by approximating the measured surface elevation spectrum by Gaussian wave groups as explained in chapter 5. The Gaussian wave groups allowed for the determination of the input parameters of the theoretical model. Consequently, the transport of the breaking and non-breaking wave groups could be calculated. The parameters of the theoretical model with the largest influence on the transport are the breaking threshold slope, linear slope, and the spectral bandwidth. The linear slope could be obtained accurately, while for the spectral bandwidth and the breaking threshold slope, which is a function of the spectral bandwidth, uncertainty

remains. A sensitivity analysis was performed in section 5.4.2, which showed that the maximum deviation of the enhancement factor caused by the spectral bandwidth and the breaking threshold slope was 7% and 2% from the mean, respectively, which is considered reasonable regarding the simplicity of the model. The wave fields with H_s = 5, 9, 13, and 17 cm showed values for the enhancement factor of χ = 1.00, 1.32, 1.45, and 1.76, respectively.

The third sub-question discussed how accurate the model results were compared to the experimental results. This was evaluated in chapter 6 by comparing the model and theoretical results. The number of breaking events, the wave-breaking-induced transport, and the enhancement factor appeared to be in the same order of magnitude for both the experimental and theoretical model results. Primarily, the values of the enhancement factor have significant overlap. Hence, the comparison showed that the model results are reasonably accurate. The min uncertainty of the model, however, is the width of the wave groups, for which the definition remains arbitrary. Nonetheless, the width of the wave groups does have a large contribution to the results of the theoretical model and therefore requires validation by using a more accurate method in defining the width. However, the transport of the theoretical model and the experimental results is in the right order of magnitude indicating that the width of the wave group was reasonably accurate.

The main question of this research was to what extent the contribution of wave-breaking-induced drift to the wave-induced Lagrangian drift at the surface of a unidirectional random sea could be quantified. First of all, it was possible to obtain the number of breaking events and the wave-breaking-induced transport from the experimental results and from the corresponding surface elevation time series using the theoretical model. Furthermore, it was concluded that the sensitivity of the parameters remains within acceptable margins. Therefore, the results of the enhancement factor determined by the model and experiments gave a reasonable approximation of the enhanced surface drift due to breaking waves. Hence, I believe that this framework can be fruitful grounds for further extensions.

7.2 Recommendations

In this section, recommendations are given for the experimental analysis and the theoretical model. First, improvements are proposed to enhance the accuracy of the theoretical model. Subsequently, possible extensions are described on how the model could be more representative of a real sea state. Lastly, recommendations are given on how a similar experiment could give more accurate results.

7.2.1 Improving the accuracy of the theoretical model

The main uncertainty of the theoretical model lies in the definition of the width of the Gaussian wave groups, which has a large influence on the transport of breaking wave groups in deep water. The current method for the width of the wave groups could be validated or improved using the Hilbert-Hueng transform. The Hilbert-Hueng transform takes into account the energy of individual wave groups for the definition of the width. Hence, using this method the Gaussian approximation of the width of the wave groups can be optimized and validated. Because of time this method was not used in this research.

7.2.2 Improving the experimental results

Tracking particles in the video footage from the experiment was challenging for two reasons. The first reason is the distance of the camera from the area of interest. The distance was 11.9 meters above the area of interest, filming particles with a diameter of 20 mm. Therefore, the spheres appeared very small in the video footage making it difficult for the CSRT tracker to keep track of the particles during breaking events. Besides, when particles were too close to each other and collisions occurred, the CSRT tracker could lose the particle it was tracking and move to another particle giving inaccurate results.

Therefore, to improve the experimental results it is recommended to spread the particles more over the area of interest so no collision of particles will occur and the distance of the camera to the area of interest should be smaller.

Furthermore, the pump-induced current is a large contributor to the drift of the particles in the experimental results and the geometry of the waves. However, because measurements were only performed at a single location and at three different depths over the vertical a good estimation of the flow profile over the vertical was not able to be determined. Hence, for further experimental campaigns, the electromagnetic velocity meters should be more numerous over the depth to get a good idea of the velocity profile.

Additionally, to get more accurate results, the background motion and the motion due to the subharmonic error wave had to be eliminated from the trajectories. As a result, the Stokes transport could be defined more accurately. Careful consideration of the error wave through fitting methods on the mean flow will then be necessary to remove eliminate the subharmonic error wave as described in Calvert et al. (2019).

7.2.3 Extending the theoretical model

The wave spectrum of a real sea is not unidirectional but multidirectional. In the ocean, short-crested or directionally spread sea states are common. The theoretical model could be extended by taking into account the directionality of the wave spectrum. Subsequently, the model could be applied to a directional spectrum of a real sea in controlled conditions. The Delta basin of Deltares could be suitable for such an experimental campaign. From the experimental results, a relationship can be established between the significant wave height input conditions and the resulting Stokes drift enhancement factor in directional irregular seas.

To extend the model even further and improve the predictability of flotsam and jetsam with different sizes and densities, research should be conducted for non-Lagrangian tracers in breaking and non-breaking waves. An enhancement factor could be related to the Stokes transport and the enhanced drift caused by the inertia of different shapes and densities in breaking and non-breaking waves.

Both the enhancement factor for breaking-induced transport and the enhancement factor for the shape and density of an object can be incorporated in a model with multiple ocean processes like current and wind-induced friction. The model accuracy can be validated by dropping buoys at a certain location where measurements of the ocean conditions are available.

References

Andrady, A. (2011). Microplastics in the marine environment. *Marine Pollution Bulletin, 62*, 1596-1605.

Banner, M. L., & Peregrine, D. (1993). Wave breaking in deep water. *Annual Review of Fluid Mechanisc 25.1*, 373-397.

Battjes, J., & van Vledder, G. (1984). Verification of Kimura's theory for wave group statistics. *Coastal Engineering Proceedings 1*.

Brown, A., Thomson, J., Ellenson, A., Rollano, F., Özkan-Haller, & Haller, M. (2019). *Kinematics and Statistics of Breaking Waves Observed Using SWIFT Buoys.* IEEE Journal of Oceanic Engineering.

Calvert, R., Whittaker, C., Raby, A., Tayler, P., Borthwick, A., & van den Bremer, T. (2019). Laboratory study of the wave-induced mean flow and set-down in unidirectional surface gravity wave packets on finite water depth. *PHYSICAL REVIEW FLUIDS 4*, 114801.

Cerna, M., & Harvey, A. F. (2000). *The Fundamentals of FFT-Based Signal Analysis and Measurement* . Austin: National Instruments Corporation.

Chen, H., & Zou, Q. (2022). Geometry of deep and intermediate water breaking waves influenced by wind speed and direction. *Physics of Fluids, 34*.

Dardagan, N., Brdanin, A., Dzigal, D., & Akagic, A. (2021). *Multiple Object Trackers in OpenCV: A Benchmark.* IEEE .

Doeleman, M. W. (2019). *Rogue waves in the Dutch North Sea.* Delft: TU Delft.

Drazen, D., Melville, W., & Lenain, L. (2008). Inertial scaling of dissipation in unsteady breaking waves. *Journal of Fluid Mechanics*, 307-332.

Duncan, J. H. (1981). An experimental investigation of breaking waves produced by a towed hydrofoil. *Proc. R. Soc. Lond. A377*, 331–348.

Eliasson, B., & Haas, F. (2014). *Trapping and instability of directional gravity waves in localized water currents.*

Funke, E., & Mansard, E. (1979). *On the synthesis of realistic Sea States in a laboratory flume.* National Research Council of Canada.

Goda, Y. (1970). A synthesis of breaker indices. *Proceedings of the Japan Society of Civil Engineers, 2*, 227-230.

Holthuijsen, L. (2007). *Waves in Oceanic and Coastal Waters.* Cambridge University Press.

Huang, W., & Dong, S. (2021). Statistical description of wave groups in three types of sea states. *Ocean Engineering*.

Lenain, L., Pizzo, N., & Melville, K. (2019). *Laboratory studies of Lagrangian transport by breaking surface waves.* Cambridge University Press.

Lermusiaux, P. F., Doshi, M., Kulkarni, C. S., Gupta, A., Haley, P. J., Mirabito, C., . . . Noble, C. (2019). Plastic Pollution in the Coastal Oceans: Characterization and Modeling. *OCEANS 2019 MTS/IEEE SEATTLE*, 1-10.

Lewis, T., & Barnett, V. (1984). *Outliers in Statistical Data 2nd edn.* New York: John Wiley.

Liubartseva, S., Coppini, G., Lecci, E., & Clementi, E. (2018). *Tracking plastics in the Mediterranean: 2D Lagrangian model.* Bologna: Marine Polution Bulletin.

Mansui, J., Molcard, A., & Ourmieres, Y. (2015). *Modelling the transport and accumulation of floating marine debris in the Mediterranean basin.* Toulon: Marine Pollution Bulletin.

Monismith, S. (2020). Stokes drift: Theory and experiments. *Journal of Fluid Mechanics, 884*.

Olabarrieta, M., Medina, R., & Castanedo, S. (2010). *Effects of wave–current interaction on the current profile.* Coastal Engineering.

Olbers, D., Willebrand, J., & Eden, C. (2012). *Lagrangian Theory of Ocean Waves.* Berlin, Heidelberg: Springer.

Parker, L. (2019, 05 27). *The world's plastic pollution crisis explained*. Retrieved from nationalgeographic: https://www.nationalgeographic.com/environment/article/plastic-pollution

Phillips, O., & Banner, M. (1974). Wave breaking in the presence of wind drift and swell. *Journal of Fluid Mechanics, 66*, 625-640.

Pizzo, N., & Melville, W. (2019). Focusing deep-water surface gravity wave packets: wave breaking criterion in a simplified model. *Journal of Fluid Mechanics. 873.*, 238-259.

Pizzo, N., Melville, K. K., & Deike, L. (2019). *Lagrangian Transport by Nonbreaking and Breaking Deep-Water Wave at the Ocean Surface.* Journal of Physical Oceanography.

Pizzo, N., Murray, E., Llewellyn Smith, D., & Lenain, L. (2021). The role of bandwidth in setting the breaking slope threshold of deep-water focusing wave packets. *Physics of Fluids 33*.

Popat, N. R. (1989). *Steep capillary waves on gravity waves.* Bristol: The University of Bristol.

Rafiuddin Ahmed, M., Faizal, M., Prasad, K., Cho, Y., Kim, C., & Lee, Y. (2010). Exploiting the orbital motion of water particles for energy extraction from waves. *Journal of Mechanical Science and Technology*, 943-949.

Rapp, R. J., & Melville, W. (1990). Laboratory measurements of deep-water breaking waves. *Philosophical Transactions of the Royal Society of London. Series A, Mathematical and Physical Sciences 331*, 735–800.

Rye, H. (1982). *Ocean wave groups.* Norway: Department of Marine Technology .

Schnurr, R., Alboiu, V., Chaudhary, M., Corbett, R., & Quanz, M. (2018). Reducing marine pollution from single-use plastics (SUPs): A review. *Marine Pollution Bulletin Volume 137*, 157-171.

Sinnis, J. T., Grare, L., Lenain, L., & Pizzo, N. (2021). Laboratory studies of the role of bandwidth in surface transport and energy dissipation of deep-water breaking waves. *Journal of Fluid Mechanics*, 927.

Stansell, P., & MacFarlane, C. (2002). Experimental investigation of wave breaking criteria based on wave phase speeds. *Journal of Physical Oceanography 32*, 1269-1283.

Stokes, G. (1847). On the Theory of Oscillatory Waves. *Transactions of the Cambridge Philosophical Society*, 441-455.

Sukhodolov, A., Nikora, V., & Katolikov, V. (2011). Flow dynamics in alluvial channels: The legacy of Kirill V. Grishanin. *Journal of Hydraulic Research. 49.*, 285-292.

Sutherland, J. (1992). *The Dynamics of non-linear wave groups.* UK: The University of Edinburgh.

van den Bremer, T., & Breivik, O. (2017). *Stokes drift.* The Royal Society Publishing.

van den Bremer, T., & Taylor, P. (2015). Estimates of Lagrangian transport by surface gravity wave groups: The effects of finite depth and directionality: Lagrangian transport by wave groups. *Journal of Geophysical Research: Oceans. 120*, 2701-2722.

van Sebille, E., Kaandorp, M., & Dijkstra, H. (2020). *Closing the Mediterranean Marine Floating Plastic Mass Budget: Inverse Modeling of Sources and Sinks.* Environmental Science and Technology.

Wang, J., Zhi, T., Peng, J., Qiu, Q., & Li, M. (2016). The behaviors of microplastics in the marine environment. *Marine Environmental Research Volume 113*, 7-17.

Wang, W. D., & Wijesekera, W. H. (2018). Observations of Breaking Waves and Energy Dissipation in Modulated Wave Groups. *Journal of Physical Oceanography, 48*, 2937–2948.

Welden, N., & Lusher, A. (2017). Impacts of Changing Ocean Circulation on the Distribution of Marine Microplastic Litter. *Integrated Environmental Assessment and Management, 13*, 483-487.

Wichmann, D., Delandmeter, P., & van Sebille, E. (2019). *Influence of Near-Surface Currents on the Global Dispersal of Marine Microplastic.* Utrecht: JGR Oceans.

Appendix A Object tracker selection

A total of seven trackers are available from the OpenCV package. Each tracker is programmed to track a single sphere to determine which performs the task of tracking the yellow sphere best. Figure A1 shows the result of the tracking process with the regions of interest of the trackers in different colours. As can be seen, only the Boosting tracker and the CSRT tracker perform best. However, in the performance test, only a single object is tracked. During the experiment almost 300 spheres need to be tracked at once. Booster is not capable of tracking this number of spheres (Dardagan, Brdanin, Dzigal, & Akagic, 2021). Hence, the CSRT tracker is used for the analysis.

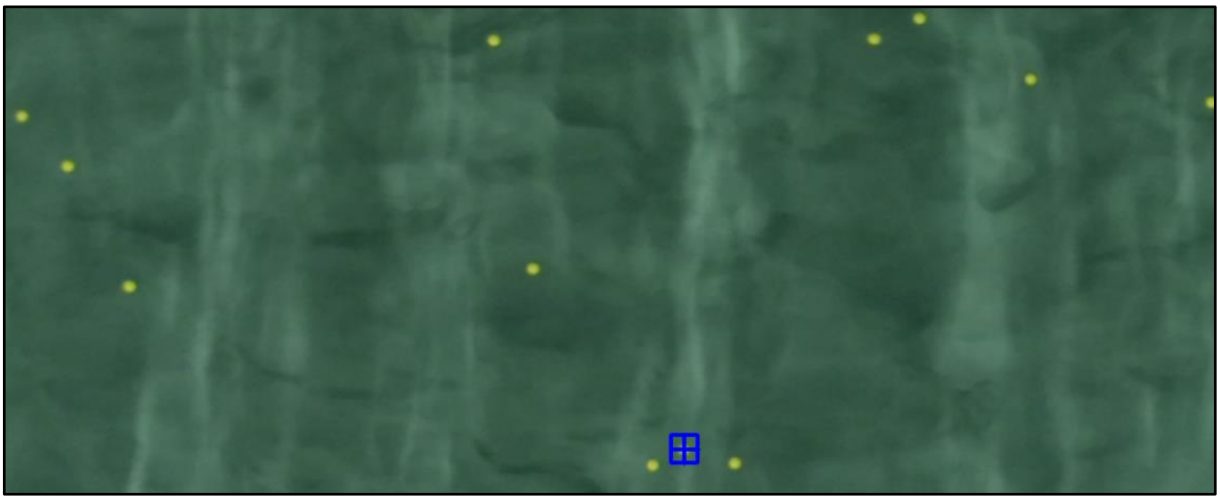

Figure 1 Selection area in blue for the trackers

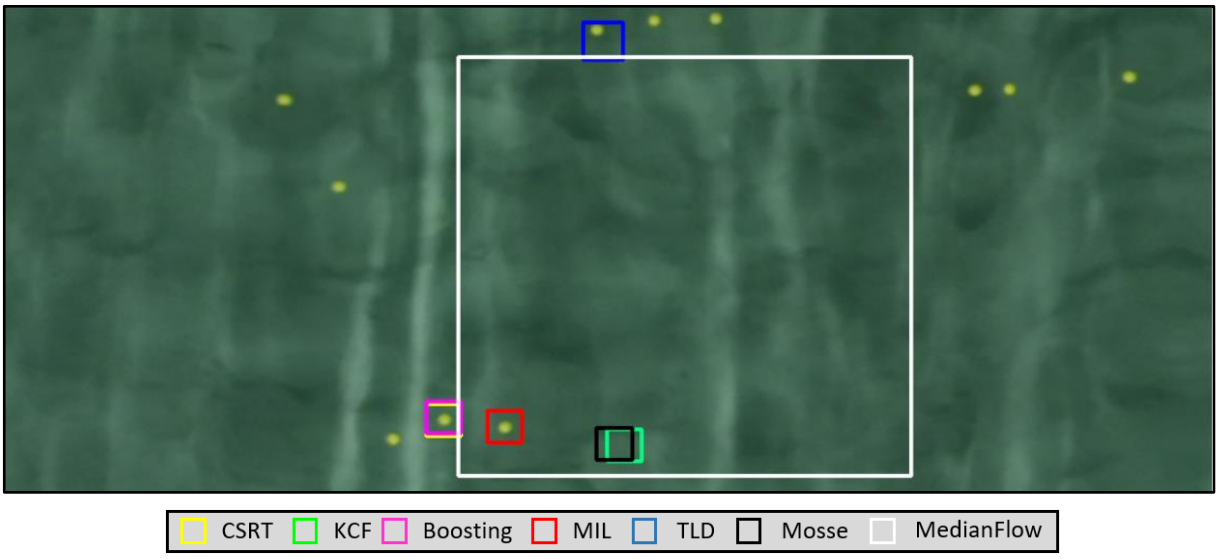

Figure A1 Performance of the trackers

Additionally, it is researched how the CSRT tracker deals with the challenges during the data extraction. The challenges that are encountered during the analysis are that the objects need to maintain its identity over all subsequent frames. Besides, the objects encounter intra-object occlusions resulting in the trackers jumping from one sphere to another, and lastly, during breaking the colour and shape of the spheres change resulting in the tracker losing the object.

The CSRT tracker is most capable of handling these challenges as the tracker uses a state-of-the-art tracking algorithm to recognize the objects efficiently. The spatial reliability map enables an arbitrary search region to mainly focus on the object and less on the background. Additionally, the reliability is

estimated from the properties of the constrained least-squares solution. To cope with changes in shape and dimension of moving objects regularized correlation filters are used. These filters keep into consideration the background and try to suppress it by assigning weights to the filter coefficients related to the object's location. Hence, based on the challenges posed by the experimental data the CSRT tracking method handles the complications best.

Appendix B Length scale derivation

In order to transform the standard deviation of the Gaussian distribution from a time scale to a length scale, the time domain of the wave group needs to be transformed to a length domain. To do this a relationship between Δt and Δx needs is established using the wave group velocity c_g. Multiplying Δt with c_g result in Δx. The group velocity for deep water waves is defined as:

$$\frac{\Delta k}{\Delta \omega} = \frac{1}{2} c = c_g \tag{B.1}$$

Where Δk is the wavenumber of the wave group, $\Delta \omega$ is the radian frequency of the wave group, and c is the phase velocity, which can be calculated using the derivative of the dispersion relation for deep water waves:

$$\omega_0 = \sqrt{gk} \tag{B.2}$$

$$k = \frac{\omega_0^2}{g} \tag{B.3}$$

$$\frac{dk}{d\omega_0} = \frac{2\omega_0}{g} = c \tag{B.4}$$

Where $k = 2\pi/L$ and $\omega = 2\pi/T$, with L the wave length and T the wave period. Substituting equation B.4 into equation B.1 we find the relationship between Δt and Δx:

$$\frac{\Delta k}{\Delta \omega} = \frac{1}{2} \frac{dk}{d\omega_0} \tag{B.5}$$

$$\frac{\Delta k}{\Delta \omega} = \frac{\omega_0}{g} \tag{B.6}$$

$$\Delta k = \frac{\omega_0}{g} \Delta \omega \tag{B.7}$$

$$\Delta k = \frac{\omega_0}{g} \Delta \omega \tag{B.8}$$

$$\Delta x = \frac{g}{\omega_0} \Delta t \tag{B.9}$$

$$\Delta x = c \Delta t \tag{B.10}$$

$$\Delta x = 2 c_g \Delta t \tag{B.11}$$

Hence, In order to calculate the length scale σ of the Gaussian wave groups, the time scale of the standard deviation from the Gaussian distribution needs to be multiplied by 2 times the group velocity c_g.

Appendix C Relating the Gaussian and Sinnis wave group characteristics

In this appendix, the wave groups from Sinnis' experiment are recreated and discussed. From these wave groups the relationships for the Gaussian and Sinnis bandwidth and linear slope are derived. First, the bandwidth is discussed. The bandwidth formulated by Sinnis for the wave groups cannot be applied to the wave groups from the Deltares experiment, because Sinnis assumes an uniform distributed energy spectrum, while the wave groups of the experiment do not have such a spectral distribution. Therefore, a relationship between both bandwidths is established by recreating the surface elevation of Sinnis' experiment and approximating the wave groups using the Gaussian method from paragraph 5.1. The formulation used by Sinnis for the generation of the wave groups is of the form:

$$\eta(t) = \sum_{n}^{N} a_n \cos(\omega_n (t - t_b)) \tag{C.1}$$

Where a_n is the amplitude of the Fourier component, w_n the wave frequency of the Fourier component, and t_b is the point in time where the wave packet focusses, which is set to 25 seconds. The input parameters used by Sinnis can be found in table C1.

Table C1 The wave group characteristics from Sinnis, where f_c is the central frequency, Δ_{Sinnis} is the bandwidth, and S the linear slope

f_c [Hz]	Δ_{Sinnis}	S
0.85	1.05	0.323
0.90	0.77	0.320
0.90	0.91	0.372
0.90	1.05	0.389
0.90	1.19	0.377

The bandwidth Δ_{Sinnis} is calculated by:

$$\Delta_{Sinnis} \equiv \frac{f_N - f_1}{f_c} \tag{C.2}$$

Where, f_N is the highest frequency, f_1 is the lowest frequency, f_c is the central frequency, and N is the number of Fourier components. From Δ_{Sinnis} and f_c the width of the spectrum is defined. The height of the spectrum is calculated using the formulation for the slope S of the wave group:

$$\mathrm{S} = \sum_{n=1}^{N} a_n k_n \tag{C.3}$$

Where a_n is the amplitude of the Fourier component and k_n the wave number of the Fourier component. a_n is taken constant for every frequency because Sinnis uses a constant amplitude method. Therefore, a_n is calculated for which the S is equal to the values for the slope in table C1. k_n is calculated using the dispersion relation $\omega = \sqrt{gk}$ with the assumption for deep water. Next, the surface elevation of the focused wave group (figure C1a) and the corresponding energy spectrum (figure C1b) are plotted for a single wave group. The energy spectrum has the correct uniform shape. Subsequently, the Gaussian envelope is applied to the focussed wave group (figure C1c) of the surface elevation time series and the bandwidth $\Delta_{Gaus} = 1/(k_0\sigma)$ is calculated, where k_0 denotes the carrier wave number and σ the packet length scale. The values of the bandwidth are plotted and a linear curve

is drawn as a best fit for the data points in figure B1d. Besides, extra focussed wave groups were created with values for the characteristics close to zero and values exceeding the experimental values

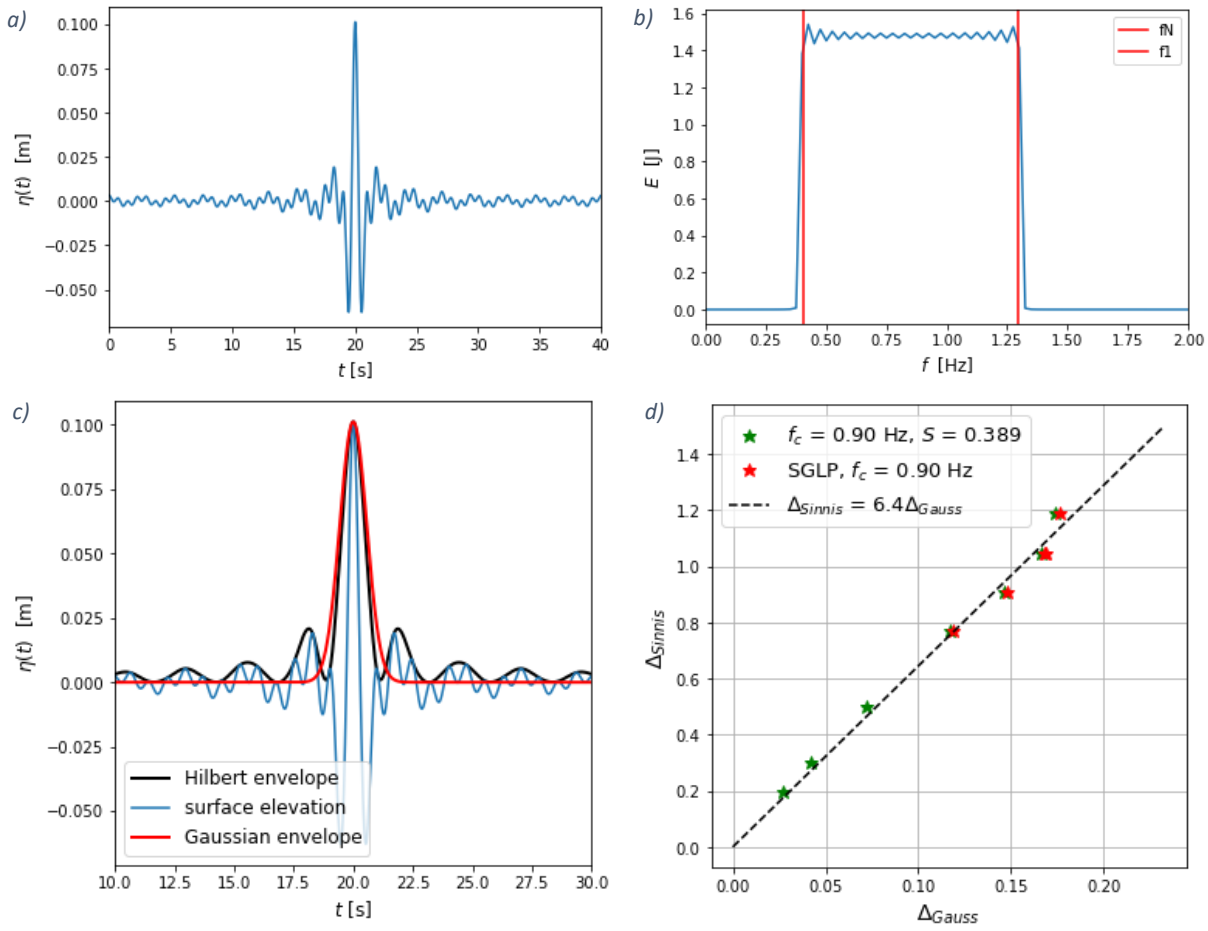

Figure C1 (a) the surface elevation time series of the wave group focusing in t_b = 25 s with f_c = 0.85 Hz, Δ_{Sinnis} =1.05, S = 0.323, and a_n= 0.00316229 m. (b) the corresponding uniformly distributed energy density spectrum. (c) Gaussian envelope applied to the focused wave group. (d) Relationship between the Sinnis bandwidth and the Gaussian bandwidth.

Table C2 calculated Fourier amplitude an and Gaussian bandwidth $\Delta_{Gaussian}$ corresponding to the input Sinnis bandwidth Δ_{Sinnis}

Δ_{Sinnis}	a_n [m]	$\Delta_{Gaussian}$
1.05	0.00316229	0.168
0.77	0.00291500	0.119
0.91	0.00332225	0.148
1.05	0.00339705	0.169
1.19	0.00321090	0.176

from Sinnis, to improve the fit and examine the implications of the relationship on much larger and smaller wave groups. The bandwidth is changed and the slope S is kept constant for these extra generated focussed wave groups. Additionally, to examine any implication to the width of the wave group, the relation between the bandwidths and the length scale of the wave group σ is studied. The relationship between the length scale σ is and both the Sinnis' bandwidth and the Gaussian bandwidth is inverse. The inverse relationship implies that the dependence of the length scale of the wave groups on the bandwidth decreases for smaller values of the bandwidth.

In determining the relationship between the Sinnis and Gaussian linear slope a similar approach is used as for the bandwidth. Wave groups from Sinnis' experiment and extra wave groups with larger and smaller slopes compared to Sinnis' experiment are generated. Both the Gaussian and Sinnis slope are calculated by the summation of the slopes of the individual components $S = \Sigma a_n k_n$. The generated surface elevation time series of the Sinnis experiment and Gaussian wave groups have a total duration D of 32 seconds resulting in a frequency interval $\Delta f = 1/D$ = 0.031 Hz for all the results. The results of the calculation of the linear slope are presented in table C4.

Table C3 The wave group characteristics to generated the extra wave groups and the results for determining the relation between the Sinnis and Gaussian bandwidth and the relation between the bandwidth and the length scale of the wave group.

Δ_{Sinnis}	f_c	S	a_n [m]	σ	$\Delta_{Gaussian}$
0.01	0.90	0.389	0.00372930	225	0.0014
0.2	0.90	0.389	0.00371610	11.21	0.027
0.3	0.90	0.389	0.00369980	7.48	0.041
0.5	0.90	0.389	0.00364838	4.33	0.071
0.77	0.90	0.389	0.00354300	2.58	0.119
0.91	0.90	0.389	0.00347410	2.08	0.147
1.05	0.90	0.389	0.00339705	1.83	0.168
1.19	0.90	0.389	0.00331310	1.75	0.175

Table C4 The wave group characteristics to generated the extra wave groups and the results for determining the relation between the Sinnis and Gaussian linear slope.

Δ_{Sinnis}	f_c	S	a_n [m]	Δ_{Gaus}	$S_{Gaussian}$
1.05	0.85	0.323	0.00258310	0.164	0.324
0.77	0.90	0.320	0.00253620	0.114	0.321
0.77	0.90	0.237	0.00188050	0.114	0.235
0.77	0.90	0.331	0.00262340	0.114	0.332
0.77	0.90	0.182	0.00144050	0.114	0.182
0.77	0.90	0.529	0.00419000	0.143	0.530
0.77	0.90	0.763	0.00605000	0.143	0.763
0.91	0.90	0.249	0.00188050	0.143	0.251
0.91	0.90	0.372	0.00281475	0.143	0.378
0.91	0.90	0.340	0.00257405	0.143	0.342
0.91	0.90	0.137	0.00103405	0.143	0.137
1.05	0.90	0.220	0.00158050	0.164	0.220
1.05	0.90	0.323	0.00232466	0.164	0.326
1.05	0.90	0.358	0.00257405	0.164	0.353
1.05	0.90	0.283	0.00203405	0.164	0.281
1.19	0.90	0.182	0.0012405	0.170	0.179
1.19	0.90	0.377	0.00257405	0.170	0.379
1.19	0.90	0.415	0.00283405	0.170	0.411
1.19	0.90	0.298	0.00203405	0.170	0.298
1.19	0.90	0.614	0.00419000	0.170	0.619
1.19	0.90	0.557	0.00380000	0.170	0.561